EPFL

Ultimate Feature Sizes in Thermally Drawn Fibers: from Fundamental Analysis to Novel Functional Fibers

Présentée le 25 mars 2021

Faculté des sciences et techniques de l'ingénieur
Laboratoire des fibres et matériaux photoniques
Programme doctoral en science et génie des matériaux

pour l'obtention du grade de Docteur ès Sciences

par

Inès RICHARD

Acceptée sur proposition du jury

Prof. R. Logé, président du jury
Prof. F. Sorin, directeur de thèse
Dr L. Weber, rapporteur
Prof. X. Jia, rapporteuse
Prof. V. Michaud, rapporteuse

École
polytechnique
fédérale
de Lausanne

2021

To my family …

Acknowledgements

First, I would like to express my gratitude to my supervisor, Professor Fabien Sorin, who offered me to join his laboratory even before I had decided to do a PhD. I had my first experience in his lab during my master studies and I really appreciated his trust and support during this semester project. I would also like to thank him for the freedom that he gave me to develop this work in many directions. His guidance, encouragement and useful critiques have been essential for the realization of this thesis.

I am very grateful to Prof. Xiaoting Jia, Prof. Véronique Michaud, Dr. Ludger Weber and Prof. Roland Logé for accepting to be in my thesis committee and for taking the time to read my thesis and attend my oral exam. I would like to thank Dr. Ludger Weber, who was also my expert during my candidacy exam, for his valuable and constructive comments on my work during this thesis.

I would like to thank all my colleagues and friends at FIMAP which made my PhD time stimulating, relaxing and fun! First, I want to mention Dr. Tung Dang-Nguyen who was my supervisor during my master project and whose passion for research and also kindness motivated me to join FIMAP for my PhD. I also had the chance to meet my dear Dr. Shahrzad Shadman during this project at FIMAP and I am so thankful for all the interesting discussions and even more importantly all the fun moments we shared at work and during our free time. Chaoqun Dong and Dr. Federica Sordo completed the "girl dream team", who brought much joy and laughter. I was also a great pleasure to share my office with Dr. Alexis Page, Dr. Rajasundar Chandran and Pierre-Luc Piveteau over the years. I am very thankful to all my other colleagues Dr. Yunpeng Qu, Marco Volpi, Dr. Wei Yan, Dr. Tapajyoti Das Gupta, Nicola Bartolomei, Louis Martin-Monier, Dr. Bastien Schyrr, Andreas Leber, William Esposito and Hritwick Banerjee for their help and support they gave me in this project and particularly for all the cheerful moments we shared inside and outside the lab. I would also like to thank the bachelor and master students who worked with me during their semester projects: Alix Dupire, Lison Marthey, Eloïse Masquelier, Victor Meynier and Natsuko Kodani. Finally, I am very thankful to Anne Roy who was always here to solve any kind problems.

I am also very grateful to everyone I had the opportunity to work with outside from our lab. I would like to thank Prof. Véronique Michaud for the use of LPAC equipment and Dr. Adrien Demongeot, Dr. Amaël Cohades and Raphaël Charvet for their help and advises. I wish also to thank the members of CIME for their teaching and technical support: Dr. Thomas La Grange, Dr. Marco Cantoni, Fabienne Bobard, Danièle Laub and Colette Vallotton. The ATMX and BM workshops were also very helpful for the preform preparation. I also thank the professors and colleagues in other laboratories and research institutes which gave me very important advises and performed experiments for me: Prof. Stéphanie Lacour and Dr. Giuseppe Schiavone (LSBI), Prof. Grégoire Courtine and Dr. Nicholas D. James (UPCOURTINE), Prof. Vasiliki Tileli (INE), Prof. Sandro Carrara and Simone Aiassa (LSI), Prof. Jörg F. Löffler and Dr. Güven Kurtuldu (LMPT, ETH), and Prof. Antonia Neels and Anjani Maurya (X-Ray, EMPA).

I would also like to thank all my friends inside and outside EPFL who always support me and bring so much joy in my life. I can mention only a few here: my long-time friends Zyanya, Christine, Lucie and Anais; my fellow EPFL engineers Céline, Marie-Claude, Chloé, Zoé, Marie, Delphine, Anouk and Anahita; the Qwertz team Manon, Yolan and Tobias; my

Abstract

The fiber thermal drawing process has emerged as a simple and scalable technique for the fabrication of multifunctional and flexible electronics. The integration of materials with various physical and functional properties in well-defined architectures opened a wide range of applications. However, the trend of increasing number of functionalities, which requires a reduction in size of each fiber constituent, revealed the importance of instability mechanisms that need to be better understood and overcome. In this thesis, we address several challenges associated with the process-microstructure relationship that govern the achievable feature sizes. We first tackle the problem of thermal reflow of polymeric textures induced by the Laplace pressure. We develop a reflow model that can be applied to periodic textures during isothermal annealing and extend it to the thermal drawing process. After validating our model with experimental data, we show that the reflow driving force can be significantly reduced by codrawing two materials of low interfacial tension. We demonstrate this finding by drawing sub-100 nm textures on polycarbonate fibers. The second part focuses on the influence of the drawing parameters on the degree of polymer chain alignment which induces serious shrinkage upon heating. We reveal that the drawing stress, which depends on the drawing speed and temperature, controls the shrinkage stress. Furthermore, we show that the degree of chain orientation increases linearly with the stress at low thermal drawing stress, and then saturates, which correlates well with the amount of shrinkage observed. We then highlight the use of this process-dependent alignment to tune the mechanical properties of the fibers and the bending behavior of multi-material fibers. Finally, a heat treatment is proposed for reducing the chain alignment to increase the dimensional stability of fiber devices such as temperature sensors.

In the third part, we switch our attention to inorganic materials and discuss the long-lasting challenge of the thermal drawing of bulk metallic glasses (BMGs) which enables us to circumvent the size limitation of crystalline metal electrodes due to capillary instabilities. We first demonstrate the production of well-ordered $Pt_{57.5}Cu_{14.7}Ni_{5.3}P_{22.5}$ (Pt-MG) ribbons within a polyetherimide matrix with uniform features down to 40 nm. We reveal via transmission electron microscopy analyses a crystallization-induced break up. Furthermore, our approach enables us to study the influence of the process on the crystallization kinetics of the Pt-MG ribbons. We show that the latter is enhanced by the increase in deformation and decrease in size both at the micro- and nanoscale. We then demonstrate the ability of thermal drawing of another BMG, $Au_{49}Ag_{5.5}Pd_{2.3}Cu_{26.9}Si_{16.3}$, by selecting a poly(methylmetacrylate) cladding with matching thermo-mechanical and rheological properties. The ultimate feature size, caused by the onset of crystallization, is a few hundred nanometers. Finally, we show two examples of devices highlighting the novel functionalities enabled by the thermal drawing of BMGs. We produce and test *in vivo*, in collaboration with colleagues in the bio-engineering department, neural probes allowing electrical stimulation, recording and precise drug delivery, and electrochemical sensors integrating the three-electrode system in a single fiber.

Keywords: Thermal drawing, Multi-material fibers, Micro- and nano-fabrication, Surface engineering, Polymer engineering, Bulk metallic glasses, Crystallization kinetics, Neural probes, Electrochemical sensors.

Résumé

Le procédé de tirage à chaud de fibres a émergé comme une technique de fabrication simple et à grande productivité pour des composants électroniques flexibles et multifonctionnels. L'intégration de matériaux avec différentes propriétés physiques et fonctionnelles dans des architectures bien définies a ouvert la porte à un large éventail d'applications. Cependant, la tendance à l'augmentation du nombre de fonctionnalités, qui nécessite une diminution en taille des composants, a révélé l'importance de plusieurs mécanismes d'instabilité qui doivent être mieux compris et maitrisés. Dans cette thèse, nous abordons premièrement le reflow de textures polymériques causé par la pression de Laplace. Nous développons un modèle pouvant être appliqué à des textures périodiques pendant un recuit isotherme et l'étendons au procédé de tirage. Après validation du modèle avec des données expérimentales, nous montrons que le reflow peut être ralenti en diminuant la tension d'interface. Cette stratégie nous permet de créer des fibres avec des textures inférieures à 100 nm. La deuxième partie cible l'influence des paramètres de tirage sur le degré d'alignement des chaines de polymères qui induit un retrait important sous l'effet de la chaleur. Nous révélons que la contrainte de tirage, qui dépend de la vitesse et de la température, contrôle la contrainte interne. De plus, nous montrons que le degré d'orientation augmente d'abord linéairement avec la contrainte de tirage avant de saturer, ce qui correspond bien au retrait observé. Nous mettons ensuite en évidence l'utilité de cet alignement pour contrôler les propriétés mécaniques des fibres et le comportement en flexion de fibres multi-matériaux. Enfin, un traitement thermique est proposé pour réduire l'alignement afin d'augmenter la stabilité dimensionnelle.

Dans la troisième partie, nous nous intéressons aux matériaux inorganiques et discutons du défi de longue date du tirage des verres métalliques qui nous permet de contourner la limitation de taille des électrodes métalliques cristallines due aux instabilités capillaires. Nous démontrons d'abord la production de rubans bien ordonnés de $Pt_{57.5}Cu_{14.7}Ni_{5.3}P_{22.5}$ (Pt-MG) dans une matrice de polyétherimide avec des dimensions uniformes jusqu'à 40 nm. Nous révélons via des analyses de microscopie électronique une fracture induite par la cristallisation. De plus, notre approche nous permet d'étudier l'influence du procédé sur la cinétique de cristallisation du Pt-MG. Nous montrons que cette dernière est accélérée par l'augmentation de la déformation et la réduction de la taille des rubans, à la fois à l'échelle micro et nanoscopique. Nous démontrons ensuite le tirage d'un autre verre, $Au_{49}Ag_{5.5}Pd_{2.3}Cu_{26.9}Si_{16.3}$, en sélectionnant une gaine de polymère avec des propriétés thermomécaniques et rhéologiques compatibles. L'épaisseur la plus fine atteignable est de quelques centaines de nanomètres, dû au début de cristallisation. Enfin, nous montrons deux exemples de fibres mettant en évidence les nouvelles fonctionnalités permises par ces verres. Nous produisons et testons *in vivo*, en collaboration avec des collègues du département de bio-ingénierie, des sondes neuronales permettant la stimulation et l'enregistrement électrique, et l'administration de médicaments, ainsi que des capteurs électrochimiques intégrant le système à trois électrodes dans une seule fibre.

Mots-clés: Tirage à chaud, Fibres multimatériaux, Micro- et nano fabrication, Ingénierie de surfaces, Science et ingénierie de polymères, Verres métalliques, Cinétique de cristallisation, Sondes neuronales, Capteurs électrochimiques

Contents

List of Abbreviations

APAP	Paracetamol
Au-MG	$Au_{49}Ag_{5.5}Pd_{2.3}Cu_{26.9}Si_{16.3}$
BMG	Bulk Metallic Glass
BSE	Backscattered-Electron
CE	Counter Electrode
cPE	Conductive Polyethylene
cPC	Conductive Polycarbonate
CTE	Coefficient of Thermal Expansion
CV	Cyclic Voltammetry
ddr	Draw Down Ratio
DMA	Dynamic Mechanical Analysis
DSC	Differential Scanning Calorimetry
EDX	Energy Dispersive X-Ray
EMG	Electromyographic
FWHM	Full Width Half Maximum
GABA	Gamma-Aminobutyric Acid
GFA	Glass Forming Ability
GFAP	Glial Fibrillary Acidic Protein
HRTEM	High Resolution TEM
LOD	Limit of Detection
MG	Metallic Glass
MLF	Mesencephalic Locomotor Region
MRO	Medium-Range Order
MW	Molecular Weight
NMP	N-Methyl-2-Pyrrolidone
OCP	Open Circuit Potential
OM	Optical Microscopy
PBS	Phosphate-Buffered Saline
PC	Polycarbonate
PDMS	Polydimethylsiloxane
PE	Polyethylene
PEI	Polyetherimide
PMMA	Poly(methyl metacrylate)
PPn	Pedunculopontine Nucleus
PSU	Polyethersulphone
Pt-MG	$Pt_{57.5}Cu_{14.7}Ni_{5.3}P_{22.5}$
RE	Reference Electrode
SAED	Selected-Area Electron Diffraction
SAXS	Small Angle X-Ray Scattering
SCLR	Supercooled Liquid Region
SEM	Scanning Electron Microscopy

SRO	Short-Range Order
STZ	Shear Transformation Zone
TEM	Transmission Electron Microscopy
T_g	Glass Transition Temperature
TTT	Time Temperature Transformation
t_x	Crystallization Time
T_x	Crystallization Temperature
VT	Voltage Transient
WAXS	Wide Angle X-ray Scattering
WE	Working Electrode
XRD	X-ray Diffraction

1 Introduction

The development of the fiber thermal drawing technique has enabled the mass-production of low-loss optical fibers which revolutionized the field of telecommunication [1]. The major feature of this technique is its efficiency and its ability to produce kilometer-long fibers with a precise control of the cross-section, starting from a macroscopic scaled—up version of the fiber. Since the 2000s, a new field of research has emerged based on this process: the multi-material thermal drawing [2]–[4]. Instead of limiting themselves to one single type of material and a simple architecture, research groups started to work on the fabrication of fibers containing several materials arranged in complex structures. Since then, thermoplastics, composites, elastomers, low melting point metals and chalcogenide glasses have been successfully integrated inside thermally drawn polymer fibers. A large variety of fiber-devices with advanced functionalities were developed finding applications in optics, sensing, electronics, energy and neuroscience, beside others [5]–[12].

The thermal drawing technique is foreseen as a promising alternative to rigid and planar electronics, due to the growing interest in flexible and soft electronics, as well as in smart textiles. However, the current trend towards device miniaturization and integration pose some significant challenges to the thermal drawing technique. Ineluctably, by pushing the limits in terms of structure, dimensions and materials, additional phenomena start to play a role in the preservation of the cross-section during fiber drawing. A deeper understanding is therefore required to develop strategies to reduce their effects, which is the core of this thesis.

1.1 Thermal drawing of multi-material fibers

1.1.1 Thermal drawing technique

The thermal drawing process consists in slowly inserting a macroscopic preform in a furnace, heating it above the glass transition temperature (T_g) of the polymer cladding and pulling it at fixed speed to produce a kilometer-long and uniform fiber, as schematized in Figure 1-1 (left). The three temperatures in the oven enable us to define a suitable temperature profile so that all the materials in the preform reach a processable viscosity in the neckdown region. They also determine the stress applied to the fiber during the draw. The feeding speed and the drawing speed define the final fiber dimension. Following the law of mass conservation, the variation of the cross-sectional dimensions can be estimated by the ratio of the speeds, called the "draw-down" ratio (ddr):

$$ddr = \sqrt{\frac{v_{draw}}{v_{feed}}} = \frac{R_{preform}}{R_{fiber}} \tag{1.1}$$

With $R_{preform}$ and R_{fiber} being the radius of the preform and the fiber, respectively, assuming a circular fiber. It is often assumed that the fiber keeps the exact same cross-section as the initial preform and therefore this ratio can also be applied to estimate the dimensions of the different elements inserted inside the preform. We will however see below that depending on the materials and on the drawing conditions, other mechanisms can influence the geometry during the draw and have an impact on the cross-section conservation.
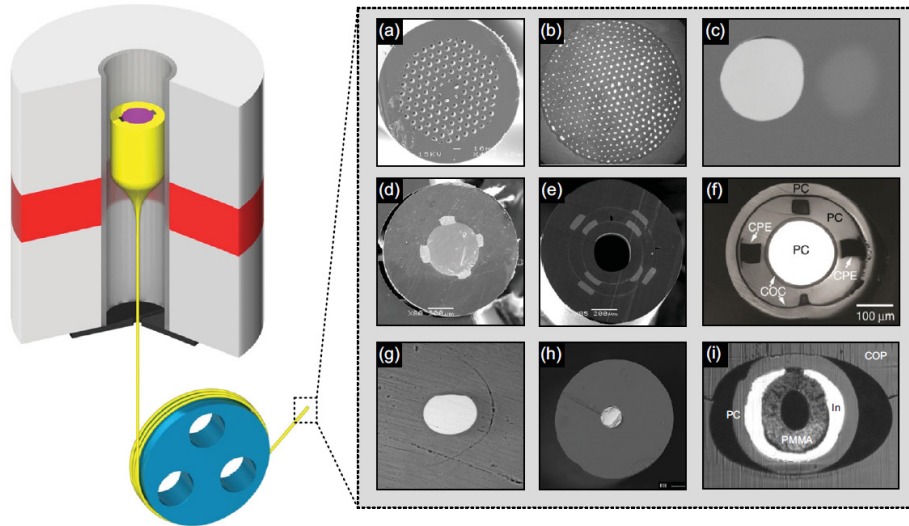
Figure 1-1 Schematic of the drawing process and example of multi-material fiber cross-sections [13].

Several methods can be used to fabricate the macro-scale preforms such as stack-and-draw, thin film rolling, hole drilling or direct 3D printing. By combining these approaches, complex preforms including various materials and precise architectures have been obtained (see Figure 1-1 (right)). Furthermore, a single draw is sometimes not sufficient to reach feature size with micrometer or nanometer dimensions. Therefore, an iterative technique has been developed where one or several first drawn fibers are inserted in a new preform and drawn for a second time. This process can theoretically be repeated until the desired dimensions are obtained providing the materials and structures support several drawing. We will discuss some challenges in the next part.

1.1.2 Compatible materials

Since the advent of the multi-material fiber field, the family of drawable materials has considerably expanded. Furthermore, a deeper understanding of the requirements on the materials to be drawn, or co-drawn, allowed the identification of new class of thermally drawn materials such as elastomers [8]. Guidelines concerning the required thermo-mechanical and rheological properties have been developed [3], [4]. First, the cladding material must be able to support the stress of the draw and have a viscosity in the range of 10^3 to $10^7\ Pa\ s$ during drawing. The high viscosity state contributes to the preservation of the structure from the preform to the fiber level. Secondly, all the processed materials should flow at a common temperature and therefore have compatible viscosities. The materials should also remain amorphous during the draw to enable deformation. If crystalline materials are drawn, such as metals, they have to be processed above their melting point so that they can flow in the fiber cladding. The preform should therefore be carefully designed to prevent any leakage or

mixing of molten materials during the draw in order to maintain the desired fiber architecture. Finally, the coefficient of thermal expansion of the various materials should be in a similar range to prevent residual stresses in the fiber due to the cooling.

At the start of this thesis, the materials used to make solid electrodes in the fibers were either crystalline metals or composites filled with conductive particles such as carbon black or carbon nanotubes. However, we can note upfront some limitations, which are: (i) crystalline metals have to be fully encapsulated and can suffer from capillary instability since they are drawn in their molten state and (ii) the composites often have a high resistivity and thus the electrical resistance of thin features can become extremely high, due to the limited amount of incorporated conductive particles for viscosity preservation.

1.1.3   Thermal drawing modelling

As we will see later in this thesis, several mechanisms occurring during a draw depend on the processing temperature, viscosity and velocity profiles, beside others. Therefore, it is necessary to have a model to simulate the deformation of the preform inside the drawing tower. The temperature profile is usually approximated with a quadratic function:

$$T(z) = T_{max} - \frac{\left(T_{max} - T_g\right)}{(L/2)^2} z^2 \tag{1.2}$$

With T_{max} the maximum temperature measured, T_g the glass transition temperature and L a fitting parameters corresponding to the length of the "hot zone". If the temperature dependent viscosity of the material is known, the viscosity profile can then be determined by $\eta(z) = \eta(T(z))$.

Pone et al. [14] and more recently Tung et al. [15] derived an expression describing the deformation of the preform-to-fiber neck down region for a cylindrical fiber $R(z)$ with $z \in (0, L)$ which fits well with the experimental observations. The main assumptions of their models are : i) the polymer melt is an incompressible Newtonian fluid, ii) we are in a low Reynold-number, high Capillary-number regime and iii) the surface tension and gravitational contributions are negligible compared to the stress induced by the pulling. Furthermore, the temperature is assumed uniform radially.

Based on these hypotheses, a relation between the velocity (v_z) and the viscosity profile ($\eta(z)$) along the drawing direction (z) can be deduced.

$$\frac{\eta(z)\frac{\partial v_z}{\partial z}}{v_z} = constant \tag{1.3}$$

The velocity profile can then be obtained by integration Equation 1.3 with the boundary conditions defined by the feeding speed $v_z(0) = v_f$, and the drawing speed $v_z(L) = v_d$:

$$v_z(z) = \exp\left(\ln v_f + \frac{\int_0^z \frac{dz}{\eta(z)}}{\int_0^L \frac{dz}{\eta(z)}} \ln \frac{v_d}{v_f}\right)$$ (1.4)

Equation 1.4 enables us to describe the flow of material during the thermal drawing and also to estimate the time spent at each position and therefore temperature.

1.2 Mechanisms influencing the cross-section preservation

1.2.1 Surface reflow

Thermal reflow is one of the processes responsible for the alteration of the fiber cross-section below a certain feature size. If a texture is imprinted on the surface of a preform, reflow can occur during thermal drawing and flatten the surface due to the high temperature and corresponding low viscosity. The driving force for this reflow is the Laplace pressure which depends on the curvature of the surface and the surface tension of the interface. A model describing the flowing mechanism during thermal drawing and allowing us to predict if a texture would be preserved on the fiber level was developed previously in our group by T. Nguyen-Dang [16]. This deeper understanding allowed us to identify strategies to alleviate this limitation. Reflow can be reduced either by increasing the viscosity of the polymers during drawing or by lowering the surface tension.

The use of polyetherimide, a high strength polymer that can be drawn under high viscosity, allowed the fabrication of surface textures down to 20 μm [10], [17]. Furthermore, surface textures with periods down to 600 nm were obtained by cooling the patterned surface with a nitrogen flow to increase the viscosity locally [18]. Another strategy consists in interfacing two materials during the draw and mechanical peeling or selectively etching one of them after drawing. Khudiyev et al. demonstrated sub-10 μm patterns on semicrystalline polymer fibers by co-drawing polyvinyl difluoride that flows in a low viscosity state, with polycarbonate which retains a high viscosity during the draw and maintains the pattern [18]. Moreover, sub-micrometer textures were obtained on poly(methyl metacrylate) PMMA and polycarbonate (PC) fibers by Nguyen-Dang et al. using a conductive polyethylene (cPE) sacrificial layer which drastically reduces the interfacial tension and thus the thermal reflow as shown in Figure 1-2 [16].
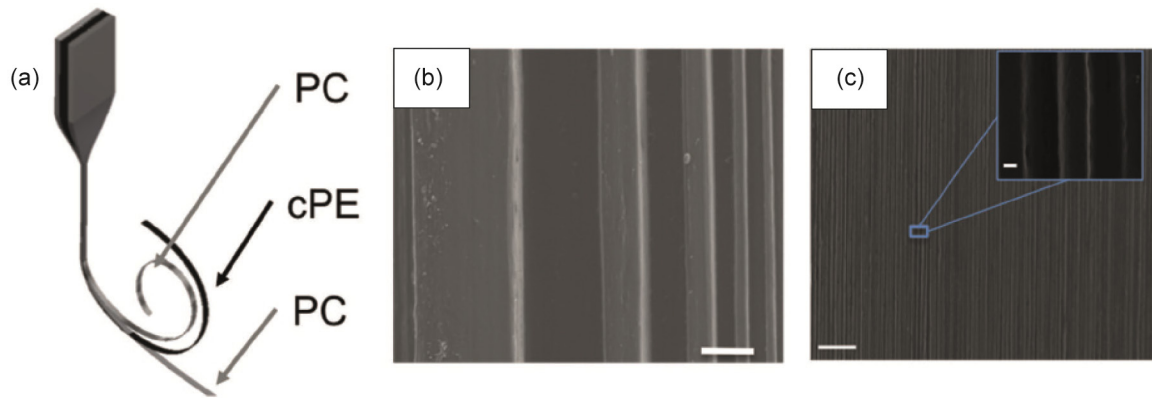
Figure 1-2 Textured thermoplastic fibers. (a) Schematic of the preform-to-fiber process. (b) Scanning electron microscopy (SEM) micrograph of a textured ribbon with square texture of different height and width (scale bar: 10 μm). (c) SEM micrograph of a sub-micrometer square shape texture (scale bar: 10 μm) with a zoom-in (scale bar: 200 nm) [16].

1.2.2   Capillary instabilities

When reaching the nanoscale and depending on the materials, axial and azimuthal capillary instabilities can develop and induce breakup of fine features. These instabilities were studied by Plateau in 1873 who attributed them to the surface tension [19]. The break-up of films into droplets is energetically favorable since it reduces the surface area and therefore the surface energy. Later, Rayleigh studied the growth rate of these perturbations and determined that they increase exponentially with time [20]. The influence of a surrounding fluid was then described by Tomotika who demonstrated the influence of the viscosity ratio between the core and the shell fluids on the instability growth rate [21]. Models in the thermal drawing field have been based on Tomotika linear instability theory in order to understand the material and geometrical properties controlling the breakup of wires and cylindrical shells [22]–[24]. D.S. Deng et al. created some stability and material selection maps which can serve as a guideline to select potentially suitable materials in function of the final feature dimensions (Figure 1-3). The main parameters controlling the instabilities are the viscosity of the core or shell and cladding materials, the surface tension and the final feature size.
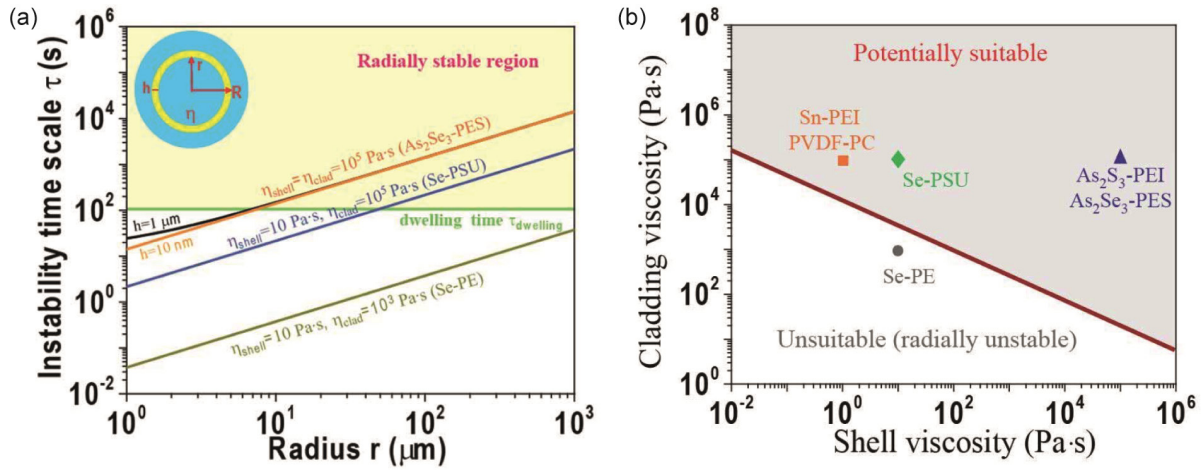
Figure 1-3 (a) Radial stability map. (b) Material selection map for various pairs of materials (from [25]).

The ultimate size limit depends mainly on the materials and especially their surface tension and viscosity during processing. Therefore, continuous nanowires with diameters below 15 nm of chalcogenide glasses such as Ga-As-Se-Te, As_2Se_3 and Se could be drawn in polymer matrices [26], [27]. On the other hand, crystalline metal wires have been limited to 1 μm diameter due to their high surface energy and the necessity to draw them in their molten state, i.e. at very low viscosity. Further size reduction induces diameter instabilities which finally results in the break-up of the rods as shown in Figure 1-4 for indium wires drawn in a PMMA cladding.
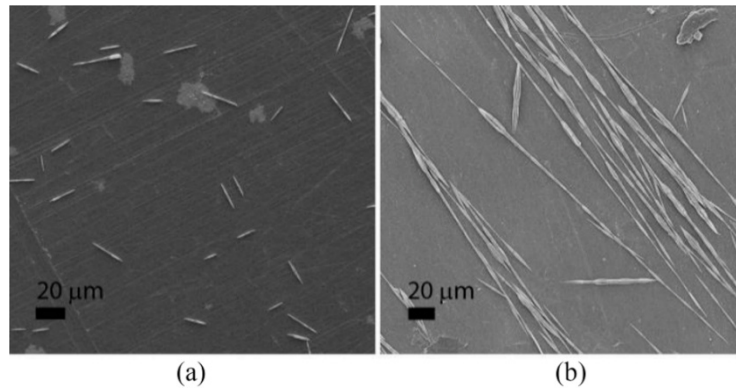
Figure 1-4 SEM images of indium wires drawn to diameters of (a) 190 nm and (b) 930 nm in a PMMA cladding [23].

Fibers containing a dense array of metallic wires or fine structures are of interest to serve as neuroprobes or as electromagnetic metamaterial beside others. Metamaterial fibers made of metallic wire arrays and split ring resonators were drawn and exhibited promising performance [28]. However, due to the micron feature sizes, their application is limited to operating frequencies in the THz to the mid-IR range. Reaching smaller sizes would enable the use of thermal drawing to fabricate large volume of metamaterial-based devices working in the NIR and visible.

Finally, studies highlighted the limitation in tuning the drawing parameters such as the drawing speed and temperature to lower the cladding viscosity, and revealed the necessity to change the materials [23]. By drawing metallic wires in a glass cladding, the interfacial surface tension was minimized and wire diameters down to 50 nm were achieved [29]. Another strategy would be to change the metallic material from traditional crystalline ones, which need to be processed in their molten state, to amorphous metals which can be drawn in a high viscosity state. Chapter 4 of the thesis is dedicated to introduction of this class of materials in the thermal drawing process.

1.2.3 Polymer chain orientation

In addition to the structural changes described above, thermal drawing can also have a large impact on the internal morphology of the polymers. In particular, fiber processing techniques such as extrusion [30], [31], spinning [32]–[34] and drawing [35]–[37] were reported to induce polymer chain alignment due to the significant amount of flow and relatively fast cooling.

On the one hand, a high degree of chain orientation can be favorable since it induces higher yield strength, strain hardening, Young's modulus and thermal conductivities [38]–[40]. The influence of the fiber drawing parameters on the mechanical properties of PMMA fibers was studied by Jiang et al. [35]. They revealed that the mechanical strength increases with the drawing force but decreases with an increase in drawing temperature. Furthermore, a subsequent annealing lowers the strength but enhances the ductility. On the other hand, such alignment leads to a rise in entropic energy due to the out-of-equilibrium conformation. Consequently, high temperatures or the presence of solvent can enable the relaxation of the chains into a random coil conformation and result in significant macroscopic shrinkage [33]. Thermally stimulated shrinkage was reported to depend on the polymer type and morphological state determined by processing [41].

This shrinkage should be prevented when a high dimensional stability is required during the fiber-based device application, or for some post-processing. In particular, thermal shrinkage imposes a limitation on the number of fibers that can be iterative drawn in a new preform. Indeed, if the cladding of the new preform is not able to prevent the contraction of the first step fibers at the drawing temperature, the latter can induce complete failure of the preform [42]. Stajanca et al. proposed annealing strategies to increase the climatic stability of a thermally drawn PMMA optical fiber sensor [37]. They further revealed that the annealing time and temperature have to be tailored as a function of the drawing parameters in order to be efficient. Another strategy developed by Shadman et al. relied on the design of a core-shell fiber with a semicrystalline polymer in the core which could prevent shrinkage [43].

Even though the influence of the drawing parameters on the fiber properties has been reported, no quantitative correlation has been made between the processing parameters and the degree of orientation. An in-depth understanding would enable the fine tuning of the fiber properties to fulfill specific requirements in terms of strength or high temperature stability for example.

1.3 Bulk metallic glasses

As mentioned earlier, traditional electrode materials present some intrinsic limitations in terms of conductivity or geometry. Therefore, a part of this thesis consisted in identifying new materials that could open doors to novel opportunities for fiber based devices and electronics. Metallic glasses which are alloys that retain an amorphous structure after cooling from their liquid state are ideal candidates. Indeed, these alloys exhibit a glass transition temperature like thermoplastic polymers and can reach viscosities in the range of 10^6 to $10^8 \; Pa \; s$ above which is the so-called supercooled liquid region (SCLR) [44]–[46]. Furthermore, some recently developed compositions, referred as bulk metallic glasses (BMG), show very large resistance against crystallization when heated above their T_g. In addition to their attractive processing properties, BMGs exhibit remarkable properties such as high strength, high elasticity and good resistance to corrosion. The combination of all these properties opens a wide range of applications for BMGs in fields such as catalysis, nano and micro electromechanical systems and biomedical implants [47].

BMGs can be produced by rapid cooling from the molten state by casting or melt-spinning for example. Then, their low viscosity and high crystallization resistance in the SCLR allow the production of micro and nano-sized parts by shaping them in this temperature region as shown in Figure 1-5 [45], [48]. Nanorods were fabricated by thermoplastic forming based on embossing BMGs in porous alumina mold [49]. Hasan et al. also developed a thermoplastic drawing method using embossed templates and were able to produce cone-shaped structures or constant diameter nanowires by varying the pulling speed and temperature [50]. Furthermore, Yi et al. processed BMG fibers by pulling rods in the SCLR and reached diameters down to 70 nm for the best BMG [51].
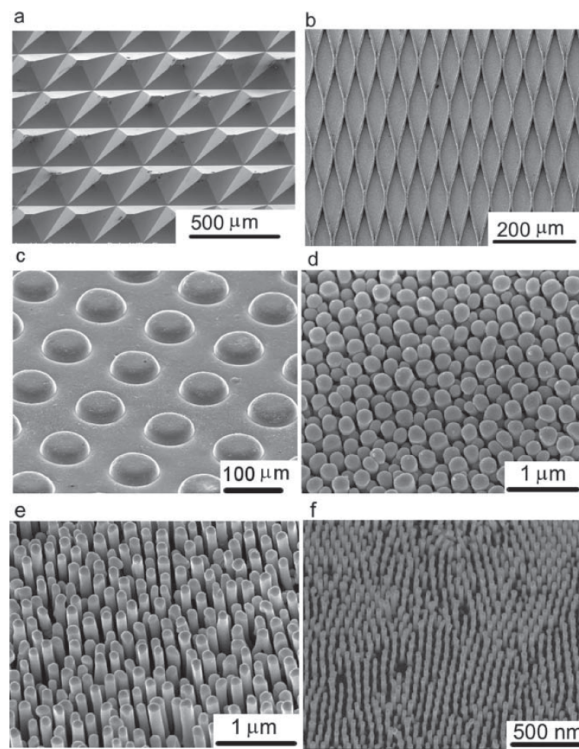
Figure 1-5 $Pt_{57.5}Cu_{14.7}Ni_{5.3}P_{22.5}$ molded surface patterns [48].

Therefore, it seems that some BMGs could fulfill all the requirements for thermal drawing and enable the fabrication of sub-micrometer features of high conductivity. Indeed, the intrinsic conductivity of BMGs is lower compared to crystalline metals but still high compared to filled polymer composites. Nevertheless, despite almost two decades of research in multi-material fibers, no BMG composition co-drawable within a polymeric matrix had been reported at the start of this thesis. In the following part, we first discuss the influence of the compositions on the BMG properties such as viscosity or crystallization resistance. Then, we present a review of the influence of various external parameters, including non-isothermal annealing, deformation and size on the deformation behavior and crystallization kinetics.

1.3.1 BMG properties

Glass-forming ability

The glass-forming ability (GFA) describes the ability of a metallic alloy to transform into a glassy state. A high packing density in multicomponent alloys and a large number of elements, referred to as the "confusion principle", are proposed to be some important parameters to improve the GFA [52]. Inoue [53] stated three empirical criteria necessary for the formation of BMGs:

1. The system should consist of three or more elements
2. There should be a difference greater than 12% in atomic sizes of the main elements
3. There should be a negative heat of mixing amongst the main elements

The GFA can be quantified either by the maximum casting diameter of a fully amorphous BMG or by the critical cooling rate necessary to prevent any crystallization. Several criteria based on thermodynamic quantities have been considered to predict the GFA of new compositions, however none of them showed precise correlation [54]–[56]. These difficulties might arise due to the different stabilization mechanisms that have been reported for various BMG compositions. Gross et al. proposed to divide good glass formers into two main classes: (i) kinetically stabilized BMGs which are characterized by a high viscosity that prevents atomic motion (Zr-based or Fe-based), (ii) thermodynamically stabilized BMGs that have either a low driving force for crystallization (Pd-based) or high interfacial energy between the amorphous and crystalline phase (Pt-based) [57].

Temperature-dependent crystallization kinetics

The crystallization kinetics of BMGs is highly temperature dependent. Plots of the onset times of the crystallization as a function of the temperature, referred to as time-temperature-transformation (TTT) diagrams, are used to represent the kinetics. These diagrams show a nose shape due to the different mechanism controlling the crystallization in function of the temperature. Above the nose, the undercooling is low and the driving force for crystallization is limited. Therefore, the crystallization is controlled by the nucleation rate. Due to the stochastic nature of nucleation and its dependence on the presence of heterogeneous nucleation sites, large scatter in onset times is observed in this range [58]. On the other hand, below the nose, it is limited by crystal growth since the high viscosity of the melt limits the mobility of atoms and almost no scatter in the time is observed.

Classical nucleation and growth theory can be used to model the crystallization kinetics [59]. The steady-state nucleation rate (I_v) is defined as,

$$I_v(T) = \frac{A_v}{\eta(T)} exp\left(-\frac{16\pi\sigma^3}{3k_BT\Delta G(T)^2}\right)$$ (1.5)

where A_v is a fitting parameter, $\eta(T)$ the temperature dependent viscosity, σ and $\Delta G(T)$ respectively are the interfacial energy per area and the Gibbs free energy difference per volume between the liquid and the crystalline phases, and k_B is the Boltzmann constant. Furthermore, the growth of the nuclei (u) can be estimated by using a diffusion-controlled growth rate, which corresponds to the product of a kinetic and thermodynamic term,

$$u(T) = \frac{k_BT}{3\pi l^2\eta(T)}\left[1 - exp\left(-\frac{n\Delta G(T)}{k_BT}\right)\right]$$ (1.6)

where l is the average atomic diameter and n is the atomic volume. The temperature dependent viscosity can be fitted by the Vogel-Fulcher-Tammann relationship and $\Delta G(T)$ estimated by $\Delta G(T) = \Delta S_F(T_{liq} - T)$, with ΔS_F the entropy of fusion per volume and T_{liq} the liquidus temperature. Figure 1-6(a) shows the dependence of both rates with temperature for a Pd-based BMG. At low temperature in the supercooled liquid region, the crystal nucleation rate is high due to the large undercooling but the crystal growth is slow due to the high

viscosity. At high temperature, the opposite trend is observed, and crystal growth is favored. Finally, the time (t_x) to crystallize a certain volume fraction (x) during isothermal holding can be estimated by:

$$t_x = \left(\frac{3x}{\pi I_v(T)[u(T)]^3}\right)^{\frac{1}{4}}$$

(1.7)

A good fit of the TTT diagram of BMG can be obtained as illustrated in Figure 1-6(b) for a Pd-based BMG. This model outlines the contribution of the viscosity, interfacial energy and Gibbs free energy to the crystallization kinetics. Several assumptions have been made to develop this model and in practice several factors can also influence the kinetics as we will discuss below.
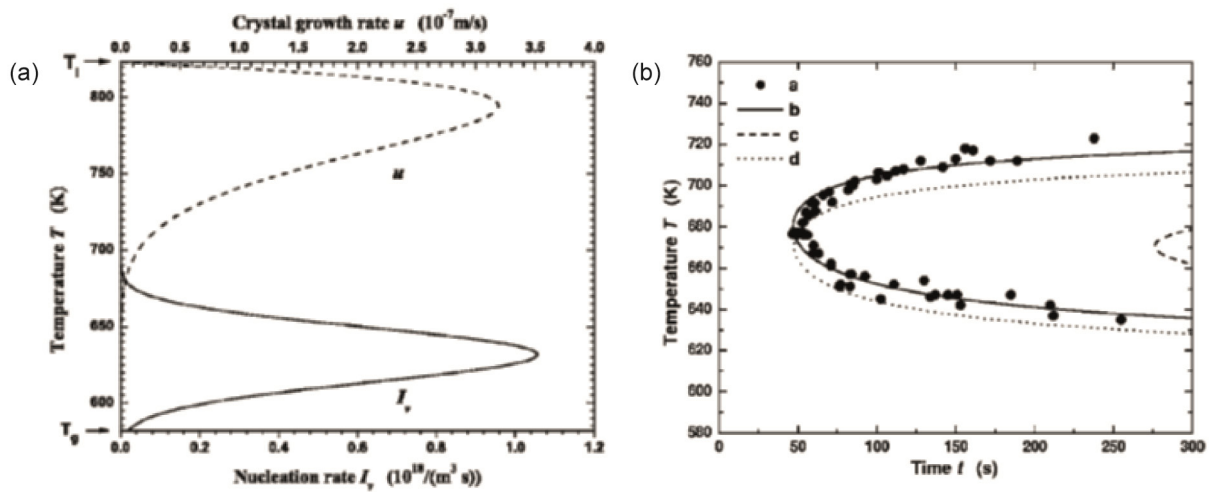
Figure 1-6 (a) Nucleation rate and crystal growth rate in function of temperature for a Pd-based BMG and (b) **a** Experimental data and **b, c, d** calculated isothermal TTT diagram with various A_v [60].

Viscosity

In the supercooled liquid state, the temperature dependent viscosity of BMGs can be described by an empirical Vogel-Fulcher-Tammann (VFT) relationship:

$$\eta = \eta_0 exp\left(\frac{DT_0}{T-T_0}\right)$$

(1.8)

where η_0 is the infinite temperature limit of viscosity, T_0 a constant and D is the kinetic fragility index [61]. Small D values correspond to fragile glass formers whose viscosity descreases more strongly with increasing temperature, while large D values describe strong ones. Figure 1-7 shows a fragility plot of several BMGs with D values between 10 and 26. As one can see, to reach the same viscosity level, e.g. a processable viscosity, BMGs have to be more or less heated above their T$_g$. A lower viscosity would permit easier processing, however it often corresponds to faster crystallization kinetics. Therefore, strong MGs have generally better glass forming ability due to the decrease in growth kinetics [62]. Another factor representing the fragility is the steepness index m:

$$m = \frac{\partial log\big(\eta(T)\big)}{\partial \big(T_g/T\big)}\bigg|_{T=T_g} \qquad (1.9)$$

With large m corresponding to fragile behavior.
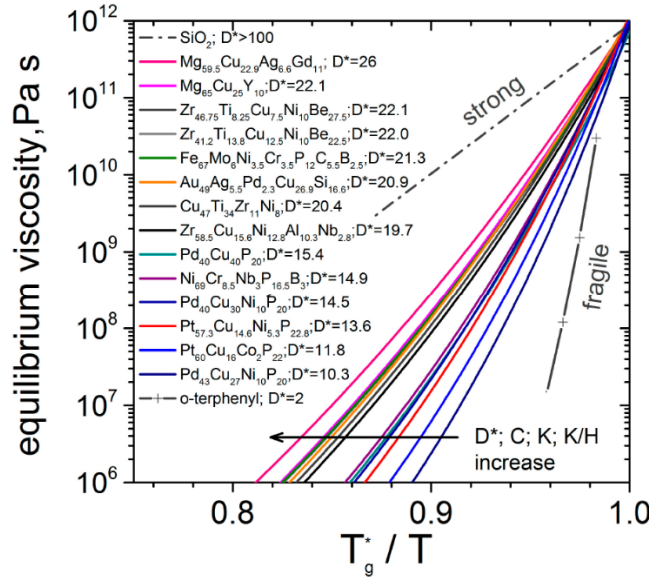
Figure 1-7 Fragility (Angell) plot of various BMGs [63].

Atomic structure

The atomic structure of metallic glasses was initially assumed to be completely random due to the absence of sharp diffraction peaks in X-ray and electron diffraction. However, more recently, the presence of short-range order (SRO) and medium-range order (MRO) was proposed [64]–[66]. The SRO corresponds to an arrangement of the nearest-neighbor atoms or solute-centered clusters. These clusters can serve as building blocks for the formation of 3D cubic or icosahedral densely packed spaces referred as MRO as shown in Figure 1-8. The clusters are not perfect and contain chemical and topological disorder, therefore the order only extends over a few clusters. Furthermore, these packings do not induce any orientational order of the clusters. Hirata et al. reported a direct observation of this local ordering through nanobeam electron diffraction for a Zr-Ni MG and correlated it with molecular simulation [67]. It remains however very challenging to observe experimentally such local atomic ordered configurations in overall disordered BMG.
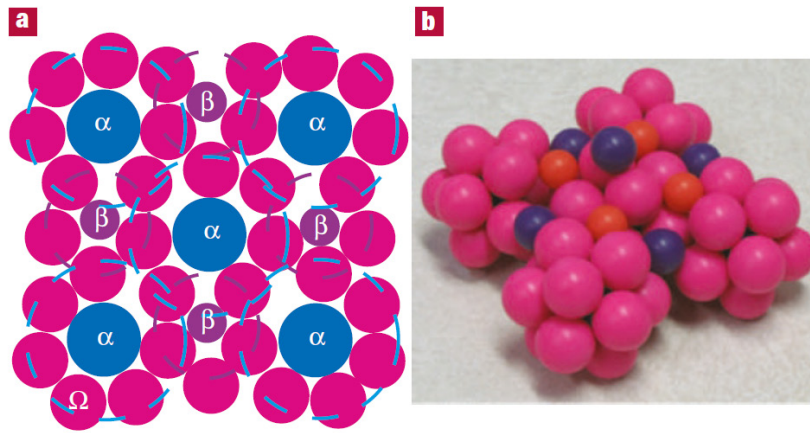
Figure 1-8 Illustrations of a cluster-based packing structure (a) in 2D and (b) in 3D where α, β and Ω correspond to three different atomic species [66].

Deformation mechanism

At room temperature, metallic glasses are characterized by a very high mechanical strength and hardness, but very limited ductility. Due to the absence of ordering, no dislocation can form and facilitate plastic deformation like in crystalline metals. In BMGs, Spaepen and Argon [68], [69] initially proposed that plastic deformation was accommodated by the formation of shear transformation zones (STZ). The latter are regions of closely-packed atoms which preferentially rearrange under the application of a shear strain. Upon further deformation, the STZs percolate and form larger shear bands. It was reported that the motion of these shear bands causes structural changes of the MRO in the STZ as well as in the area surrounding them, so-called shear band affected zones [70], [71]. These modified regions were reported to modify the physical properties of some plastically deformed glasses such as lowering the activation energy for crystallization [72] or increasing the tensile ductility [73].

At temperatures close or above the T_g, three distinct behaviors are observed depending on the strain rate. At low strain rates, the flow remains Newtonian and uniform, while at higher strain rates BMGs exhibit inhomogeneous flow caused by non-Newtonian effects and ultimately shear localization as shown in Figure 1-9 for Vitreloy-1 [74]–[77]. The precise mechanism inducing this transition is still a subject of debate; however, a general consensus exists on the importance of the free volume. The formation of shear band is assumed to take place when the free volume increases locally which induces a decrease in viscosity and therefore a decrease in resistance to deformation. The increase in free volume could be induced either by structural disordering caused by the shear or by a local heating causing thermal expansion. On the other hand, free volume is thermally relaxed due to the annealing at the deformation temperature, which explains the temperature dependence.
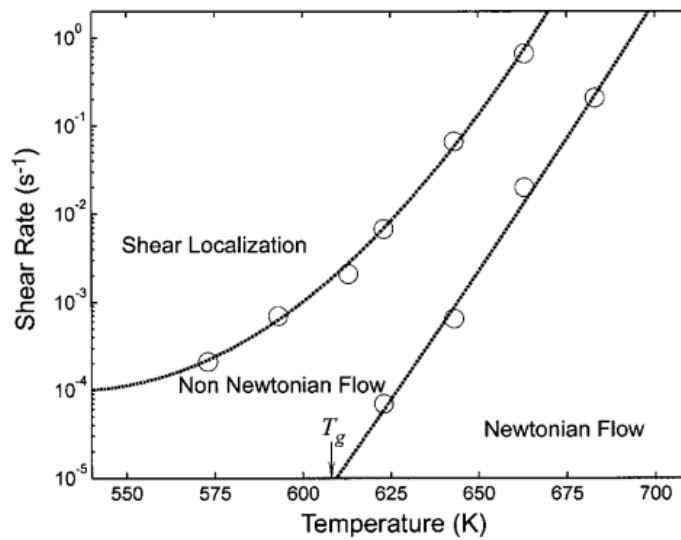
Figure 1-9 Map of the flow mechanism in function of the strain rate and temperature [76].

1.3.2 Factors affecting BMG properties

Influence of the temperature history

Metallic glasses are in a metastable state and therefore any annealing above their glass transition temperature will have an influence on their structure. Usually, BMG crystallization is studied via single temperature isothermal holding or fixed temperature ramp to form, respectively, TTT or continuous cooling transformation (CCT) diagrams. However, during processing a combination of steps is generally used; the BMGs are heated above T_g and then cooled down multiple times. The influence of such steps on the crystallization kinetics has been studied by Bordeenithikasem et al. [78] on a Zr-based and Pd-based BMG. They observed that in the case of several heating steps at the same temperature below the nose, the processing times could be simply added up and subtracted to the total time before crystallization of virgin sample to obtain the remaining time to crystallization. On the other hand, in the case of different processing temperatures, two opposite influences on crystallization were reported. If the second step is at a higher temperature, in the nucleation-controlled state, a much faster crystallization was observed. Indeed, the first heating induces fast crystal nucleation and the second one fast growing kinetics. Oppositely, if the first heating occurs at a high temperature, the time to crystallization at a lower temperature is only reduced by a small amount compared to a virgin sample. Similar observations were made on a $Au_{49}Ag_{5.5}Pd_{2.3}Cu_{26.9}Si_{16.3}$ BMG in which 5% crystallization was induced by slow cooling [79]. The TTT diagrams of fully amorphous and 5% crystallized BMG overlap at low temperature due to the growth-controlled kinetics. On the other hand, at higher temperature the sample with nanocrystals is shown to crystallize much earlier because of the shift to a nucleation-controlled phase.

Influence of the deformation

As mentioned in the previous section, mechanical deformation has an influence on the microstructure and can induce changes of free volume, viscosity and medium-range order beside others. Furthermore, it depends

strongly on the temperature and the deformation rate. It is therefore expected to have an impact on the crystallization kinetics as well.

Cao et al. reported that above a critical deformation degree, cold rolling of a Cu-based BMG enhanced the crystallization kinetics due to phase-separation. At low deformation, no influence on crystallization was observed [80]. Ma et al. demonstrated also faster crystal nucleation in cold-rolled CuZrAl BMG and attributed it to the formation of shear bands which modify the atomic structure and subsequently the nucleation thermodynamics. Moreover, the shear bands can reduce the viscosity locally which implies faster kinetics [72]. The influence of strain on two Pd-based BMG was compared by Mitrofanov et al. [81]. They reported that the crystallization temperature decreased more for the most stable glass and supposed that it was due to the alteration of the optimum short-range order configuration. Interestingly, they reported that above a critical strain no further influence is observed. Moreover, high-pressure torsion of a Pd-based BMG revealed via differential scanning calorimetry (DSC) the splitting of the crystallization peak into two crystallization processes at lower temperature after deformation [82]. They attributed the splitting to a change of the cluster ordering caused by the deformation.

Some contradictory observations have been reported concerning the influence of deformation in the SCLR depending on the BMGs and the deformation modes. Bae et al. analyzed the deformation behavior of $Cu_{47}Ti_{33}Zr_{11}Ni_6Sn_2Si_1$ BMG by tensile testing [83]. DSC characterizations of the specimen gauge and grip revealed the occurrence of crystallization only in the deformed area. Transmission electron microscopy (TEM) analyses confirmed the presence of nano-crystals. Several groups reported similar deformation-induced nanocrystallization in Zr-based BMG under tension and compression [84]–[86]. On the contrary, deformation-induced stability of the supercooled liquid has been reported for a Zr-based BMG tested in compression and a Ca-BMG in tension [87]–[89]. Several reasons could explain these apparent discrepancies. The stabilization mechanisms responsible for the high resistance against crystallization are composition dependent and therefore deformation will have a different impact. Moreover, the structural modifications are strongly dependent on the deformation temperature and rate. In general, crystallization was observed to be particularly enhanced at low temperature, just above the T_g, and at high strain rate.

Demetriou et al. [90] developed a model to predict the influence of shear rate on the crystallization kinetics and TTT diagrams. They assumed that the mechanism responsible for the deformation-induced crystallization was the increase in mobility. As exposed before, deformation increases the creation of free volume and enhances the atomic diffusion, which results in easier crystal nucleation. Based on several assumptions, they deduced an approximate shift induced on the TTT diagram of Vitreloy-1 (Figure 1-10). It is interesting to note that for a fixed shear rate, the shift increases with decreasing temperature. While the model is too simple to accurately predict the shift, it provides insight on the range of temperature and shear rate affecting the crystallization kinetics.
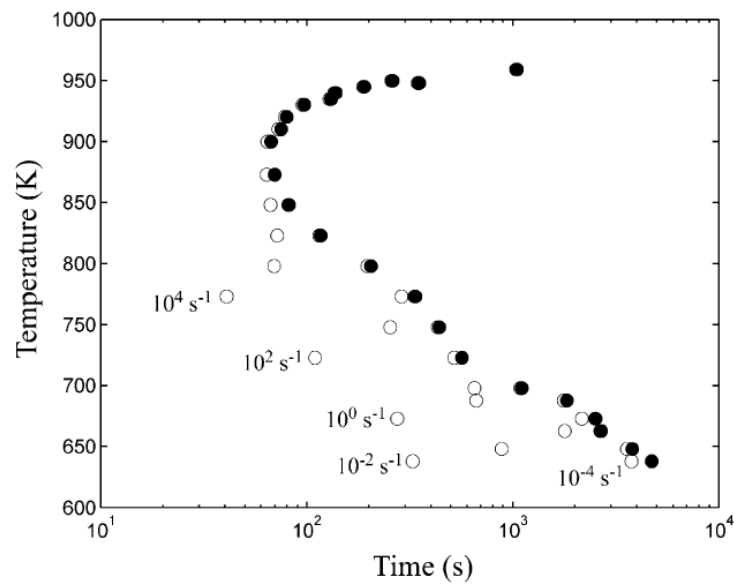
Figure 1-10 Simulated TTT diagram of Vitreloy-1 BMG for various shear rates [90].

Influence of the BMG dimensions

Different groups reported size dependent mechanical and thermophysical properties [48]. It was found that the room temperature deformation behavior evolves from heterogeneous for bulk samples to homogeneous for micro- or nano-sized samples leading to an increase in tensile plasticity [45], [50], [91]. Nevertheless, previously published studies are not consistent and the responsible mechanisms are still a subject of debate. Studies on nano-scale samples are indeed complex both in terms of processing and characterization due to the small sample size. The processing techniques used such as nanomoulding, focus ion beam (FIB) milling, sputtering or pulling may induce changes in the MG structure compared to the bulk MG which could then overlap with the presumed size effects [51], [92]–[94].

Finite size effects have also been observed in the SCLR for bulk metallic glasses of nm-scale size. Both the viscosity and the crystallization kinetics, which play a critical role to assess the formability of a material, strongly vary in the sub $\sim 100 \ nm$ range. Shao et al. [95] reported an increase in viscosity by a factor of five between a $100 \ nm$ diameter and a $40 \ nm$ Pt-based MG rod. They suggest that it is caused by the strong confinement which restricts the collective atomic motion with the STZs and increases the flow resistance. Several studies reported an increase in crystallization kinetics and proposed various origins. Gopinadhan et al. [96] analyzed 100 and 200 nm Pt-based nanorods, processed by extrusion, by DSC and HRTEM and demonstrated a decrease in crystallization temperature. Their results did not provide any evidence of surface and deformation effects, therefore they speculated that the faster nucleation rate was caused by composition fluctuations which are enhanced in small samples. On the other hand, Sohn et al. [97], [98] reported a similar dependence using in-situ heating TEM but assumed that it is caused by faster heterogeneous crystal nucleation at the surface. Faster surface crystallization has indeed been observed in many glass systems and attributed to higher surface mobility, local change in composition or decrease in total surface energy [99], [100]. Furthermore, they analyzed sub-50

nm samples and observed a subsequent increase in crystallization temperature and slower crystallization kinetics. They reported higher scattering in crystallization temperature and slower grain growth with decreasing diameter. This suggests that the slower crystallization kinetics are caused by a reduction in nucleation probability and apparent increase in viscosity as reported by Shao et al. [95].

1.4 Objective and outline of the thesis

The general theme of this thesis is the study of the fundamental mechanisms preventing the preservation of the fiber microstructure during thermal drawing, as well as during fiber device operation. More specifically, it consists in determining the key parameters controlling three specific phenomena: the thermal reflow of polymeric structures, the thermal shrinkage of thermally drawn polymer fibers, and the effect of thermal drawing on the crystallization kinetics of metallic glasses. For each phenomenon, we unravel novel insights in the mechanisms at play, and propose strategies to control or alleviate their effect. We also demonstrate novel materials and applications allowed by our findings. The thesis is then organized around three main themes:

1) Modelling of the evolution of the reflow of patterned surfaces during thermal drawing and the fabrication of sub-100 nm structures.

2) Analysis of the influence of thermal drawing parameters on the polymer morphology and induced thermal shrinkage and mechanical properties.

3) Identification and integration of bulk metallic glasses in polymer fibers, elucidation of the ultimate architectures and feature sizes achievable during thermal drawing, study of the influence of thermal drawing on the crystallization kinetics, and design of novel functional fibers based on the unique properties of BMGs.

The outline of this thesis can then be detailed as follow:

In the second chapter, we establish a model describing the evolution of the reflow during thermal drawing. We start by experimentally and theoretically studying the isothermal reflow of a texture imprinted on a polymer plate. We then use this analysis to develop a model which combines both the reflow and the down-scaling at different temperatures occurring during thermal drawing. We then compare our theoretical prediction and experimental data. Finally, we present some strategies that could be employed to reduce the reflow at the micro and nanoscale. By lowering the interfacial energy, we demonstrate the fabrication of a sub-100 nm structure on a thermally drawn polymer fiber.

The influence of thermal drawing parameters on the in-fiber polymer morphology, thermal shrinkage and mechanical properties is presented in chapter 3. We first demonstrate the influence of the drawing stress on the shrinkage behavior of polyetherimide fibers. We then present small and wide angle X-ray scattering analyses revealing the evolution of the degree of polymer chain orientation in function of the drawing stress. Moreover, we show that the thermal drawing parameters can be used to tune the mechanical properties. Then, we extend

our finding to fibers made of PMMAs of two different molecular weights. Thanks to our understanding of the temperature and processing stress dependent shrinkage, we fabricate a controllable irreversible bending fiber made of two PMMAs. Finally, we describe an annealing strategy to increase the thermal stability of fibers and demonstrate its efficiency with a thermal sensor fiber.

In chapter 4, we identify two BMG compositions which can be drawn inside polymer matrices: $Pt_{57.5}Cu_{14.7}Ni_{5.3}P_{22.5}$ and $Au_{49}Ag_{5.5}Pd_{2.3}Cu_{26.9}Si_{16.3}$. We first show different fiber structures and determine the ultimate feature size of Pt-BMG ribbons. We then present an analysis of the influence of thermal drawing on the crystallization kinetics in microscale and nanoscale ribbons via DSC, X-ray diffraction (XRD) and microstructure observation, and in-situ heating TEM analyses respectively. Next we turn to the Au-BMG having a lower GFA. We first describe the strategy used to find a suitable polymer cladding. The ultimate feature size and the crystallization kinetics are then presented.

In chapter 5, we show two novel applications of fibers integrating Pt-BMG electrodes in the field of neuroprobes and electrochemical sensing respectively. We first characterize the electrical and electrochemical stability of the Pt-BMG *in vitro*. Then, we present two different designs of multifunctional fibers which can be used for stimulation and recording for the first fiber, and recording and drug delivery for the second one. We demonstrate the good performance and stability of our electrodes during *in vivo* tests. Secondly, two designs of electrochemical sensing fibers integrating a three electrode system composed of two composite electrodes and one Pt-BMG electrode are presented. We demonstrate their ability to detect paracetamol via cyclic voltammetry or amperometry.

2 Submicrometer cross-section preservation via surface tension engineering

High aspect ratio constructs such as thin fibers and micro-channels with well-defined surface textures are gaining an increasing technological interest in a wide range of applications including scaffolds for nerve regeneration, microfluidics, health care monitoring and smart textiles. However, the fabrication of sub-micrometer textures onto thin fibers of tens-of-micrometers in diameter, or onto the inner wall of small micro-channels, is very challenging even with advanced lithography processes. The thermal drawing technique has been used to fabricate surface-patterned fibers, ribbons and micro-channels [5], [16], [18] with applications in textiles, photovoltaic cells or regenerative scaffolds [10], [16]–[18], [101].

As mentioned in the introduction, thermal reflow takes place during drawing due to Laplace pressure which limits the ultimate feature size of structures at the fiber level. This has been shown in previous publications, together with proposed practical strategies to alleviate this limitation [16], [18]. Nevertheless, no model describing the evolution of this reflow during thermal drawing has been presented. Such detailed understanding of the process remains essential to better characterize reflow and design arbitrary textures that can reach lower feature sizes. In order to be able to design strategies to delay this reflow, we establish here an analytical reflow model that can be applied to any periodic texture and demonstrate experimentally its validity during both isothermal annealing and thermal drawing experiments.

This chapter starts with the description and experimental characterization of the isothermal reflow of a texture imprinted on a thick polymer plate, which reveals the contribution of high frequency modes during the early stage of reflow. We then use this first analysis to tackle the problem of deformation during thermal drawing which combines reflow and monolithic scaling at different temperatures. We compare and show an excellent agreement between our theoretical prediction of reflow and experimental data taken at different positions along the preform-to-fiber region. This enables us to critically discuss several strategies that have been employed to enhance the cross-sectional preservation and show that lowering the reflow driving force holds the key for successful texturing of fibers and micro-channels at feature sizes as low as a few tens of nanometers. To illustrate this finding, we demonstrate the fabrication of sub-100 nm structures within a thermally drawn fiber by co-drawing two materials of low interfacial energy.

This chapter is initially based on a model developed by Dr. Nguyen Dang during his PhD at FIMAP and the work presented here has been continued in collaboration with him [16]. The majority of the content has been published in the following article:

T. Nguyen Dang#, I. Richard#, E. Goy, F. Sordo, and F. Sorin, "Insights into the fabrication of sub-100 nm textured thermally drawn fibers", *Journal of Applied Physics*, vol. 125, no. 17, p. 175301, May 2019, doi: 10.1063/1.5089022.

# The authors contributed equally to this work.

2.1 Reflow during isothermal annealing

2.1.1 Analytical model

At first, we consider the reflow deformation of a polymer surface texture under simple isothermal annealing. Furthermore, we restrict our investigation to a one-dimensional periodic pattern in the x direction with a profile $y(x) = h \cos(\frac{2\pi}{\lambda} x)$ with a periodicity λ and a height h significantly smaller than the substrate thickness d, as shown in Figure 2-1. Our analysis focuses on annealing temperatures slightly above the glass transition temperature. Therefore the polymer can be considered as a Newtonian incompressible fluid that flows in a regime of very low Reynolds number due to the high viscosity in this range. The latter is confirmed below when applying the model to specific polymers. Moreover, we consider the case where the height of the surface pattern is significantly smaller compared to its periodicity ($h \ll \lambda$), which allows the linearization of the Laplace pressure in the normal stress boundary condition between the polymer and air [102], [103]. A well-known solution of the velocity (u_x, u_y) field in such a configuration is a periodic function in x that decays exponentially in the bulk (y-direction). Applying the kinematic boundary condition allows us to relate u_y with the change of height over time, leading to a simple first order differential equation $\frac{\partial h}{\partial t} = -\frac{h}{\tau}$, and hence $h(t) = h(0) \exp\left(-\frac{t}{\tau}\right)$ with the characteristic reflow time $\tau = \frac{\eta \lambda}{\pi \gamma}$, with η the viscosity of the polymer, and γ its surface tension [16], [104], [105].
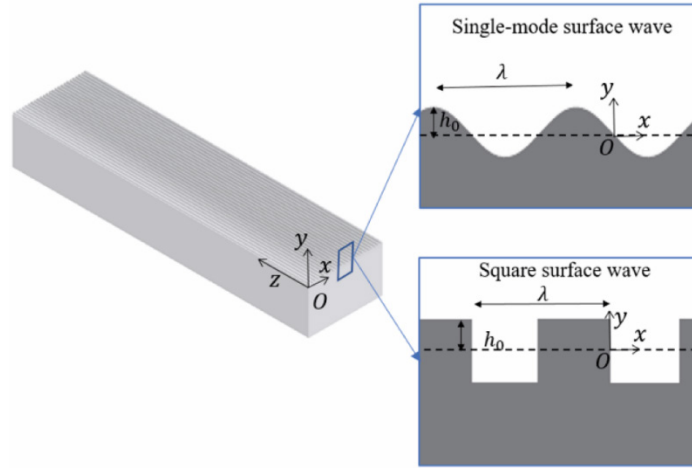
Figure 2-1 Schematics of a sinusoidal surface wave and a square surface wave

This solution for a single harmonic can be used to treat the case of an arbitrary periodic texture $y(x)$. Assuming that all patterns are regular functions that verify the Dirichlet conditions, $y(x)$ can be written as the sum of sine and cosine modes, with each mode having a period $\lambda_n = \lambda/n$. Because of the linearization conditions we applied above (low Reynolds number, and $h<<\lambda$), the Navier-Stokes equations governing the velocity field as well as the boundary conditions are all linear relations. It is then straightforward to realize that injecting $y(x)$ in these equations will project each harmonic into a set of similar equations as described above for a single harmonic [102]. In other words, each mode will decay with a similar expression $h_n = h_{n0} \exp\left(-\frac{t}{\tau_n}\right)$, where h_{n0} is the nth-Fourier term of the original shape, and $\tau_n = \tau/n$. To verify experimentally this analysis, we apply our model to a square wave texture as shown in Figure 2-1 (bottom) with an initial height of h_0. The Fourier transform of such function is known to be $y(x) = \frac{4h_0}{\pi} \sum_n \frac{(-1)^n}{(2n+1)} \cos\left(\frac{2\pi(2n+1)}{\lambda} x\right)$. Since each mode $h_n = \frac{4}{\pi} \frac{(-1)^n}{(2n+1)} h_0$ evolves like described above, we have a time evolution of the texture given by

$$y(x,t) = \frac{4h_0}{\pi} \sum_n \left(\frac{(-1)^n}{(2n+1)} \mathrm{e}^{-(2n+1)\frac{t}{\tau}}\right) \times \cos\left(\frac{2\pi(2n+1)}{\lambda} x\right) \quad (2.1)$$

A measurable value that can be simply defined is the height of the structure as it reflows at $x = 0 \ [\lambda]$, which will have the following evolution:

$$\frac{h(t)}{h_0} = \frac{4}{\pi} \sum_n \left(\frac{(-1)^n}{(2n+1)} \mathrm{e}^{-(2n+1)\frac{t}{\tau}}\right) \quad (2.2)$$

2.1.2 Experimental verification

In order to verify this theoretical description, we carried out isothermal reflow experiments on micro-imprinted PMMA samples. The imprinting and annealing processes are illustrated in Figure 2-2. First, we made two polydimethylsiloxane (PDMS) molds with periodical square patterns with period λ and total height $2h_0$ of 20 μm and 40 μm, respectively. The patterns were transferred to PMMA plates by hot pressing. Finally, the annealing

procedure was carried on in an oven at $130^oC \pm 2^oC$ for various durations. Typical cross-sections of imprinted samples before and after annealing are shown in Figure 2-2.
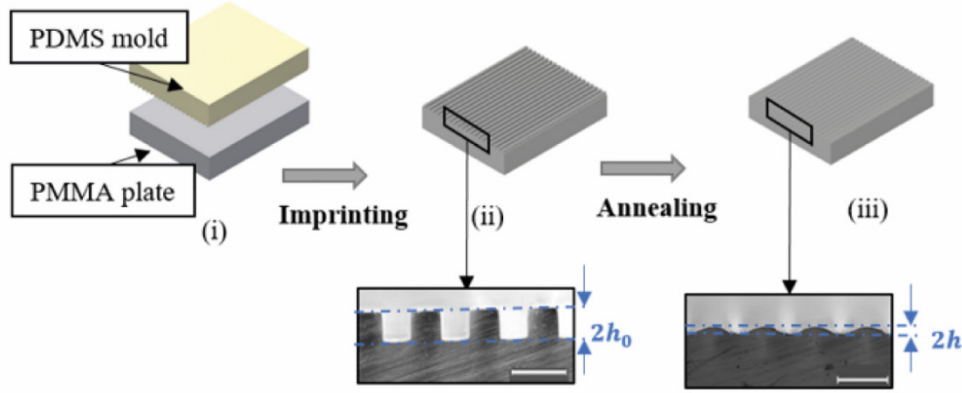
Figure 2-2 Schematics of the imprinting and annealing experiments and the cross-section of a sample after each step

In order to calculate the theoretical reflow, we used a surface tension $\gamma = 33\ mN/m$ at 130^oC from [106]. Furthermore, we measured the temperature dependent viscosity and from the experimental data, a fitted expression of the temperature-dependent viscosity was obtained (Figure 2-3):

$$\eta_{PMMA}\big(T(K)\big) = \exp\left(\frac{16184}{T} - 22.41\right) \tag{2.3}$$

From this fit we can extrapolate the values of the viscosity at different temperatures. In particular, we obtain that $\eta(128^oC) \approx 6.14 \times 10^7\ Pa.s, \eta(130^oC) \approx 5.0 \times 10^7\ Pa.s$ and $\eta(132^oC) \approx 4.1 \times 10^7\ Pa$ with $T(K) = T(^\circ C) + 273.15.$
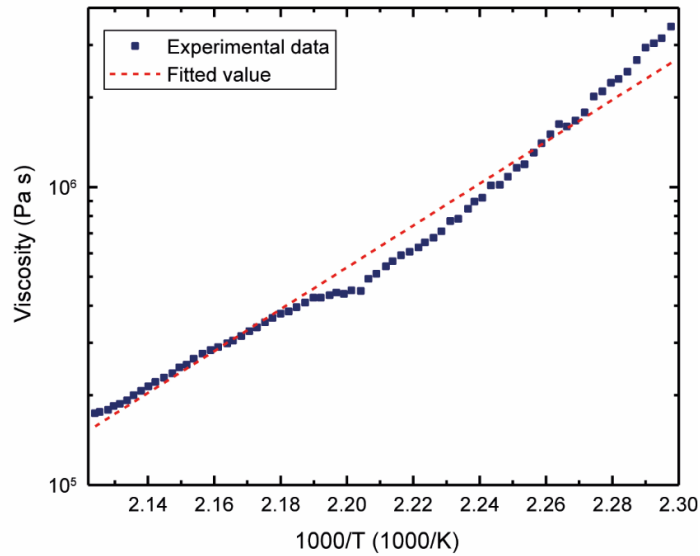
Figure 2-3 Experimental and fitted values of PMMA viscosity in the temperature range from $160\ ^oC$ to $200\ ^oC$

We can first verify some hypotheses we stated to develop our model. In these experiments, the Reynolds and the Capillary numbers were $Re = \frac{\rho U h}{\eta} \approx 10^{-5} \ll 1$ and $Ca = \frac{\eta U}{\gamma} \approx 1$, with $U = \frac{h_0}{\tau} \approx 10^{-5} \ (m/s)$ and $h = h_0 \approx 10^{-5} \ (m)$, which justifies our earlier approximation of neglecting the inertial term in the Navier-Stokes equations.

Figure 2-4 displays the experimental and theoretical values obtained with PMMA. A standard deviation of $\Delta h = 2 \ \mu m$ was measured on several samples and is shown by the vertical error bars. The theoretical values determined by Equation 2.2 are shown by three dashed lines corresponding to the temperature uncertainties in the oven, i.e. one theoretical curve for 128°C, 130°C and 132°C. We note that our analysis considered $h_0 \ll \lambda$, which is initially not completely satisfied, especially when considering the high order modes. However, the contribution of these modes decays much faster than the first-order ones (as $\tau_n = \tau/n$), and disappears over a time scale negligible compared to the overall process. The excellent agreement between Equation 2.2 and experimental data further confirms that our model captures well the overall dynamic of the system despite the linearization approximation.
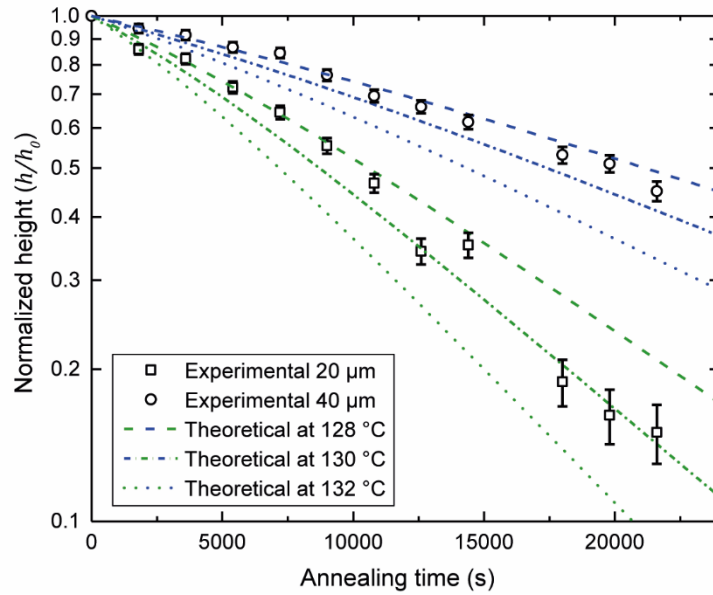
Figure 2-4 Theoretical (dashed lines) and experimental decay (square and circular dots) of the normalized amplitude of an annealed square surface as function of annealing time. The green and blue lines correspond to the patterns with a period of 20 and 40 μm, respectively.

2.2 Reflow during thermal drawing

2.2.1 Analytical model

We then exploit this first study to tackle the case of the thermal drawing of a pattern on the surface of a preform. The same approximation can be made regarding the incompressibility of the polymer and the low Reynolds number flow during thermal drawing as shown before [14], [107], [108]. This time however, as we schematically show in Figure 2-5, the drawing process entails a non-isothermal reflow with a scaling down of all the cross-

sectional geometrical parameters as the fiber is being formed. The periodicity λ of an arbitrary pattern is no longer unchanged during the reflow because of the scaling, h_0 is subjected to reflow and scaling simultaneously, and the surface tension γ and viscosity η are also varying because the temperature varies strongly along the length of the furnace.
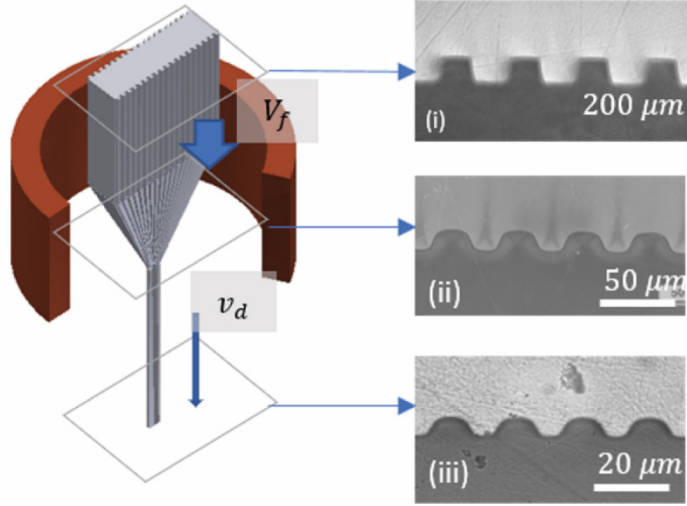
Figure 2-5 Schematics of the drawing process with i, ii, iii: micrographs of the cross-sectional cut at different positions from the preform to the fiber

To model this problem, we can consider the evolution of the surface pattern along an infinitesimal length dz of the preform-to-fiber axis [109]. The overall change of height results from the sum of two types of deformation, the scaling deformation $dh_{sc}(z)$ coming from the drawing process and the thermal reflow deformation $dh_{re}(z)$. The former results from simple volume conservation and can be expressed as $dh_{sc}(z) = -\frac{1}{2}\frac{h}{v}\,dv$ with $v = v(z)$ being the fluid velocity along the furnace axis considered uniform in the cross-section. The latter follows a similar evolution as described above since between z and $z + dz$ we can consider an isothermal reflow at $T(z)$ for a period of (dz): $dh_{re}(z) = -\frac{h}{\tau(z)}\,dt$, with a corresponding time $dt = \frac{dz}{v(z)}$.

This evolution can also be derived for a square pattern using again a spectral approach. The reflow between the positions z and $z + dz$ applies to each mode as explained above. The scaling down is also a uniform transformation that applies to all modes. Hence, we can write for each mode:

$$\frac{dh_n}{h_n(z)} = -\frac{1}{2}\frac{dv}{v(z)} - \frac{dz}{v(z) \times \tau_n(z)} \tag{2.4}$$

which gives for each mode: $h_n(z) = \left(\frac{v(z)}{V_f}\right)^{-\frac{1}{2}} \exp\left(\int_{-z_0}^{z} -\frac{1}{v(z)\,\tau_n(z)}\,dz\right)$, where we fix the center of the furnace at $z = 0$, $-z_0$ represents the top of the furnace, and V_f is the preform feeding speed. The expression of the amplitude for a square pattern, following our calculations in Equation 2.2, is finally written as:

$$h(z) = \frac{4h_0}{\pi} \left(\frac{v(z)}{V_f}\right)^{-\frac{1}{2}} \sum_n \frac{(-1)^n}{(2n+1)} \exp\left(\int_{-z_0}^{z} -\frac{(2n+1)}{v(z)\,\tau(z)} dz\right) \tag{2.5}$$

Due to the volume conservation, we can write $\left(\frac{V_f}{v(z)}\right)^{-1/2} = \frac{\lambda_0}{\lambda(z)}$, thus Equation 2.5 can be rearranged to define a dimensionless quantity that we name the shape factor f_{shape} :

$$f_{shape}(z) = \frac{h(z)}{h_0}\frac{\lambda_0}{\lambda(z)} = \frac{4}{\pi} \sum_n \frac{(-1)^n}{(2n+1)} \exp\left(\int_{-z_0}^{z} -\frac{(2n+1)}{v(z)\,\tau(z)} dz\right) \tag{2.6}$$

This shape factor is a quantitative measure of the preservation of the structure in a drawing process. It varies from 0 to 1, with $f_{shape} = 1$ corresponding to a perfect preservation of the cross-sectional shape, whereas $f_{shape} = 0$ corresponds to a complete collapse of the structure.

2.2.2 Experimental verification

To verify experimentally this analysis, a $200\ \mu m$-square pattern was embossed onto a thick PMMA plate following the same procedure than for the annealing experiment. The preform was then thermally drawn into a fiber as shown in Figure 2-5, with a feeding (V_f) and a drawing speed (v_d) fixed at $1\ mm/min$ and $100\ mm/min$ respectively. To evaluate the shape factor according to our analysis (the right-hand side of Equation 2.5) in such an experiment, we must know the material viscosity $\eta(T(z))$ and surface tension $\gamma(T(z))$, as well as the drawing speed v(z), at all z positions. The temperature distribution along the furnace axis was measured with a thermocouple and fitted with a quadratic profile $T(z) = T_0 - a \cdot z^2$, with $T_0 = 170 \pm 2\ (^oC)$ and $a = 1.43\ (^oC \cdot cm^{-2})$, fixing the center of the furnace at $z = 0$. Knowing the dependence of the viscosity on temperature, we can extract $\eta(z)$. The surface tension of PMMA was taken as: $\gamma(T) = 41.1 - 0.078 \times T(^oC)$ [106]. Finally, we use the expression of $v(z)$ developed in section 1.1.3 and given by :

$$v(z) = \exp\left(\ln V_f + \frac{\int_0^z \frac{dz}{\eta(z)}}{\int_0^L \frac{dz}{\eta(z)}} \frac{v_d}{V_f} \right) \tag{2.7}$$

The theoretical value obtained is shown as three dashed lines corresponding to the temperature uncertainties in Figure 2-6. The large uncertainty in the model results from the difficulty to measure accurately the temperature inside the furnace. Even taking a conservative uncertainty of $\pm 2\ °C$ for the measured temperature, the induced variation of viscosity leads to an uncertainty of around 10 %.

To confront this theoretical value to experimental data, we measured experimentally the evolution of the parameter $\frac{h(z)}{h_0}\frac{\lambda_0}{\lambda(z)}$ during the draw. To do so, we stopped the feeding and drawing simultaneously when the drawing process became steady and removed the preform-to-fiber construct from the furnace. We then cut and polished the exposed cross-section at several positions along the z-axis. Figure 2-5 shows three examples of the preform-to-fiber cross-sections at the preform level, in the neck-down region, and at the fiber level respectively.

We could then image with an optical microscope these cross-sections and measure the height of the structure $h(z)$ and its period $\lambda(z)$ to obtain the shape factor at different positions. The experimental data are plotted in Figure 2-6 and compared with the theoretical value described above, with a very good agreement observed. The vertical and horizontal error bars correspond to the statistical standard deviation of the height measurement of the patterns and the distance measurement of each cut to the top of the preform, respectively.
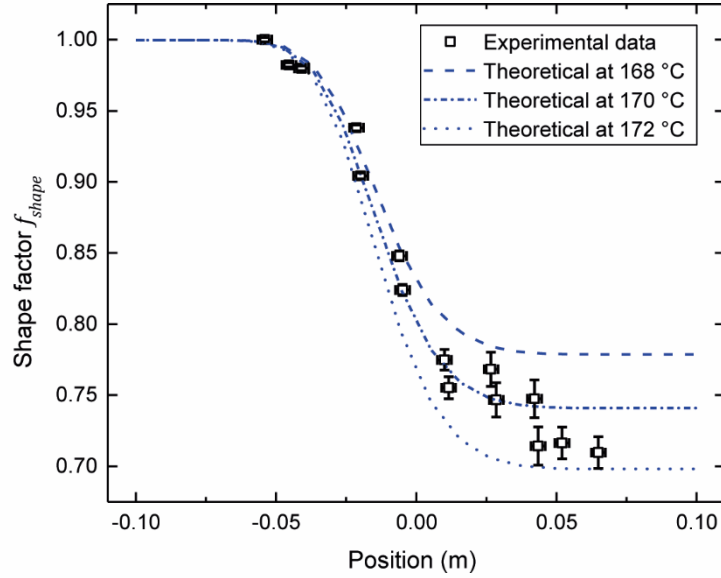
Figure 2-6 The experimental and theoretical shape factor along the drawing direction. The lines correspond to the calculated value of the shape factor with $T_0 = 168\ ^oC, 170\ ^oC$ and $172\ ^oC$, respectively.

2.3 Strategies to reduce thermal reflow

2.3.1 Reflow theoretical prediction

Since our model now accounts for the evolution of the pattern during the entire fiber drawing process, we can use it as a tool to better understand reflow during fiber processing and propose strategies to prevent reflow, i.e. keep f_{shape} with a value close to 1. From Equation 2.6, we see that one way to do so is to make τ as high as possible, as $f_{shape} \xrightarrow[\tau \to \infty]{} 1$. τ being proportional to the viscosity and inversely proportional to the surface tension, for a targeted pattern size λ at the fiber level, one can either increase the viscosity η or decrease the surface tension γ of the drawn materials. The former route was exploited for example by using high-mechanical-strength polymers, such as polyetherimide (PEI), which led to the fabrication of textured fibers with feature size as small as $20\ \mu m$ [10], [17]. Reducing the temperature of the preform surface during drawing to locally lower the viscosity at the texture level was also used to reach sub-micrometer feature sizes [18]. Nevertheless, there is an upper limit to the viscosity at which a steady draw can be performed which ineluctably limits the achievable feature sizes.

An alternating approach consists in decreasing the surface tension contribution by interfacing the patterned surface of a preform with another polymer during drawing. As a result, the driving force of the thermal reflow

deformation becomes the interfacial tension between the two polymers, which can be chosen to be much smaller than the surface tension of either component. It was previously shown that a square pattern with 300 nm feature size could be obtained by thermally drawing a multi-material polycarbonate (PC)/polyethylene(PE) fiber [109]. Contrary to a PC-only fiber, the PC/PE could maintain the structure because the interfacial tension between the two polymers (6.9 mN/m at 20^oC) is more than 5 times lower than between PC and air [106], [110]. It appeared that while the PC/PE system enables the maintaining of a shape factor close to 1 for a 300 nm -feature-sized pattern (the feature size is defined as half of the period, corresponding to the width of an individual groove), it decreases quickly to 0 when feature size gets to sub-100 nm region (see below). An alternative pair of polymers to maintain feature sizes down to 100 nm at the fiber level is PC/PMMA. This pair of materials can be co-drawn and has an estimated surface tension of 0.39 mN/m (see below) more than an order of magnitude below the one of PC and PE.

To estimate the smallest feature size which can resist to the thermal reflow during drawing, we calculated the final shape factor at the fiber level, where $z = L$, as follows:

$$f_{shape}(z = L) = \frac{4}{\pi} \sum_n \frac{(-1)^n}{(2n+1)} \exp\left(\int_0^L -\frac{(2n+1)}{v(z)\,\tau(z)} dz \right)$$

We assumed a draw-down ratio of 20 ($V_{feed} = v(0) = 1\ mm/min$ and $V_{draw} = v(L) = 400\ mm/min$). We estimated the temperature profile following the same procedure than with PMMA and obtained $T(z) = 190(^oC) - 14300 \times z^2$. The viscosity of PC was measured experimentally (Figure 2-7) and fitted by a modified Arrhenius temperature dependence as:

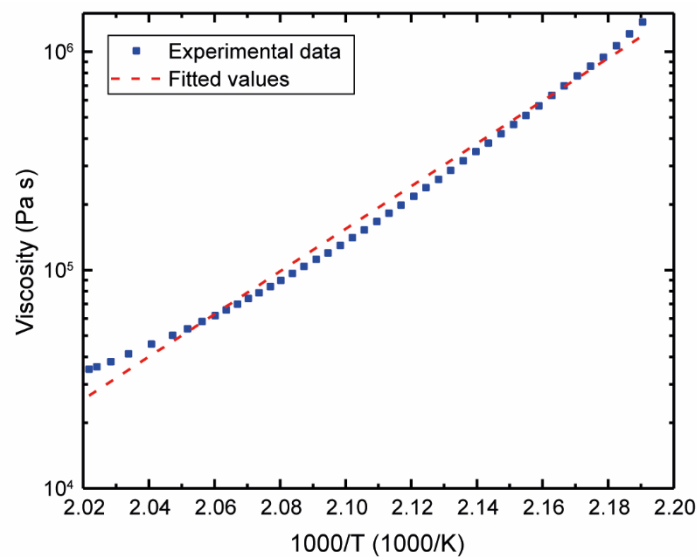$$\eta_{PC}(Pa.s) = \exp\left(\frac{22493}{T(^oC) + 273.15} - 35.287 \right)$$

Figure 2-7 Experimental and fitted values of PC viscosity in the temperature range from 180 ^oC to 220 ^oC

The value of the interfacial tension between PC and PE was reported as $\gamma_{PC/cPE} = 6.9 - 0.018 \cdot (T(^oC) - 20)$ $\left(\frac{mN}{m}\right)$ [106], [110], [111]. The value of interfacial tension between PC and PMMA was estimated using the approximation $\gamma_{PC/PMMA} = \gamma_{PC} + \gamma_{PMMA} - 4\frac{\gamma_{PC}^d \gamma_{PMMA}^d}{\gamma_{PC}^d + \gamma_{PMMA}^d} - 4\frac{\gamma_{PC}^p \gamma_{PMMA}^p}{\gamma_{PC}^p + \gamma_{PMMA}^p}$ proposed by Wu Souheng [110], where γ_i^d and γ_i^q ($i = PC, PMMA$) correspond to the dispersive and polar components of each surface tension. With the following value of surface tension taken from the Chemical Abstract Series (24936-68-3 for PC and 25087-26-7 for PMMA), $\gamma_{PC} = 43.4 \left(\frac{mN}{m}\right)$, $\gamma_{PC}^d = 38.2 \left(\frac{mN}{m}\right)$, $\gamma_{PC}^p = 5.2 \left(\frac{mN}{m}\right)$ and $\gamma_{PMMA} = 41.0 \left(\frac{mN}{m}\right)$, $\gamma_{PMMA}^d = 35.9 \left(\frac{mN}{m}\right)$, $\gamma_{PMMA}^p = 7.8 \left(\frac{mN}{m}\right)$, we obtain $\gamma_{PC/PMMA} \approx 0.39 \left(\frac{mN}{m}\right)$.
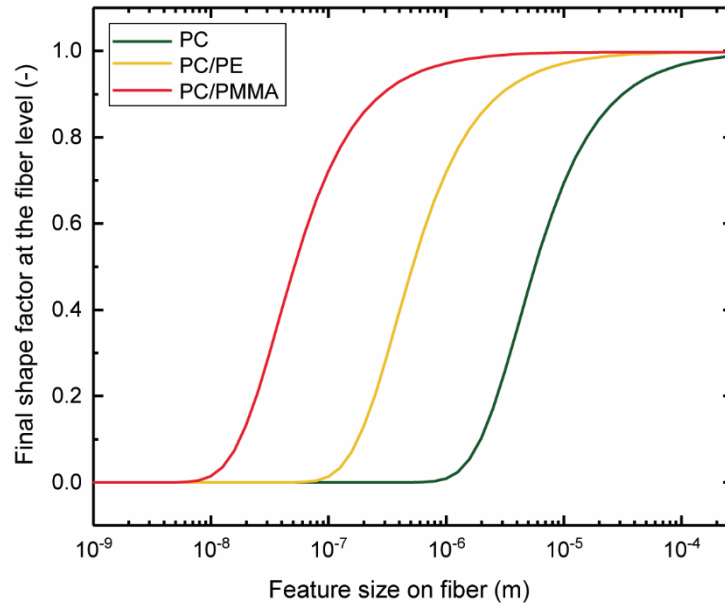
Figure 2-8 Calculated value of the shape factor at the fiber level versus the targeted feature size of the texture for PC, PC/PE and PC/PMMA systems

Using these values, we were able to calculate the theoretical value of the shape factor at the fiber level as a function of the feature size on fiber for the PC/air, PC/PE and PC/PMMA system and the results are displayed in Figure 2-8. It can be seen that adding a sacrificial polymer layer allows us to reach sub-1 μm feature sizes. While the PC/PE system enables us to maintain a shape factor close to 1 for a 500 nm -feature-sized pattern (the feature size is defined as half of the period, corresponding to the width of an individual groove), it decreases to 0 when the feature size reaches the sub-100 nm region. At the same time, the PC/PMMA system allows the final shape factor at the fiber level to remain close to 1 at 100 nm feature-size.

2.3.2   Thermal drawing of sub 100-nm patterned fibers

To verify experimentally this analysis, we fabricated a cylindrical preform with a textured PC core surrounded by a PMMA cladding that we drew a first time to obtain a submillimeter scale fiber as shown in Figure 2-9(a-i). We then assembled several of these fibers and drew them a second and third time to reach sub-100 nm features. Figure 2-9(a-ii) shows the fiber cross-section after the second draw. In Figure 2-9(b) and (c) we show cross-

sections after the second and third draw, respectively, where the PMMA was etched by dipping the fibers into acetic acid to expose the PC free surfaces. While imaging at this scale is challenging, the SEM micrographs reveal patterned fibers drawn with sub-micrometer diameter, on which textures are maintained with feature sizes well below 100 nm, around 20-30 nm in terms of height.
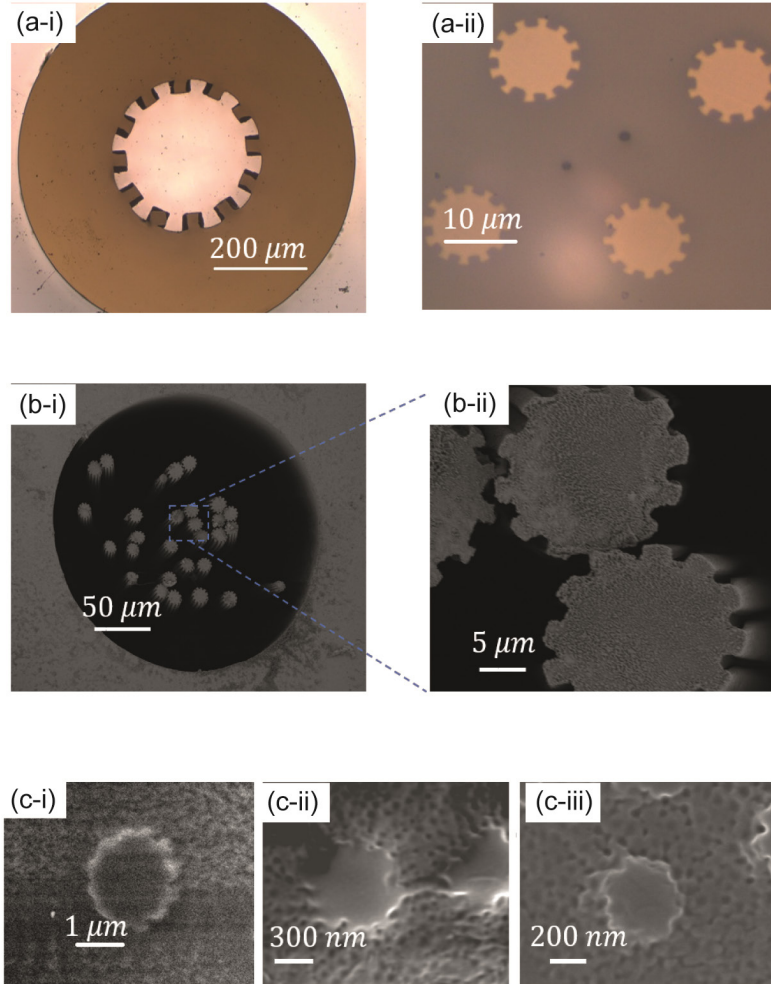
Figure 2-9 (a-i) and (a-ii) Optical micrographs of the once-draw and twice-draw PC textured fibers covered by PMMA cladding, respectively. (b) SEM micrographs of twice-drawn fiber after dissolution of PMMA. (c) SEM micrographs of thrice-drawn fibers with sub-100 nm feature-size at different draw-down ratio

2.4 Summary and conclusion

In conclusion, we presented in this chapter an in-depth theoretical and experimental study of the thermal reflow deformation of polymer surfaces in isothermal and in thermal drawing conditions. Analytical descriptions of the deformation of a square wave were obtained and showed very good agreement with experiment data. We showed that by decreasing the driving force of the reflow, we could keep the sharpness of the structure at a micrometer scale and achieved sub-100 nm patterned fibers. The simplicity of our model can be applied to multiple fiber shapes and periodic structures, allowing for a variety of configurations to be engineered. This paves the way towards the design of advanced fibers for novel applications in optical waveguides,

bioengineering, microfluidics or deformation sensing [5], [13], [112], [113]. Beyond thermal drawing, the theoretical framework presented herein could find an interest in other processes such as for fiber spinning techniques or for post-processing methods in micro-lens fabrication [114].

While the agreement we achieved is very good, our model still involves some assumptions that could be alleviated in future research. Numerical solutions could be developed in order to take into account the nonlinearity of the Laplace pressure for patterns with a height larger than the periodicity (h<λ). In addition, our model could be extended to non-Newtonian fluid and the coupling between the thermal reflow and drawing scaling could also be considered to refine the model, particularly for materials with a strong non-Newtonian behavior.

2.5 Materials and experimental methods

Materials: PMMA (Plexiglas) plates and PC rods were purchased from Boedeker, while the PMMA films were obtained from Goodfellow. Chlorotrimethylsilane and the PDMS pre-polymer (Sylgard 184) were purchased from Sigma Aldrich and Dow Corning, respectively.

Preform making: The silicon masks were patterned using photolithography at the Centre for Microfabrication (CMi) of EPFL. First, Chromium-coated masks were fabricated with a Heidelberg DWL200 laser writer and then transferred to silicon wafers coated with a photoresists (ECI), using a photolithography line (RiteTRack 88 Series Coater and Developer and Süss MA6/BA6 mask aligner). The silicon masks were etched with a plasma etcher Alcatel AMS 200 SE. The masks were then passivated with chlorotrimethylsilane by vapor deposition and casted with a PDMS pre-polymer with a crosslink agent (10:1 wt ratio). The PDMS molds were cured at $80\,°C$ for 4 hours before being removed from the Si masters. Two PDMS molds were made with periodic square patterns of period and height of $20\,\mu m$ and $40\,\mu m$, respectively. The patterns were transferred to PMMA plates by hot pressing at $175\,°C$ under a pressure of $0.1\,MPa$. The heating speed and cooling speed were fixed to $5\,°C$ per minute to avoid any residual stress.

For the circular PC fiber, a square texture of $1\,mm$ was milled on a $1.6\,cm$ diameter PC rod. Then PMMA films were tightly rolled around the bar and consolidated in an oven under vacuum (France Etuves) at $150\,°C$ for about 10 minutes. After consolidation, the PMMA had only partially flown inside the grooves but it flew during the first draw due to the lower viscosity of PMMA. For the second and third draw, several fibers were inserted in a PC tube to form the new preform.

Thermal drawing: The fibers were drawn in a custom-made drawing tower with three heating zones. For the PMMA fiber, the set temperatures were $120\,°C$, $250\,°C$ and $85\,°C$ and the feeding speed and drawing speed $1\,mm\,min^{-1}$ and $100\,mm\,min^{-1}$ respectively. The PC-PMMA circular fibers were drawn at set temperatures of $150\,°C$, $270\,°C$ and $85\,°C$ with a feeding speed of $1\,mm\,min^{-1}$ and drawing speed between 100 and $400\,mm\,min^{-1}$. Note that the real temperatures inside the tower are lower.

Rheological characterization: PC and PMMA circular plates of diameter 2.5 cm and thickness 1.5 mm were hot pressed. The measurements were carried out in a rheometer AR2000 (TA Instrument) with a shear rate of 0.1 s^{-1}.

Thermal annealing: Samples were annealed in a vacuum oven (France Etuves).

Optical microscopy: The samples for the cross-sections were obtained by cutting and polishing the exposed surface of the polymer fibers with SiC papers P4000 (Struers). In order to etch the PMMA from the PC-PMMA fibers, the polished tip was dipped briefly in acetic acid. Images were taken using a Leica DM 2700M optical microscope.

Scanning electron microscopy: Fibers were coated with a 10 nm carbon film and images were taken using a Zeiss Merlin field emission SEM (Zeiss, Göttingen) equipped with a GEMINI II column.

Height measurement: The height of the patterns was measured with a UBM laser profilometer.

3 Influence of thermal drawing on the polymer morphology

The final properties of polymers depend on their morphology, which is largely determined by the fabrication process. In particular, the latter affects the amount of crystallized domains and their orientation, as well as the degree of orientation of amorphous regions [115], [116]. As discussed in the introduction, this orientation induces anisotropic properties and has a significant impact on the mechanical properties and the failure mechanisms [117]. In addition, the chain alignment leads to a rise in entropic energy due to the out-of-equilibrium conformation. Consequently, an increase in temperature induces macroscopic shrinkage due to the chain relaxation into random coil conformations [33].

Depending on the final application of the thermally drawn fibers, different thermomechanical properties are required such as high strength, and high dimensional stability at high temperature or in aqueous environment [6], [43]. Even though the influence of the drawing parameters on some fiber properties has been reported [42], [43], no in-depth study at the microscopic level has been carried out. A precise understanding of this phenomenon is however essential to predict the final properties of the fiber and subsequently tune the processing parameters and perform post heat-treatment in order to expand its performance and resilience, and meet the targeted requirements.

In this chapter, we analyze the influence of the drawing parameters on the polymer microstructure, the fiber shrinkage behavior when annealed, and on its mechanical properties. We first focus on polyetherimide (PEI) fibers yet our conclusions can be applied to a wide range of thermoplastic materials. In order to clarify the change in morphology, small- and wide-angle X-ray scattering (SAXS, WAXS) experiments are carried out which give an insight on the presence of anisotropy trapped-in the fibers. This study is then extended to other PMMA fibers and a heat-controlled bending fiber is designed. Finally, an annealing procedure is proposed to relax the fibers and the thermomechanical properties are correlated with structural change through additional SAXS and WAXS experiments. To highlight the scientific and technological impact of our study, we apply this to a temperature sensing fiber device for heat monitoring in protective garments.

The SAXS and WAXS experiments were performed by A. Maurya at the Center for X-ray Analytics, EMPA.

3.1 Shrinkage behavior

We started by investigating the influence of drawing parameters on the shrinkage of thermally drawn fibers upon annealing. The thermal drawing process is controlled by varying the oven temperature and the draw down ratio, defined as $ddr = \sqrt{\frac{v_d}{v_f}}$ where v_d and v_f are the drawing and the feeding speed, respectively. Both have a significant impact on polymer flow, since they determine the viscosity, the deformation rate and the total deformation. Their influence can

be correlated to the drawing stress, which is continuously monitored during the draw. The latter increases when the temperature is reduced or the drawing speed is increased. To assess the influence of these parameters on the final morphological structure and thermomechanical properties of thermally drawn fibers, two sets of pure rectangular PEI fibers (T_g = 214 $°C$) were processed by either varying the drawing temperature from 360 $°C$ to 340 $°C$ at a ddr of 15, or keeping the drawing temperature constant at 350 $°C$ and varying the ddr from 10 to 40 (Figure 3-1(a)). Few meters of fibers were drawn upon changing settings to ensure a stable state is reached. A wide range of drawing stresses was therefore obtained, spanning from 1.1 to 17.5 MPa (Table 3.1).
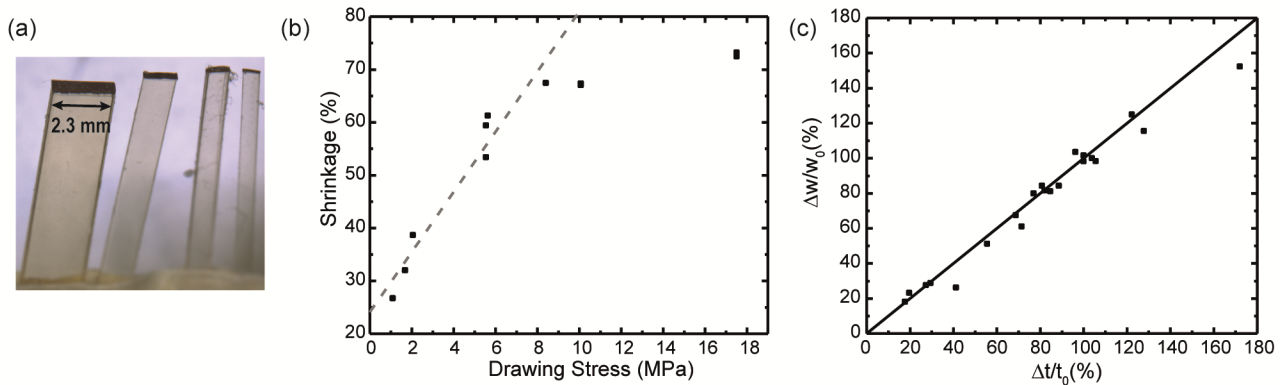
Figure 3-1 (a) Photograph of PEI fibers (b) Total shrinkage after annealing 225 $°C$ in function of the drawing stress. The dash line respresents the linear fitting between 0.8 and 8 MPa. (c) Relative changes in width and thickness after annealing at 225 $°C$. A line of slope 1 is added for easier visualization.

Figure 3-1(b) shows the shrinkage ratio, defined by $S = \frac{L_0 - L_1}{L_0} \times 100$, with L_0 the initial length and L_1 the length after a 10 min annealing above the T_g as a function of the drawing stress. The shrinkage ratio increases first linearly with the drawing stress before stabilizing at values as high as 75 % for stresses above 8 MPa. This upper limit is related to the maximum orientation and elongation of the polymer chains induced by the thermal drawing process. Furthermore, a proportional increase in thickness and width is observed, which confirms the isotropic behavior of the fibers in the transverse directions (Figure 3-1(c)).

Table 3.1 PEI fiber drawing parameters, cross-sectional dimensions and deduced drawing stresses

Set temperature ($°C$)	DDR	Cross-section (mm^2)	Drawing stress (MPa)
360	15	0.78	1.1
350	15	0.78	1.7
350	15	0.77	5.6
330	15	0.91	8.4
350	10	1.6	2.1
350	20	0.44	5.5
350	30	0.24	10.2
350	40	0.12	17.5

Additional thermomechanical tests were performed in a dynamic mechanical analyzer (DMA) in order to record the evolution of retractive stresses upon heating of the fibers in the condition where their extremities were fixed (Figure

3-2(a)) and of deformation without constraint (Figure 3-2(b)). In Figure 3-2(a), fibers drawn between 1.1 and 8.4 MPa are characterized first by a negative stress developing in the fiber to compensate the thermal expansion, then an increase in stress while approaching the T_g and a maximum just above it. When the relationship between the maximum stress and the drawing stress is plotted, interestingly a linear correlation is obtained independent of the varied parameters, the temperature or the drawing speed (Figure 3-2(c)-top). This reveals that most of the frozen entropic stresses induced in the fiber during processing is preserved. Furthermore, a variation in the peak stress temperature can be observed, decreasing from 232 $°C$ for the fiber drawn at the lowest stress (i.e. highest temperature) to 222 $°C$ for the highest drawing stress. Turning now to the strain experience by heating the fibers without constraints (Figure 3-2(b)), it respects first a linear behavior, whose slope corresponds to the thermal expansion, followed by a sharp drop when irreversible shrinkage takes place. In Figure 3-2(c)-middle graph, we show that the temperature of the inflection point, corresponding to the overtaking of the shrinkage force, is characterized by first a strong decrease with the drawing stress and then seems to reach a plateau at a temperature as low as 130 $°C$ for the fiber drawn at 17.5 MPa. The occurrence of shrinkage far below T_g might be explained by the reduction in chain entanglement in oriented polymers, which results in a greater ease with which the polymer chains can slip [118]. The frozen-in entropic forces could also be sufficient to compensate the thermal activation to overcome local barrier potentials and allow polymer flow [119]. Furthermore, some studies suggest that in addition to entropic forces, intra-chain enthalpic forces can emerge due to chain stretching via the entanglement network and could explain the apparition of shrinkage much below the T_g [120].
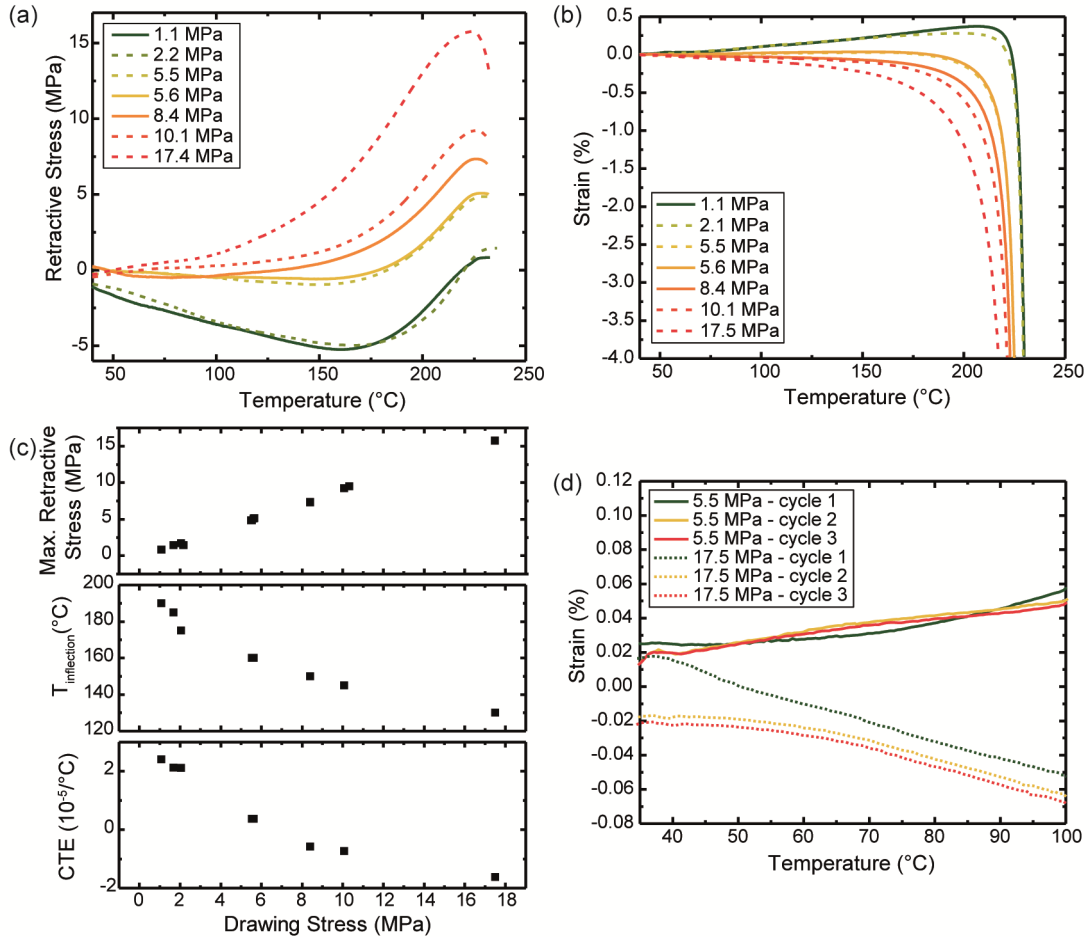
Figure 3-2 (a) Retractive stress measurements of PEI fibers drawn at various stresses and (b) deformation of fibers drawn at various stresses upon heating. Solid lines correspond to fiber drawn at different temperatures and dash lines with different ddr. (c) Maximum retractive stress (fixed extremities), temperature of inflection and longitudinal CTE (without constraint) in function of the drawing stress. (d) Deformation of 2 PEI fibers (5.5 and 17.5 MPa) during three consecutives heating ramp from room temperature to 100 $°C$.

It is also interesting to note that the estimated coefficient of thermal expansion (CTE) below T_g along the fiber direction can be tuned from positive to negative values depending on the drawing stress (Figure 3-2(c)-bottom). Due to the chain structure, the CTE components are different parallel (α_{para}) and perpendicular (α_{perp}) to the polymer chains [116]. Thermal expansion arises from stretching vibrations due to the asymmetry of the binding potentials as well as some transverse vibrations. While α_{perp} is always positive, α_{para} can be negative due to the contribution of the transverse thermal vibrations, which induce a shortening of the chains. From our experiments, it seems that PEI chains exhibit a negative α_{para}, which clarifies the negative CTE at room temperature of highly oriented fibers. Furthermore, some cycling tests up to 100 $°C$ showed the relative stability of the CTE, which confirms that the negative value is not caused by frozen-in stress due to the fast cooling during thermal drawing (Figure 3-2(d)). Tuning the drawing parameters is therefore a simple way to make the CTE of polymers comparable to other classes of materials like metal and therefore improve the dimensional stability of complex devices [121], [122], as we show later.

3.2 SAXS and WAXS analyses

To provide more in-depth information on the effect of drawing stresses on the nanometer and molecular microstructure respectively, we performed SAXS and WAXS measurements on PEI fibers drawn at stresses ranging from 0.8 to 15.5 MPa, as shown in Figure 3-3 and Figure 3-4. At low drawing stresses, isotropic scattering halos in the 2D SAXS profiles are observed caused by the random distribution of lamellar domains (molecular correlations between the nearest molecular neighbors) in the fibers (Figure 3-3(a)). Then, the patterns evolves from isotropic halos to 4-point SAXS patterns on increasing the drawing stress. 4-point patterns have been observed in oriented semi-crystalline polymers and could derive from a tilted lamellar structure or a chevron structure induced by the crystal lamellae [123]–[126]. Even though PEI does not contain crystalline domains, studies revealed the existence of short-range ordered microstructures in amorphous polymers, which could induce such 4-point pattern [127]. The lamellar spacing d in the drawing direction can be deduced from the peak position q_0 in the 1D radial profile (Figure 3-3(b)):

$$d = \frac{2\pi}{q_0} \tag{3.1}$$

The latter is seen to increase first linearly with the drawing stress and starts to stabilize above 10 MPa (Figure 3-3(c)).

Figure 3-3 SAXS characterization of PEI fibers. (a) 2D SAXS profiles measured at a SDD of 27 cm for PEI fibers drawn under stresses between 0.8 and 15.5 MPa. The thermal drawing direction (TD) is shown by an arrow. (b) 1D radial profiles along the fiber direction (30 °) extracted from the 2D profiles as illustrated by the triangle in the first profile. The dashed lines correspond to the Gaussian fit. (c) Lamellar spacing in the drawing direction as a function of the drawing stress.

Similar to SAXS, 2D-WAXS profiles also demonstrate the increase in the anisotropy on increasing the drawing stress of the fibers (Figure 3-4(a)). The presence of the preferred orientation (distinct arcs perpendicular to the fiber drawing direction) in the WAXS patterns indicates the gradual alignment of the polymer chains along the drawing direction. In order to quantify the degree of orientation, the 1D azimuthal profiles have been extracted (Figure 3-4(b)). It is interesting to note that in addition to the increasing intensity at azimuthal angle 90°, a slight increase in intensity at about 45 and 135° azimuthal angle is also observed even at low stress with respect to fiber alignment direction. This

suggests that some 45° chain alignment is present in the fibers and may come from the shear stress experienced by the polymer during thermal drawing and the conical shape in the preform-to-fiber region.
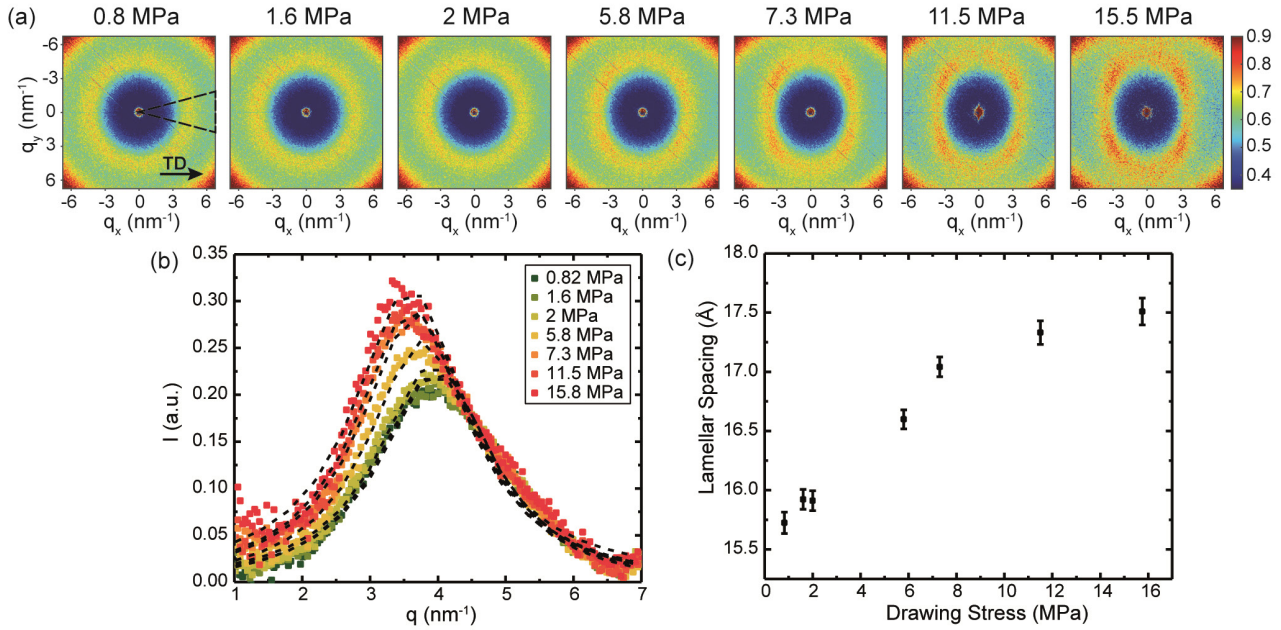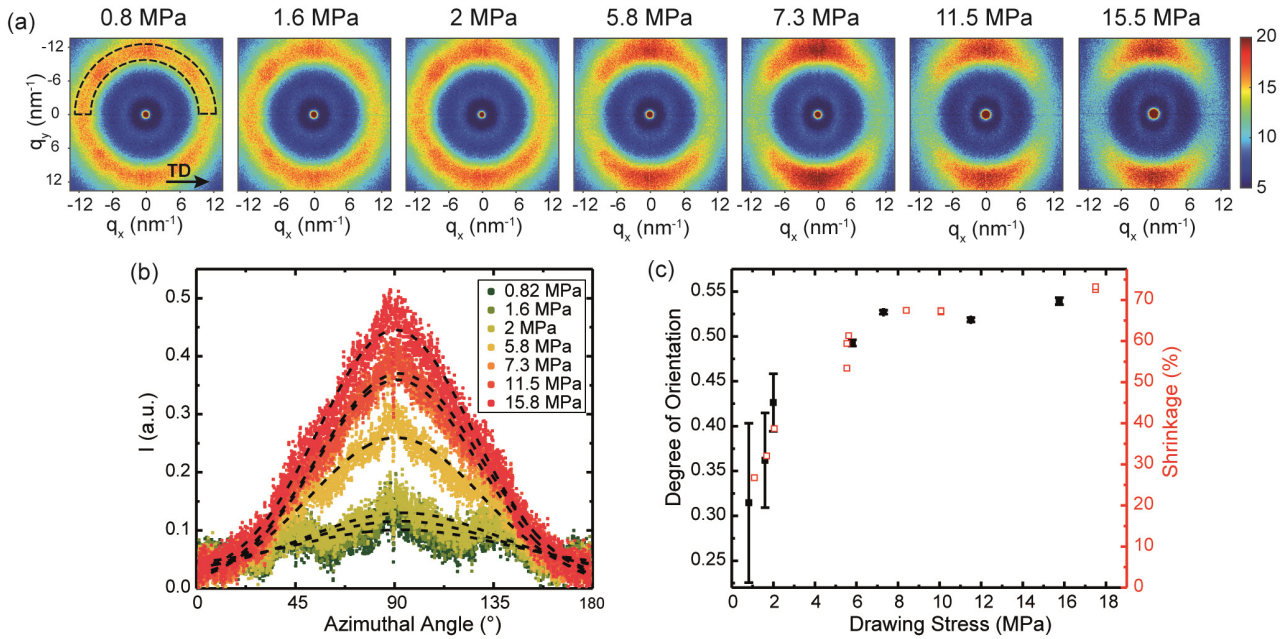

Figure 3-4 WAXS characterization of PEI fibers. (a) 2D WAXS profiles measured at a SDD of 13 cm for PEI fibers drawn under stresses between 0.8 and 18.5 MPa. (b) 1D WAXS azimuthal profiles extracted from the 2D profiles, averaged for (0-180°) and (180-360°) to increase the signal to noise ratio. The dashed lines are Gaussian fits of the data. (c) Degree of orientation (black) in function of the drawing stress. The shrinkage ratio (red) from Figure 3-1(b) is reproduced to enable comparison.

The degree of orientation π can be estimated using Equation 3.2:

$$\pi = \frac{180° - FWHM}{180°}$$

(3.2)

Where $FWHM$ is the full width half maximum and is determined by fitting the azimuthal profile with a Gaussian function, with $\pi = 1$ corresponds to perfect orientation and $\pi = 0$ to completely random orientation [128], [129]. Despite the large standard deviation, the degree of orientation increases linearly with the drawing stress for stresses below 8 MPa, and then reaches a plateau for higher stresses with a maximum of ~0.55. This transition to a nonlinear regime above a critical stress has been reported in polymer melt stretching experiments and has been related to the onset of non-Gaussian stretching when the entangled network reaches its finite extensibility [130], [131]. As shown in Figure 3-4(c), the shrinkage percentage and the changes in the inter- and intramolecular polymer structure show similar dependence on the drawing stress. It reveals that chain orientation is one of the key parameters controlling the thermal shrinkage of thermally drawn fibers. The presence of the plateau further indicates that above 8 MPa, the drawing stress induces internal stresses in the fiber which are not related to chain orientation and could be therefore of enthalpic origin.

3.3 Room temperature mechanical properties

We then turn our focus to the mechanical properties since they are also strongly dependent on the polymer chain alignment and it is an important criterion in applications such as textiles and sutures [5], [43]. As expected, depending on the drawing stress, the tensile stress-strain curves exhibit a wide range of behaviors (Figure 3-5(a)). Fibers drawn under high stress show a glass-like behavior with the stress rising to the breaking point almost linearly with the strain. The rupture occurs at stresses higher than 250 MPa but at low strain compared to the disoriented polymers. On the other hand, fibers drawn at low stress have a rubber-like behavior with the stress increasing at low strain until yielding and sample necking. It reaches then a plateau level where chains start aligning and is followed by a final increase caused by strain hardening until the breaking point at strains as high as 100 %. While the tensile strength seems to increase linearly with the drawing stress, the ductility decreases strongly and reaches a plateau above 8 MPa (Figure 3-5(c)). This trend correlates well with the orientation factor (Figure 3-4(c)) and suggests that the ductility depends on the amount of chains that can still be reoriented and their stretching state [115]. The true stress $-$ strain plot, defined as $\sigma_{true} = \sigma(1 + \varepsilon)$ and $\varepsilon_{true} = ln(1 + \varepsilon)$ with σ and ε being the engineering stress and strain respectively confirms this hypothesis (Figure 3-5(b)). Indeed, all post-yield curves can superpose in a single curve by adding a shift in strain, which indicates that all the fibers obey similar deformation mechanisms [117]. The increase of the Young Modulus from 0.5 to 2.5 MPa with the drawing stress is also attributed to the chain alignment and pre stretching (Figure 3-5(c)). Indeed, in oriented fibers, the deformation acts on the strong covalent bonds aligned to the testing direction, instead of the weaker intermolecular and Van der Waals forces [118]. Interestingly, the mechanical behavior is determined by the drawing stress, which can be easily tuned by varying the temperature during the processing, and no size effect is observed. We can therefore process fibers with a wide range of dimensions with specific mechanical properties.
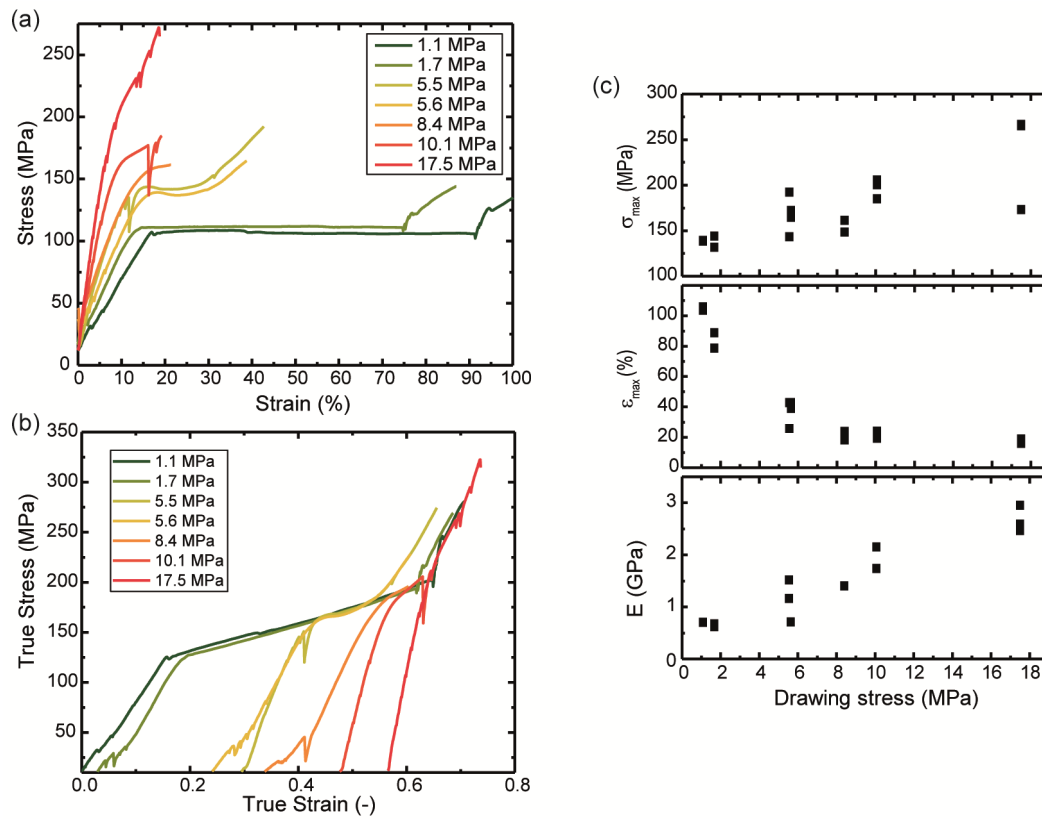
Figure 3-5 Mechanical properties of drawn PEI fibers. (a) Stress-strain curves of PEI fibers drawn at stresses between 1.1 and 17.5 MPa. (b) True stress versus true strain plot of the same fibers. (c) Extracted dependence of ultimate tensile strength σ_{max}, maximum elongation ε_{max} and Young's Modulus E on the drawing stress

3.4 Multimaterial fibers

Since thermal drawing enables the production of fibers composed of several materials in complex architectures, we first verify if our main conclusions for PEI can be extended to other thermoplastics and then we exploit our in-depth understanding to develop heat-controlled bendable fibers. Fibers made of two PMMA with different MW were drawn and analyzed in a DMA following the same procedures as described earlier. The same correlation between the maximum retractive stress and drawing stress is obtained independently of the polymer type (Figure 3-6(a)). This highlights the major influence of the processing stress on the final fiber morphology. Likewise, the free shrinkage shows similar dependence with drawing stress as observed for PEI fibers (Figure 3-6(b)). However, the temperatures at which shrinkage occurs depend on the polymer type and molecular weight. As can be seen in Figure 3-6(b), the low MW PMMA fibers start shrinking at slightly lower temperature even though they were drawn at similar drawing stress than the high MW ones. Indeed, low MW polymers have lower T_g and viscosity due to the reduction in chain entanglement and increased free volume which facilitate molecular slipping [132], [133]. Therefore, a higher chain mobility can be assumed at low temperature. WAXS patterns of three high MW PMMA fibers drawn at various stresses are shown in Figure 3-6(c). Similar to PEI, an asymmetric pattern develops upon drawing at high stress. The 1D azimuthal profiles exhibit comparable features as PEI fibers and the degree of orientation reaches a maximum of ~0.42 at a drawing stress of 16.4 MPa (Figure 3-6(d)). This value is lower than for the PEI and demonstrates the influence of the polymer chemistry on

the chain alignment dependence. Additionally, no intensity was observed in SAXS range for PMMA fibers which indicates an absence of correlation between the lamellae domains of this polymer.
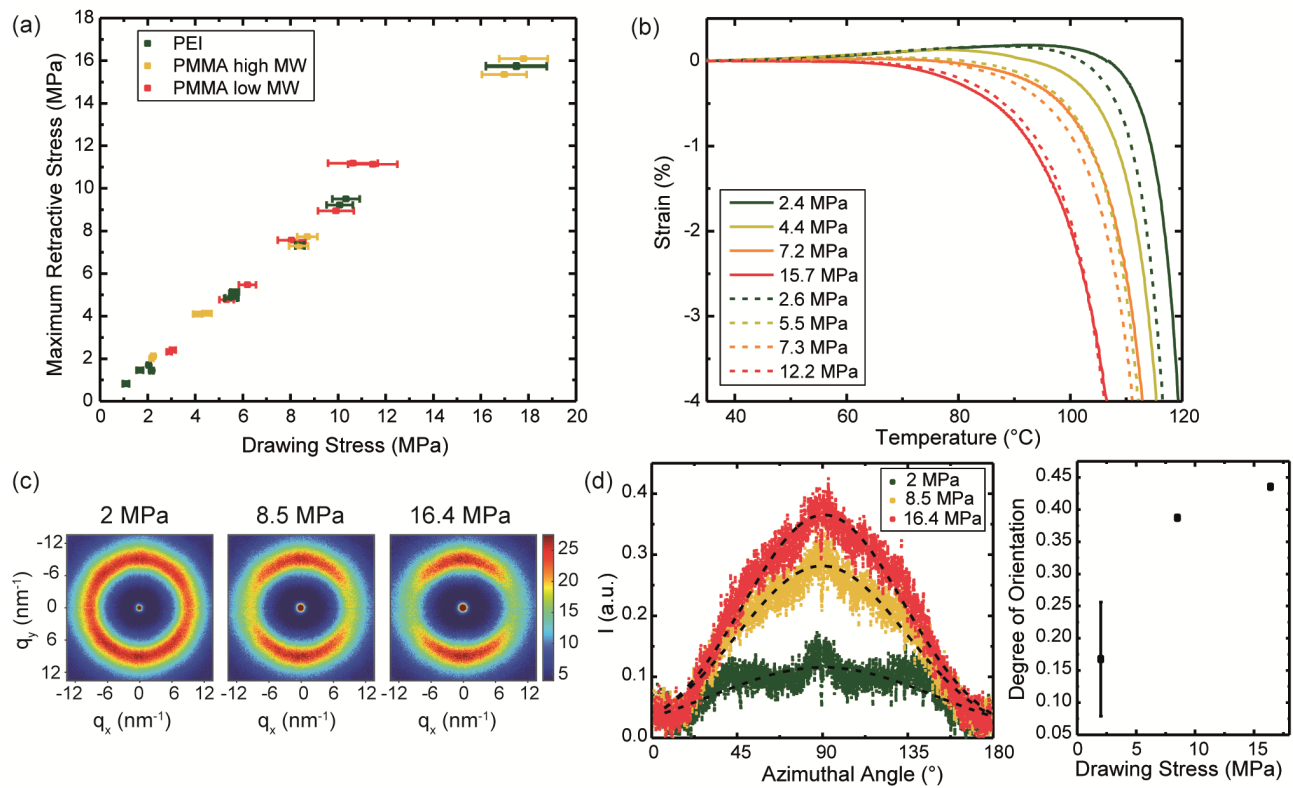
Figure 3-6 (a) Maximum retractive stress versus drawing stress for the different polymers. (b) Temperature dependent shrinkage for the two PMMA fibers drawn at various stresses. The continuous lines correspond to the high MW PMMA and the dash lines to the low MW PMMA. (c) 2D WAXS patterns of three high MW PMMA fibers. (d) 1D extracted radial profiles of the high MW PMMA fibers and calculated degree of orientation.

Overall, these results indicate that the polymer morphology induced during drawing predominantly depend on the processing conditions, in particular the drawing stress, for all polymers. Very low MW polymers could show a different behavior under annealing due to their very weak chain networking which allows the chain to individually retract [120]. However, such polymers are typically not favored in multi-material thermal drawing due to too low viscosity that leads to unstable processing conditions.
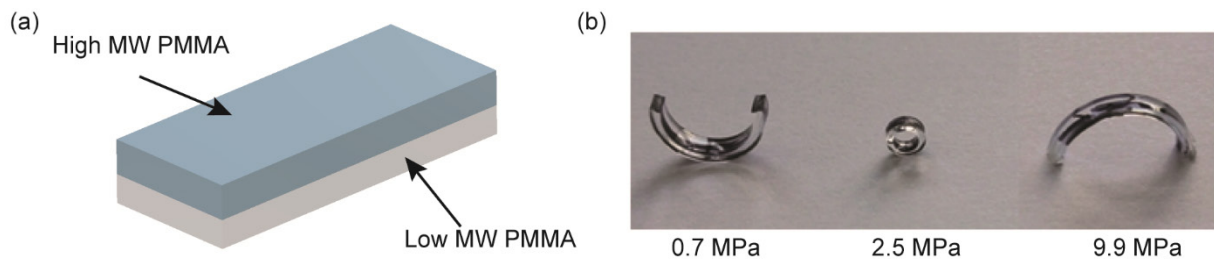
Figure 3-7 (a) Schematic of the preform of the PMMA bending fiber. (b) Photograph of fibers processed at different drawing stresses after annealing with the high MW PMMA at the top

With the ability to control the microstructure and resulting thermal properties of different thermally drawn materials, we can design novel effects and performance for multi-material fibers. We present a first example of a heat-controlled bendable fiber that can be directly produced by co-drawing two plates of different polymers (Figure 3-7(a)). Here, we used the two PMMAs analyzed before, which have similar thermomechanical properties, to demonstrate the dependence of the bending direction on the drawing parameters. The fiber was drawn at various set temperatures (between 270 °C and 210 °C) with a ddr of 10 or 15 and then subjected to annealing. By tuning the stress during drawing, we can engineer different bending behaviors upon annealing. Indeed, as shown in Figure 3-7(b), after heating the fibers for one hour at 100 °C, opposite bending behaviors were observed. For fibers drawn at high stress, the low MW PMMA part shrank first, while for the others bending occurred due to the shrinkage of the high MW PMMA part. To understand this transition, the stress experienced by both polymers during thermal drawing was estimated by measuring their temperature dependent viscosity and assuming a stress proportional to the viscosity at a fixed deformation rate (see section 1.1.3). As we can see in Table 3.2, in all the fibers the high MW PMMA carried the highest stress, between 2 to 4 times higher, due to its higher viscosity during the draw. Since at low stress, the shrinkage temperature is very sensitive to the drawing stress, this difference is sufficient to promote the shrinkage of the high MW PMMA part. On the other hand, at high stress, even though each part supported respectively 6.1 and 13 MPa, the difference in chain alignment is smaller and the low MW part shrinks first due to its higher chain mobility at the annealing temperature.

Table 3.2 Stress distribution in the PMMA fiber

Fiber	Low MW PMMA	High MW PMMA
(MPa)	(MPa)	(MPa)
0.7	0.3	1.1
2.5	0.9	3.8
9.9	6.1	13.0

3.5 Strategy to reduce the shrinkage

Finally, while significant chain alignment improves the mechanical properties and enables the tuning of the CTE and controlled shrinkage, some applications or post-processing steps require stable dimensions independent of the temperature. Based on our deeper understanding, we propose a relaxation procedure consisting in annealing the fibers while fixing the fiber extremities to prevent shrinkage. Figure 3-8 shows the retractive stress measured after successive heat treatments of a PEI fiber drawn under a stress of 17 MPa. Although a heat treatment below the T_g can delay the shrinkage to higher temperatures, the maximum retractive stress is only marginally reduced. A second heat treatment above T_g is thus necessary to allow a larger relaxation.
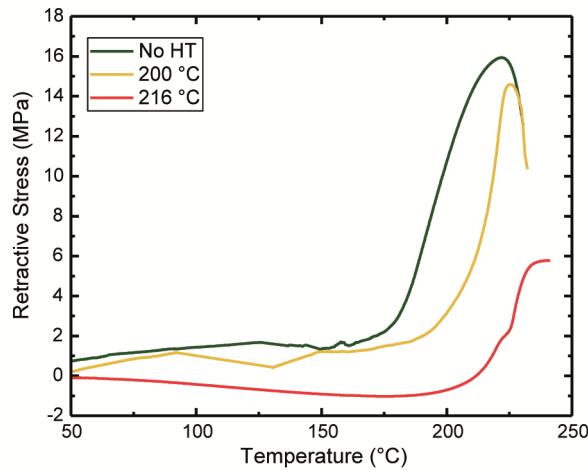
Figure 3-8 Retractive stress measurements of PEI fibers drawn with a ddr of 40 after no annealing, 2 hour annealing at 200 $°C$, additional 2 hour annealing at 216 $°C$ respectively.

This relaxation goes along with a reduction of the lamellar spacing in the drawing direction (Figure 3-9(a)) and of the polymer chair alignment as revealed by the decrease in anisotropy of the 2D WAXS profiles (Figure 3-9(b)). After the heat treatment at 200 °C, the degree of orientation does almost not decrease which explains the similar retractive stress measured. After the annealing at 216 °C, the degree of orientation is reduced from 0.55 to 0.5 (Figure 3-9(b)) and, as demonstrated earlier, this reduction is sufficient to induce a large decrease in retractive stress due to the strong dependence at high stresses. It is important to note that a temperature-step heat treatment is required. A direct heating above T$_g$ can lead to a mechanical failure of the fiber because of the combined high retractive stress and high chain mobility. This first heat treatment procedure paves the way towards the engineering of more complex procedures that could lead to optimized relaxation in fiber devices.

Figure 3-9 (a) SAXS and (b) WAXS characterization of PEI fibers before and after annealing with 1D profiles and calculated lamellar spacing and degree of orientation, respectively.

We then applied this treatment to a PEI fiber containing a thin $Pt_{57.5}Cu_{14.7}Ni_{5.3}P_{22.5}$ metallic glass ribbo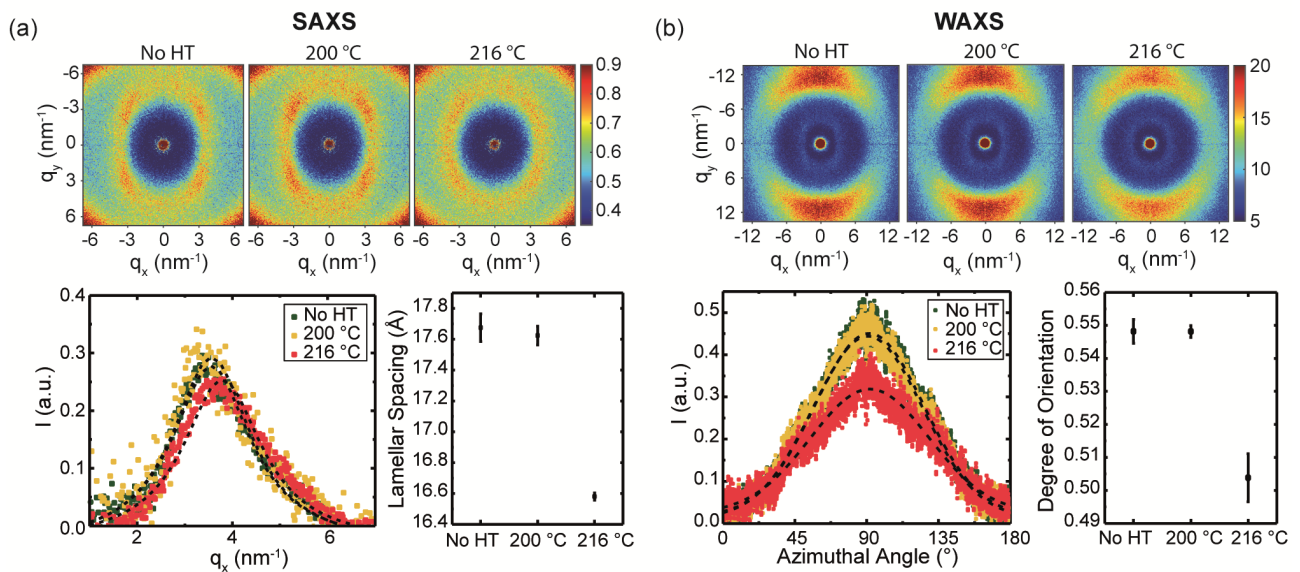n serving as an electrode drawn under a stress of 10.1 MPa [134]. Such fiber can be used as a classical resistive metal-based temperature sensor since the resistance will vary both due to the temperature dependent resistivity of the metal and the thermal expansion of the fiber [135]. These types of fibers can be integrated within garments and alert workers of excessive heat at the proximity of the skin, for example. Such high-temperature applications however requires a large temperature window of operation. We measured the relative resistance change due to a localized heating on two fibers of similar dimension before and after annealing at the maximum temperature of 210 $°C$. The fiber and experimental set-up are schematized in Figure 3-10(a) and the results presented in Figure 3-10(b). While the as-drawn fiber loses its linearity above 140 $°C$ due to the irreversible fiber shrinkage, the linearity is preserved up to nearly 200 $°C$ for the heat treated one. This experiment illustrates how an annealing procedure based on the developed in-depth understating of process-microstructure relationship in the thermal drawing process, can extend the operating temperature range of a fiber sensor by 40 %.
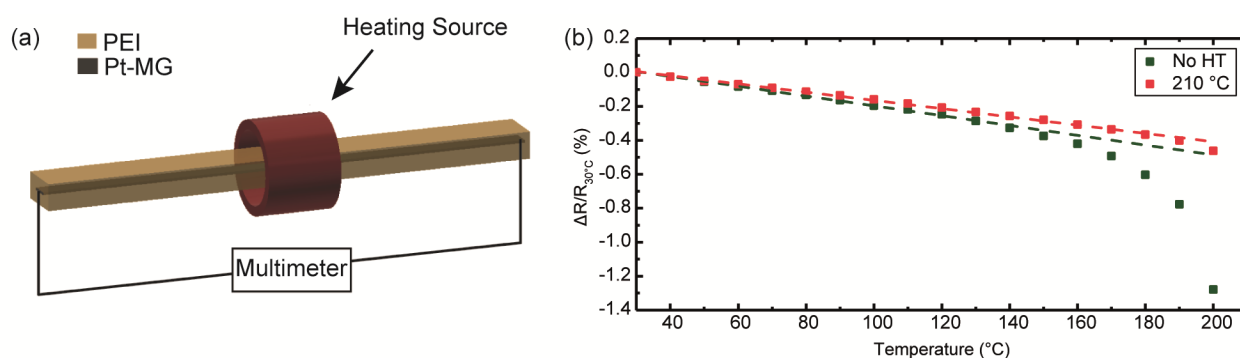

Figure 3-10 (a) Schematic of the temperature sensing fiber and experimental set-up. (b) Relative resistance change versus temperature for the temperature sensing fiber after no annealing and an annealing at a maximum temperature of 210 $°C$.

3.6 Summary and conclusion

In this chapter, we revealed the dependence of the thermal shrinkage behavior on the processing stress during thermal drawing. In particular, we found that the retractive stress contained in the drawn fibers was proportional to the processing stress and that the latter also controlled the temperature dependent deformation. We then carried out morphological characterization through SAXS and WAXS experiments and correlated the shrinkage behavior to the variation in the degree of polymer chain orientation. Our research also showed the influence of the drawing parameters on the mechanical properties with a transition from weak but ductile fibers to strong but brittle fibers with increasing stress. Moreover, we generalized these findings by following a similar approach to study fibers made of two grades of PMMA with different molecular weight. We observed that the molecular weight has an impact on the temperature at which shrinkage takes place and therefore were able to design a bending fiber by co-drawing the two types of PMMAs. Finally, we proposed a thermal annealing strategy to reduce the amount of internal stress and the degree of polymer orientation in order to postpone the shrinkage to higher temperatures. This procedure allowed us to extend by 50 $°C$ the operating range of a temperature sensor based on a metallic glass electrode. We envision that the deeper understanding revealed by this work can serve as a guidance for the processing of complex multimaterial fibers with finely tuned properties.

3.7 Materials and experimental methods

Materials: .25'' thick plates of polyetherimide (PEI, ULTEM 1000) and poly(methyl methacrylate) (PMMA) were purchased from Boedeker and Evonik Röhm GmbH, respectively. A PMMA powder (average MW ~120,000 by GPC, 182230) was obtained from Sigma Aldrich. The $Pt_{57.5}Cu_{14.7}Ni_{5.3}P_{22.5}$ alloy was purchased at PXGroup (Switzerland) and the ribbons were prepared by melt spinning on a Cu wheel with a rim speed of 20 $m\,s^{-1}$.

Preform fabrication and thermal drawing: Flat rectangular preforms (24 x 6.4 x 150 mm^3) were cut from the commercially acquired polymer plates. The low MW PMMA powder was consolidated in a mold in a hot press at 210 °C for 20 min to obtain plates of similar dimensions (Lauffer Pressen UVL 5.0). The preform for the PMMA bending fiber was processed by consolidating a low MW PMMA powder plate and high MW PMMA in a mold at 135 °C for 15 min. The heat sensor preform was obtained by encapsulating a Pt-MG ribbon between two plates of PEI and consolidating it at 240 °C for 30 min (Maschinenfabrik Herbert Meyer GmbH).

The preforms were thermally drawn into fibers in a three-stage vertical oven. In order to obtain a wide range of drawing stresses, two PEI fibers were drawn at a ddr of 15 and various set temperature between 360-320 °C. Additionally, a PEI fiber was drawn at a fixed set temperature of 350 °C and ddr between 10 and 40, a high MW PMMA fiber at 255 °C with ddr between 10 and 30, and a low MW PMMA fiber at 235 °C with ddr between 10 and 25. The bending fiber was drawn at 270 °C under a ddr of 10 and 15, and at 250 °C under a draw down ratio of 15. The temperature sensing fiber was drawn at 340 °C with a ddr of 26.5. Few meters were drawn after each variation of the drawing parameters before collecting the samples to ensure stable conditions.

The tension was measured by a tension meter composed of three rollers. The drawing stress is then calculated by:

$$\sigma_{draw} = \frac{Force}{Surface} = \frac{T \times g}{w \times t}$$

With T the tension, g the gravity constant, w the width and t the thickness of the fiber.

Free shrinkage study: 5 mm long fibers were heated up to 225 °C (T$_g$ + 11 °C) in a dilatometer with a temperature ramp of 3 °$C\,min^{-1}$ and annealed for 10 min at this temperature. Their decrease in length was measured and the shrinkage ratio was estimated by $(\%) = \frac{L_0 - L_1}{L_0} \times 100$, with L_0 the initial length and L_1 the length after annealing. The width and thickness of each sample was also measured before and after the annealing.

Thermo-mechanical characterization: A DMA (Q800, TA Instruments) operating in film tension mode was used to characterize the shrinkage behavior of the samples. A low tensile force of 0.001 N was applied on the samples to prevent sample slippage. The samples were heated from room temperature up to their T$_g$ + 20 °C with a heating ramp of 3 °$C\,min^{-1}$ and the strain was continuously recorded. The sample length was kept as similar as possible. The CTE was estimated with the slope of the strain versus temperature curve between 30 and 60 °C. The retractive stresses were measured by fixing the extremities and increasing the temperature with a heating ramp of 3 °$C\,min^{-1}$.

Mechanical tensile testing: Tensile tests were performed with an electromechanical Universal Testing Machine Series LFM-125 kN using a 1 kN load cell. The initial sample length was 10 cm and the strain rate 1 $mm\ s^{-1}$.

SAXS and WAXS characterization: SAXS and WAXS experiments were performed with a Bruker Nanostar instrument (Bruker AXS GmBH, Karlsruhe, Germany) equipped with a pinhole collimation system and a micro-focused X-ray Cu source (wavelength CuKα 1.5406 Å) providing a beam diameter of about 400 μm. A 2D MikroGap technology-based detector (VANTEC-2000) with 2048 x 2048 pixels (pixel size 68 x 68 μm) gave a resolvable scattering vector modulus q-range between 0.06 and 26 nm^{-1} for a combination of sample-to-detector distance (SDD). Samples were measured at a SDD of 13 cm and 28.5 cm with resolvable q-range of 0.95-15.6 and 0.27-8.88 nm^{-1} respectively. 2D profiles and fittings were performed in MatLab and Python. 1D profiles were extracted using the Bruker software DIFFRAC.EVA. Radial profiles along the fiber directions were extracted by performing a wedge integration (30°). The background was subtracted after normalizing the total scattering profile by the transmitted intensity measured at the direct beam position. Peak position was determined by subtracting the baseline line and fitting the extracted peak with a Lorentzian function. The azimuthal scans were obtained by performing radial integration in the q-range of 10.65-12.77 nm^{-1} and 8.53-10.64 nm^{-1} for 360° azimuthal angle for PEI and PMMA fibers respectively. The profiles were then normalized to the total scattering intensity and averaged over (0-180°) and (180-360°) to improve the statistics. A Gaussian fit was performed to determine the FWHM of the peaks. The error bars correspond to half of the 95 % confidence interval of the fitting parameters.

Heat treatments: The drawn fibers were clamped at both end to prevent any shrinkage and stored in an oven. The multistep heat treatments were carried out by gradually increasing the temperature from below to above T_g. At each temperature, a 2 hour annealing was performed.

4 Thermal drawing of bulk metallic glasses

In order to address the limitation in feature size of conductive electrodes, we propose here to replace crystalline metals and conductive composites by metallic glasses. Indeed, metallic glasses satisfy all the requirements: they can be processed at a high viscosity state in the SCLR; sub-micrometer features have been reported by thermoforming [49]; and they have high conductivity, around one order of magnitude lower than crystalline metals, due to their disordered structure. Their high viscosity state during processing also allows us to design more complex fiber architectures and to interface them with materials in their molten state during the draw. In addition, these MGs have exceptional strength, elasticity and good corrosion resistance that offer opportunities in flexible electronics or neuroscience. The thermal drawing technique can also serve as a platform to perform fundamental research on the crystallization kinetics both at the micro- and nanoscale. Indeed, several processing parameters such as deformation, deformation rate or size have been reported to have an influence on the kinetics.

This chapter starts with the identification of two BMGs which can be drawn inside polymer matrices: $Pt_{57.5}Cu_{14.7}Ni_{5.3}P_{22.5}$ (Pt-MG) and $Au_{49}Ag_{5.5}Pd_{2.3}Cu_{26.9}Si_{16.3}$ (Au-MG). We first focus on the Pt-MG and demonstrate the ability to draw ribbons spanning a wide size range from a few micrometers to around $40\ nm$ and rods down to sub-micrometer diameters. We then show the versatility of fiber structures enabled by the preform design at the macroscopic scale. Next, we discuss the influence of capillary instabilities and crystallization on the ribbon break-up, which control the ultimate feature size. We then present an analysis of the influence of thermal drawing on the crystallization kinetics at the nanoscale, via in situ heating TEM, and at the microscale via DSC, XRD and SEM morphological observation. Finally, we turn to the Au-MG having a lower GFA. We first describe the strategies used to find a polymer cladding with compatible thermo-mechanical properties. The ultimate feature size and the crystallization kinetics are then investigated.

The first part of the research on the Pt-MG was performed in collaboration with Dr. Wei Yan and the results have been published in:

W. Yan, I. Richard, G. Kurtuldu, N.D. James, G. Schiavone, J.W. Squair, T. Nguyen-Dang, T. Das Gupta, Y. Qu, J.D. Cao, R. Ignatans, S.P. Lacour, V. Tileli, G. Courtine, J.F. Löffler, and F. Sorin "Structured nanoscale metallic glass fibres with extreme aspect ratios", *Nat. Nanotechnol*. 15, p. 875-882, August 2020, doi : 10.1038/s41565-020-0747-9

4.1 Material selection

4.1.1 BMG selection criteria

As reported in section 1.1.2; selection criteria have been developed to identify co-drawable pairs of materials. They include requirements on specific thermal, rheological and crystallization properties. These criteria can be extended to the thermal drawing of bulk metallic glasses. To be drawable, the BMG should have sluggish crystallization kinetics in the supercooled liquid region while reaching a low viscosity. Furthermore, they need to have a compatible processing temperature with an amorphous polymer to serve as a cladding. To identify possible pairs of BMG-polymer we conducted an extensive literature review and defined three requirements:

1. $t_{x,\ BMG}(T_{max}) \geq 10\ min$
2. $T_g(clad) \approx T_g(BMG)$
3. $\eta_{BMG}(T_{max}) \approx 10^7\ Pa\ s$

With T_{max} the maximum temperature of the temperature profile inside the drawing oven and t_x the crystallization time.

The first requirement means a high resistance to crystallization at the processing temperature. Since TTT diagrams are not reported for all the BMGs, we relied on the temperature range of the SCLR ($\Delta T_x = T_x - T_g$) or the maximum casting diameter to select possible candidates. Furthermore, during this thesis, we focused on amorphous polymer claddings with a maximum T_g of 215 $°C$ (polyetherimide). Therefore, the second criteria reduces already significantly the compatible families of BMGs. For example, it excludes the good glass formers Zr-BMGs and Pd-BMGs which could potentially be drawn in glass claddings. Precise measurements of the temperature dependent viscosity being not always available for all the BMGs, we then searched for BMG exhibiting a fragile behavior. Since a fragile behavior often correlates with faster crystallization kinetics due to the higher mobility, thermodynamically stabilized BMGs are preferred. Based on this review, two BMGs were selected to be investigated in this thesis: Pt$_{57.5}$Cu$_{14.7}$Ni$_{5.3}$P$_{22.5}$ and Au$_{49}$Ag$_{5.5}$Pd$_{2.3}$Cu$_{26.9}$Si$_{16.3}$.

The Pt$_{57.5}$Cu$_{14.7}$Ni$_{5.3}$P$_{22.5}$ BMG was developed in 2004 by Schroers and Johnson [136]. It has a Tg of 235 $°C$, a SCLR of 98 $°C$ and shows excellent processability. In addition, they observed no embrittlement and a good resistance to oxidation when heated in the SCLR in contrast to other BMGs such as Zr-based alloys. Its high glass forming ability comes from a surprising combination of slow crystallization kinetics and fragile kinetic behavior ($m = 51.9$ [137]) as reported by Pitt et al. [44] (Figure 4-1). Legg et al. [138] reported than neither the thermodynamics nor the kinetics properties could induce this outstanding glass forming ability. They measured a steeper temperature dependent Gibbs free energy difference between the liquid and crystal phases compared to other BMGs and a higher temperature dependence of the viscosity. Since both phenomena should enhance the crystallization kinetics, they suggested that the nucleation rate is controlled by the high liquid-crystal interfacial energy. Gross et al. [57] reported a similar high interfacial energy of 0.11 Jm^{-2} for a good glass former of the same system Pt$_{42.4}$Cu$_{27}$Ni$_{9.5}$P$_{21}$.
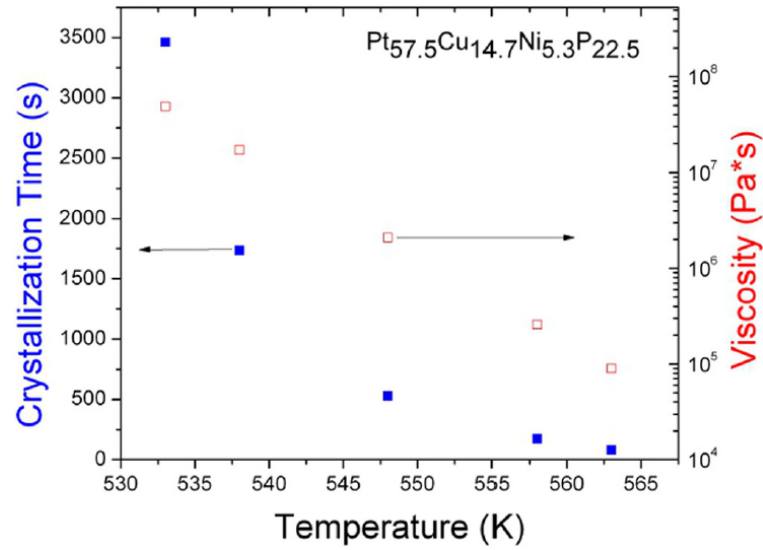
Figure 4-1 Temperature dependent crystallization time and viscosity of Pt57.5Cu14.7Ni5.3P22.5 [44]

The Au49Ag5.5Pd2.3Cu26.9Si16.3, developed by Schroers et al. in 2005, is characterized by a lower Tg of 128 °C, a SCLR of 58 °C and a critical casting thickness exceeding 5 mm [139]. It shows a less fragile behavior compared to the Pt-MG with $m = 16$ [137] and can reach viscosity down to $2 \times 10^7 \, Pa \, s$ in the SCLR [140]. Furthermore, the TTT diagram reveals relatively slow crystallization kinetics below 155 °C as shown in Figure 4-2(a) [141]. Interestingly, the crystallization process depends on the heating rate or annealing temperature. At annealing temperature around 150 °C or below, a rather soft phase nucleates attributed to Au-Cu rich compositions, in opposition to the harder phase nucleating at higher temperature [142], [143]. Thermomechanical tests further highlighted the ability of the Au-MG to be thermoformed even after the crystallization onset (Figure 4-2(b)) [144], meaning a longer processing time available.
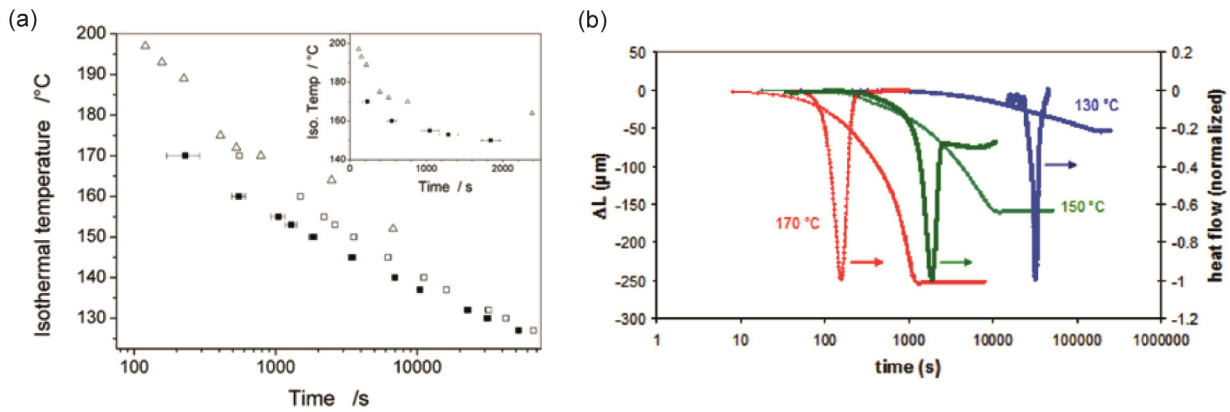
Figure 4-2 (a) TTT diagram of Au49Ag5.5Pd2.3Cu26.9Si16.3 [141]. (b) Comparison between the deformation and heat flow during isothermal holding at 130, 150 and 170 °C [144].

4.1.2 Cladding selection

The next step consisted in finding cladding materials which could be co-drawn with these two BMGs. We compared the temperature dependent viscosity of the BMGs reported by Pitt et al. [44] and of amorphous polymers previously

characterized by shear rheology in our laboratory (Figure 4-3). It enabled us to identify two pairs of materials having similar viscosity in a temperature range:

1) Polyetherimide and $Pt_{57.5}Cu_{14.7}Ni_{5.3}P_{22.5}$

2) Poly(methyl metacrylate) and $Au_{49}Ag_{5.5}Pd_{2.3}Cu_{26.9}Si_{16.3}$

The thermal drawing of these pairs of materials is presented in the rest of this chapter.
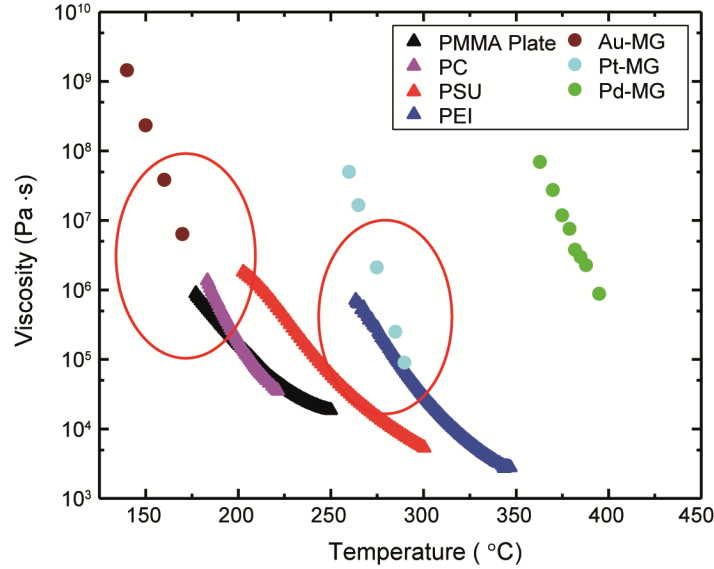
Figure 4-3 Temperature dependent viscosity of several BMGs (from [44]) and thermoplastic polymers.

4.2 Thermal drawing of Pt-BMG and polyetherimide

4.2.1 Thermal drawing

In order to verify the data from the literature and from the manufacturer, we first performed DSC analyses on the cast Pt-MG and PEI plates. Their heating curves at a rate of $20\ °C\ min^{-1}$ are presented in Figure 4-4(a) and demonstrate the onset of glass transition (T_g) and of crystallization (T_x) temperatures. Furthermore, we also constructed the low temperature part of the TTT diagram for $Pt_{57.5}Cu_{14.7}Ni_{5.3}P_{22.5}$ (Figure 4-4(b)). The temperature of the specimens was quickly increased from room temperature to isothermal treatment temperatures in the supercooled liquid region (250, 260, 270, 280 and 290 $°C$) and held there until they were fully crystallized. The time required for 5% and 95% crystal phase fractions were determined for each isothermal temperature using the total enthalpy of crystallization. Five measurements were done for each temperature. Both measurements confirm the large supercooled liquid region ($\Delta T = 83\ °C$) of the Pt-MG, the compatible softening temperatures of the polymer and the metal and the long crystallization time above T_g.
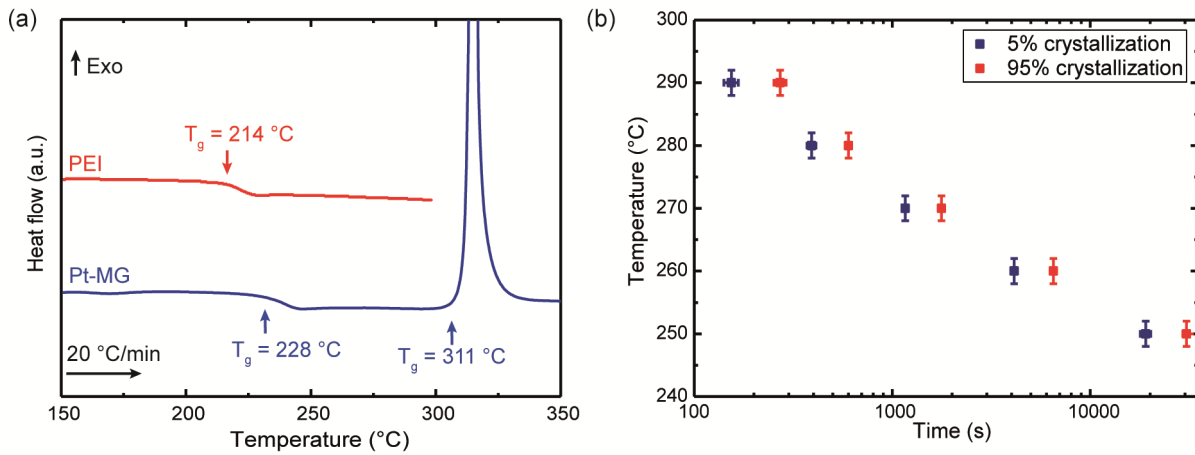
Figure 4-4 DSC characterization: (a) DSC heating curves of PEI and $Pt_{57.5}Cu_{14.7}Ni_{5.3}P_{22.5}$ at a rate of 20 $°C\ min^{-1}$. (b) TTT diagram of $Pt_{57.5}Cu_{14.7}Ni_{5.3}P_{22.5}$. The horizontal error bars show the standard deviations of measured time for 5 and 95 % crystallization fractions and vertical errors bars the $\pm 2\ °C$ accuracy of DSC measurements.

To demonstrate the co-processing of metallic glasses and thermoplastic polymers, the Pt-MG ribbons were inserted between two PEI plates and the assembly was consolidated in a hot press at 240 $°C$ for 30 min with a low pressure to form the first preforms. The latter were then successfully drawn and fibers containing MGs ribbons of various thicknesses uniform along tens of meters were produced. Draw down ratios up to 30 can be achieved by increasing the drawing speed and slightly adjusting the drawing temperature to control the stress supported by the polymer cladding. Beginning for example with a 60 μm thick MG ribbon, 2 μm thicknesses can be reached with a single draw.

In order to further reduce the ribbon thicknesses, an iterative drawing method can be used as schematized in Figure 4-5(a). After drawing a first fiber, a section of this fiber can be cut and encapsulated in another PEI jacket. After consolidation, the preform can be redrawn and the ribbon thickness reduced to a few hundreds of nanometers, depending on the draw-down ratio. The drawing step can be repeated a third time to achieve ribbons with thicknesses of a few tens of nanometers. Figure 4-5(b) shows some SEM cross-sections of the drawn fibers after the various steps. We can see that the MG ribbon thickness is uniform and can reach down to~$40\ nm$. Furthermore, once thermally drawn, the MG ribbons can be extracted from the polymer matrix via mechanical peel-off of the PEI cladding or by selectively dissolving the PEI with N-Methyl-2-Pyrrolidone (NMP). Some example of free-standing micro- and nanoribbons are shown in Figure 4-5(c) with thicknesses ranging from 2.5 μm to 50 nm. In contrast to crystalline metals, the MG ribbons remain continuous and unaltered along the fiber axis even with sub-1 μm thicknesses.
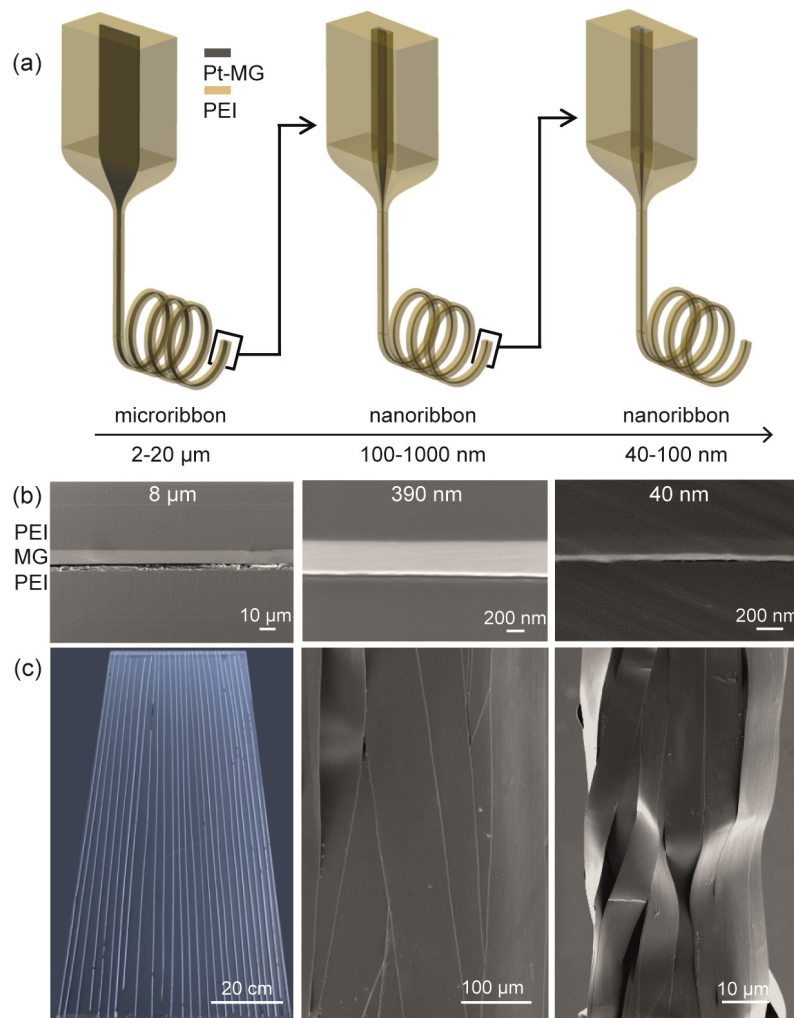
Figure 4-5 Processing of highly uniform and well-ordered micro- and nanoscale Pt-MG ribbons via thermal drawing: (a) Schematic of the fabrication scheme. (b) SEM micrographs (cross-sectional view) of Pt-MG ribbons with thicknesses of $\sim 8\ \mu m$, $390\ nm$ and $40\ nm$. (c) Left: optical image of meters-long MG ribbons with a thickness of around 2.5 μm, Middle: SEM micrograph of ribbons of $\sim 500\ nm$ thickness, Right: SEM micrograph of ribbons of $\sim 50\ nm$ thicknesses.

The capability of reaching sub-100 nm feature sizes of highly conductive material is achievable thanks to two main factors. First, the Pt-MG ribbons are drawn in a highly viscous state which impedes the development of capillary instabilities and therefore the ribbons conserve their integrity during the draw (see section 4.2.3). Furthermore, iterative drawing can be repeated only provided that the metallic glass remains mostly amorphous. To assess the latter, we carried out TEM analyses on the Pt-MG ribbons after each step. The selected-area electron diffraction (SAED) patterns are shown in Figure 4-6. All the samples exhibit the broad halos characteristics for the amorphous state. This highlights again the excellent stability against crystallization of the $Pt_{57.5}Cu_{14.7}Ni_{5.3}P_{22.5}$ alloy. Nevertheless, the presence of nanocrystals cannot be ruled out since their signal could be hidden by the amorphous matrix. A more exhaustive study on the crystallization behavior is presented in sections 4.2.4 and 4.2.5.
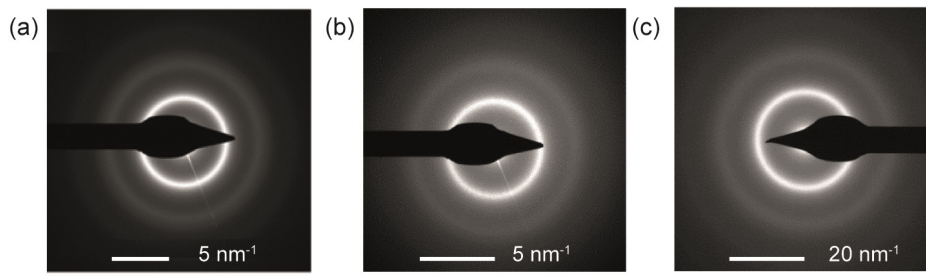
Figure 4-6 SAED patterns of the Pt-MG ribbon drawn once (thickness: 2.5 μm), twice (thickness: 500 nm) and three times (thickness: 50 nm).

A similar iterative procedure can be used to draw Pt-MG rods. Starting with a 1-mm diameter rod, a 4-um diameter rod can be obtained after 2 draws (Figure 4-7(a)). Reaching sub-um does however often induces a break-up of the rod as shown by the optical micrograph in Figure 4-7(b). The exact reason for this break-up is still a subject of investigation. However, we were able to successfully draw continuous rods with a diameter of 750 nm by completely dissolving the cladding of the 2nd drawn fiber and inserting the Pt-rods in a new preform. An SEM micrograph of these rods after etching the cladding is shown in Figure 4-7(c) and shows that the diameter of the rods remains perfectly constant along the length. This rules out the fluid instabilities as a cause of the break-up in contrast to crystalline metals processed in the molten state. TEM characterization on these rods again reveals that the rods remain mostly amorphous after this third draw as shown by the broad halo in the SAED (Figure 4-7(d)). Some nanocrystals might still be present and not visible due to the relatively large thickness of the sample cut by ultramicrotomie ($\sim 80\ nm$). A possible reason for the break-up is that the stress that the Pt-MG is experiencing during the draw is too high due to the higher viscosity of the Pt-MG and the small cross-section area. It can then induce locally some break-up of the wires which are then simply pulled by the cladding like fillers.
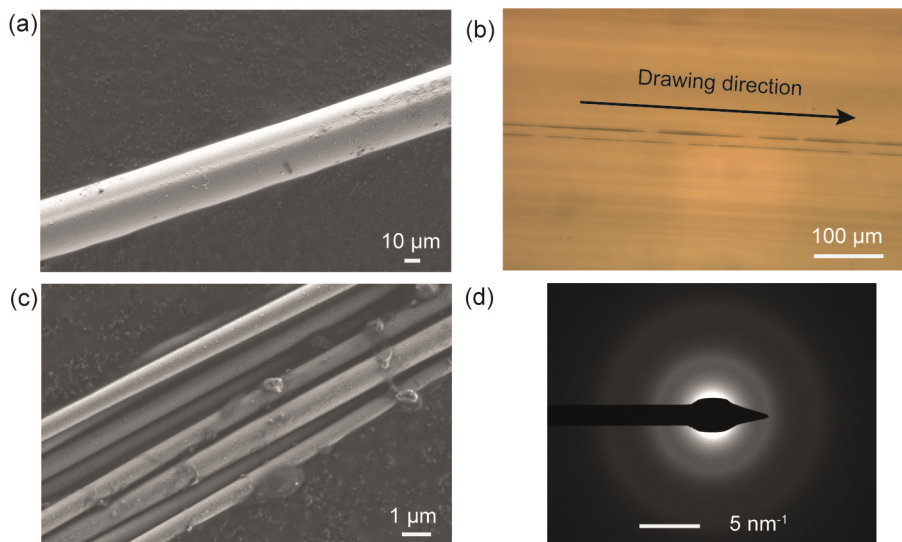
Figure 4-7 Processing of Pt-MG rods: (a) SEM micrograph of twice drawn rod with a diameter of $\sim 4\ \mu m$. (b) Optical micrograph of a third drawn fiber along the drawing direction. (c) SEM micrograph of third drawn rods with diameters of $\sim 750\ nm$. (d) SAED pattern of a third drawn rod.

4.2.2   Composite fibers and Pt-MG properties

The ability to reach feature sizes at the nanometer level opens opportunities for the design of complex MG micro-structures. Various methods can be used to make macroscopic preforms from which structured MG fibers can be fabricated. The first one is referred to as the stack-and-draw approach and consists in simply milling grooves, integrating multiple materials of determined dimensions between two polymer plates and consolidating the assembly. An example of such a preform is shown in Figure 4-8(a) where alternating layers of Pt-MG ribbons and PEI films are inserted between two polymer plates. Secondly, cylindrical preforms can be made by rolling polymer films either around a polymer or a ceramic rod, to end up with a hollow preform, and consolidating the preform in a vacuum oven. Other elements can be inserted during the rolling, such as Pt-MG ribbons, to increase the complexity of the preform as illustrated in Figure 4-8(b). The third method consists in drilling holes in a preform and either leaving the holes empty, inserting raw materials or inserting previously drawn fibers for an iterative draw as shown in Figure 4-8(c). Finally, all these methods can be combined to fabricate complex macroscopic preforms. Furthermore, thanks to the cross-section preservation and direct relationship between the draw down ratio and the size reduction, simple calculations permits us to determine the dimension of each elements at the preform level in order to obtain a fiber with the expected architecture.
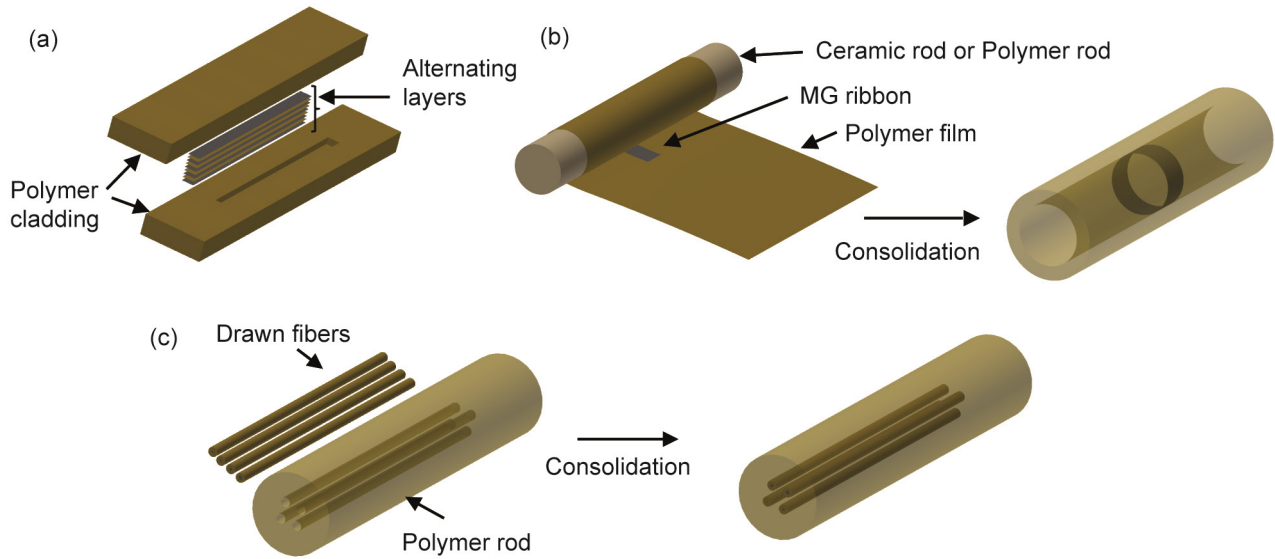
Figure 4-8 Schematics of the preform making: (a) Stack-and-drawn method. (b) Thin film rolling. (c) Holes drilling.

In order to illustrate the ability of the co-processing of BMGs and thermoplastics to reach complex structure with extremely thin feature sizes, we fabricated various multi-material fibers shown in Figure 4-9. The first fiber consists in ten alternating layers of Pt-MG and PEI encapsulated with a PEI cladding, as shown in Figure 4-9(a). The interface between the two materials is smooth and the number and size of such bi-layers can be tuned at the preform level, paving the way towards a scalable fabrication of fiber-based optical metamaterials [145]. Besides embedding nanoscale MG ribbons into a polymer matrix, their high viscosity during thermal drawing allows us to also expose them on the fiber surface. As shown in Figure 4-9(b), a MG array with a periodicity of 4.5 μm runs along the surface over the entire fiber length. This presents a new approach to the fabrication of optical gratings or implantable probes with exposed electrodes [146], [147]. Other examples of architectures can be found in Figure 4-9(c) and (d) with cylindrical fibers

containing a hollow core surrounded by a continuous MG layer or a slotted MG cylinder. The integrity of the ribbons is confirmed by energy dispersive X-ray (EDX) mappings shown in the insets. The former fiber might find application for transmitting high-power light at long wavelengths and the latter might be used as a magnetic resonator [148]. By combining various polymers having compatible thermoplastic properties and MG components a more advanced structure can be designed as shown in Figure 4-9(e). The fiber consists in a PEI/polyethersulfone waveguide surrounded by three MG ribbons (thicknesses of 2.5 μm, 400 nm and 53 nm) and two MG rods (diameters of 26 μm) encapsulated in a PEI cladding. Such multi-functional fibers could be used for simultaneous optical and electrical stimulation and recording for example [9].
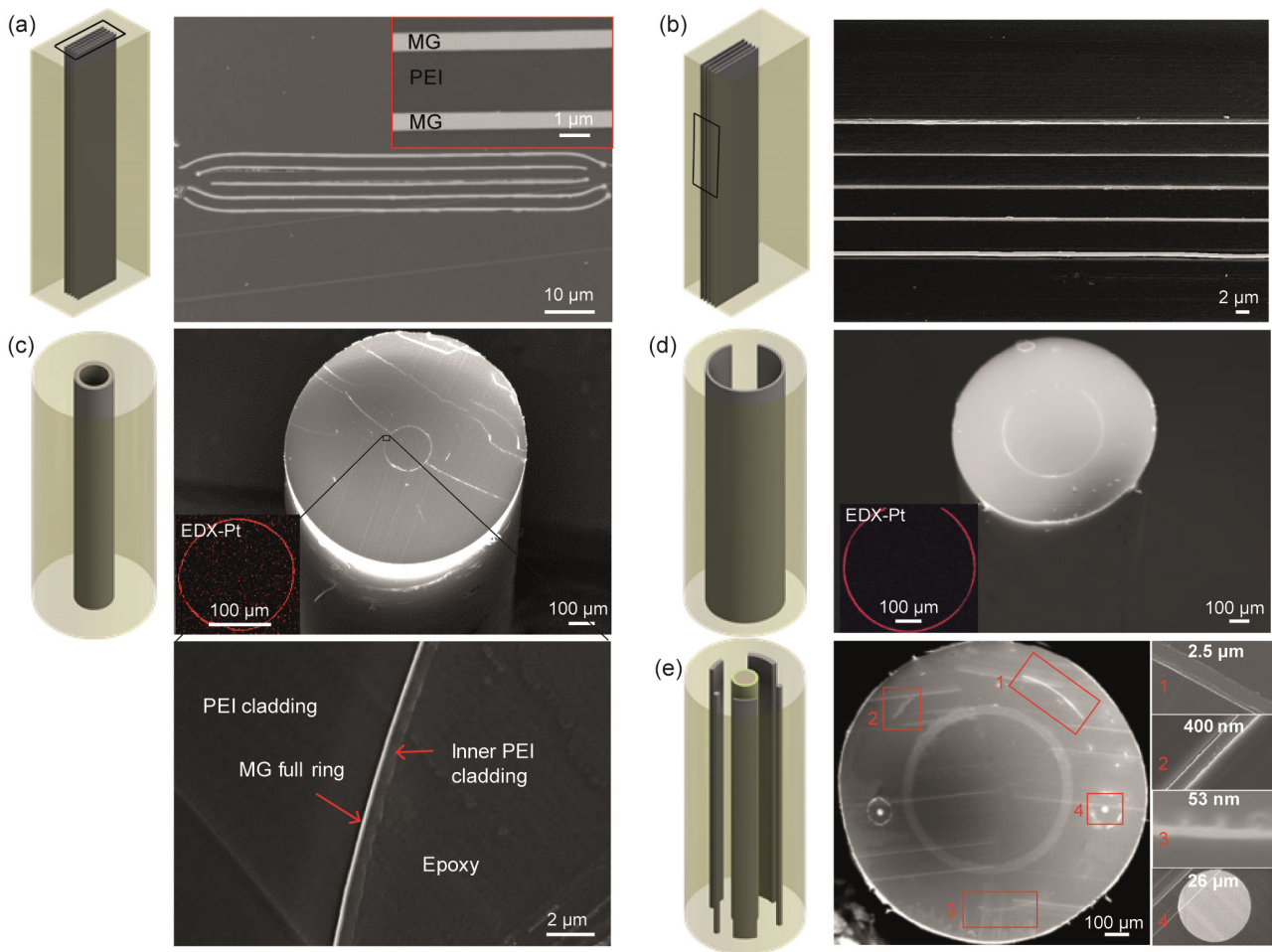
Figure 4-9 Complex MG fibers: (a) SEM micrograph (cross-sectional view) of a fiber consisting of ten alternating layers of MG and PEI. Inset: High-magnification SEM image of the interface region. (b) SEM micrograph (side view) of a fiber that consists in exposed MG arrays. (c) Top: SEM micrograph (tilted view) of a hollow core fiber surrounded by a full MG cylinder encapsulated by a thin PEI layer. Inset: EDX map of Pt. Bottom: High-magnification SEM image confirming the fiber architecture. (d) SEM micrograph (tilted view) of a fiber containing a MG slotted-cylinder. Inset: EDX map of Pt. (e) Left: SEM micrograph (cross-sectional view) of a PEI/PES waveguide fiber containing three MG ribbons and two MG rods. The MG ribbons and rods are indicated with red rectangles and their thicknesses are highlighted in the high-magnification SEM images on the right. The schematics of all fiber structures are also shown in (a)-(e).

4.2.3   Ultimate feature size

The ability to draw uniform metallic ribbons with feature sizes down to $\sim 40\ nm$ drastically contrasts with what had been previously achieved with crystalline metals. As mentioned in chapter 1, the smallest diameter of low melting temperature metal wires reported is $\sim 1\ \mu m$ [23], [28]. Further size reduction induces diameter instabilities which finally

result in the break-up of the rods. In contrast to crystalline metals which are drawn in their molten state, metallic glasses are drawn in a highly viscous state. In order to assess the resistance against break-up of our new material system, a simulation was carried out based on the instability theory. It was performed for both a tin (Sn) wire embedded in polyethersulphone (PSU) and a MG wire surrounded by the PEI cladding. An estimated instability time scale was determined and compared to the dwelling time, defined as the time spent in the hot zone of the drawing tower.

Classical Plateau-Rayleigh instability theory points out that when a cylindrical column of liquid is surrounded by another substance, a sinusoidal perturbation wave may appear at the heterogeneous interfaces between the two materials and finally lead to the breakup of the liquid. Here, we consider the MG core heated to a temperature T as a viscous cylindrical thread (diameter $2R$ and viscosity η_{core}) surrounded by an infinite viscous cladding PEI (viscosity η_{clad}). We further consider that the core is incompressible, Newtonian and isotropic.

The perturbation grows exponentially over time with an instability time scale τ that is linearly proportional to the core diameter and inversely dependent on the maximum of a function associated with the core/cladding viscosity ratio. From Tomotika's linear theory, τ can be defined as:

$$\tau = \frac{2R\eta_{clad}}{\gamma \max[(1 - x^2)\Phi(x, \eta_{core}/\eta_{clad})]} \tag{4.1}$$

where γ is the interfacial energy between the cladding and the core metal, $x = \frac{2\pi R}{\gamma}$ with λ the wavelength of the perturbation, and $\Phi(x)$ an explicitly known function [21]:

$$\Phi(x) = \frac{N(x)}{D(x)} \tag{4.2}$$

With

$$N(x) \equiv I_1(x)\Delta_1 - \{xI_0(x) - I_1(x)\}\Delta_2$$

$$D(x) = \left(\frac{\eta_{core}}{\eta_{clad}}\right)\{xI_0(x) - I_1(x)\}\Delta_1 - \left(\frac{\eta_{core}}{\eta_{clad}}\right)\{(x^2 + 1)I_1(x) - xI_0(x)\}\Delta_2 - \{xK_0(x) + K_1(x)\}\Delta_3$$
$$- \{(x^2 + 1)K_1(x) - xK_0(x)\}\Delta_4$$

where $I_0(x)$ and $I_1(x)$ are the modified Bessel functions of the 0th and 1st order, respectively. Furthermore, Δ_1, Δ_2, Δ_3 and Δ_4 are functions of x expressed in determinantal forms as follows:

$$\Delta_1 = \begin{vmatrix} xI_0(x) - I_1(x) & K_1(x) & xK_0(x) - K_1(x) \\ I_0(x) + xI_1(x) & -K_0(x) & -K_0(x) + xK_1(x) \\ \left(\frac{\eta_{core}}{\eta_{clad}}\right)xI_0(x) & K_1(x) & -xK_0(x) \end{vmatrix}$$

$$\Delta_2 = \begin{vmatrix} I_1(x) & K_1(x) & -xK_0(x) - K_1(x) \\ I_0(x) & -K_0(x) & -K_0(x) + xK_1(x) \\ \left(\dfrac{\eta_{core}}{\eta_{clad}}\right) I_1(x) & K_1(x) & -xK_0(x) \end{vmatrix}$$

$$\Delta_3 = \begin{vmatrix} I_1(x) & xI_0(x) - I_1(x) & -xK_0(x) - K_1(x) \\ I_0(x) & I_0(x) + xI_1(x) & -K_0(x) + xK_1(x) \\ \left(\dfrac{\eta_{core}}{\eta_{clad}}\right) I_1(x) & \left(\dfrac{\eta_{core}}{\eta_{clad}}\right) xI_0(x) & -xK_0(x) \end{vmatrix}$$

$$\Delta_4 = \begin{vmatrix} I_1(x) & xI_0(x) - I_1(x) & K_1(x) \\ I_0(x) & I_0(x) + xI_1(x) & -K_0(x) \\ \left(\dfrac{\eta_{core}}{\eta_{clad}}\right) I_1(x) & \left(\dfrac{\eta_{core}}{\eta_{clad}}\right) xI_0(x) & -K_1(x) \end{vmatrix} \qquad (4.3)$$

The perturbation with the highest $[(1 - x^2)\Phi(x, \eta_{core}/\eta_{clad})]$ will dominate the instability and generate break-up (which is a very conservative estimate).

We first model the instability time of a typical metal, e.g. Sn, co-drawn with a PSU cladding ($\eta_{core} = 10^{-3}\ Pa\ s$, $\eta_{clad} = 10^5\ Pa\ s$, $\gamma = 0.1\ N/m$). The $(1 - x^2)\Phi(x, \eta_{core}/\eta_{clad})$ reaches unity when x is around 0.015 (Figure 4-10(a)). The instability time versus radius given by Equation 4.1 is plotted in Figure 4-10(b). We can see that for a radius of $1\ \mu m$, the instability time is of only $2\ s$. It is not straightforward to compare this instability time to the dwelling time in the drawing tower since thermal drawing involves non-isothermal condition and a gradual decrease in diameter. Nevertheless, it indicates the major importance of capillary instabilities on the ultimate feature sizes of molten metal wires.
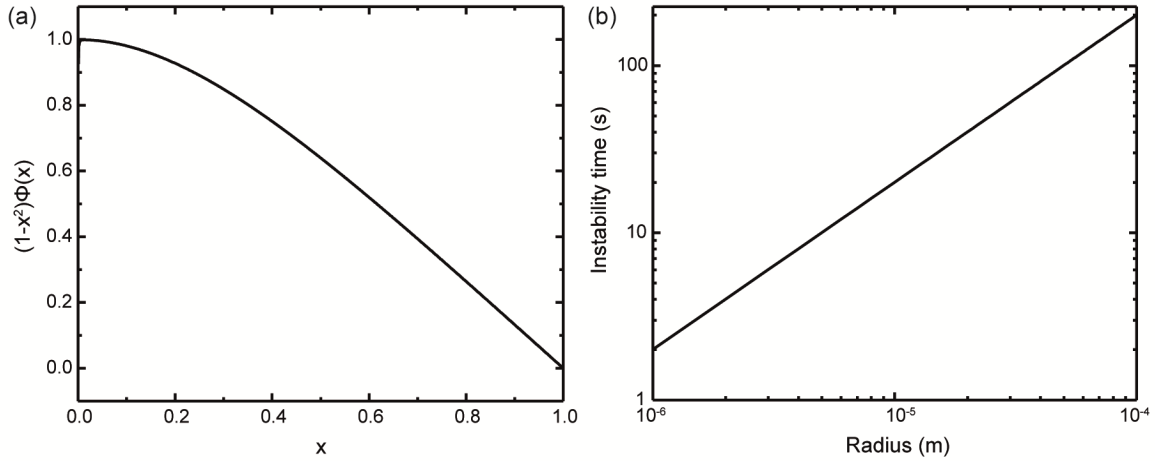
Figure 4-10 Sn/PSU system: (a) $(1 - x^2)\Phi(x, \eta_{core}/\eta_{clad})$ versus x and (b) Instability time versus Sn radius.

On the other hand, the same calculation was done for the Pt-MG/PEI system at the maximum drawing temperature (260 °C). From the literature and our rheological measurements, we estimate $\eta_{\text{Pt-MG},260\,°C} \approx 4.8 \times 10^7\ Pa\ s$ and $\eta_{\text{PEI},260\,°C} \approx 8.2 \times 10^5\ Pa\ s$ corresponding to a ratio of 59. Furthermore we assume that the interfacial energy is dominated by the surface tension of the metallic glass, $\gamma = 1\ N/m$ [149]. This is a conservative estimate considering that the interface between MG and PEI is intimate. We obtain $(1 - x^2)\Phi(x, \eta_{core}/\eta_{clad})$ values almost three orders of magnitude lower compared to that of the Sn/PSU system (Figure 4-11(a)). This creates a much longer instability time,

as shown in Figure 4-11(b). In the MG system, the instability time for a radius of $1\ \mu m$ is around $300\ s$ which rationalizes the higher resistance to capillary break-up observed for the MG/PEI fiber and the sub-micron feature sizes obtained.
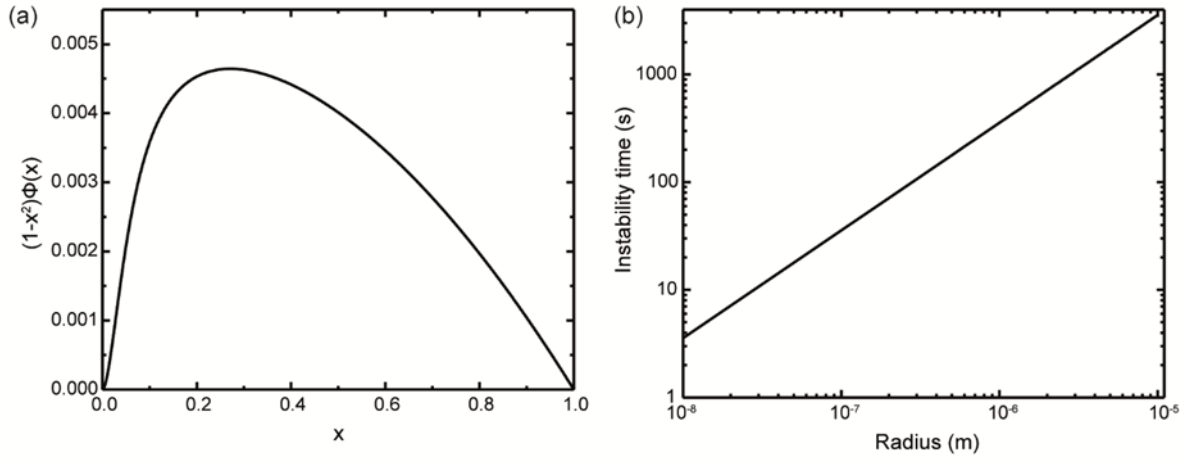
Figure 4-11 Pt-MG/PEI system: (a) $(1-x^2)\Phi(x,\eta_{core}/\eta_{clad})$ versus x. (b) Instability time versus Pt-MG radius.

Finally, we tried to evaluate if capillary instability could be the cause of the break-up in the $50\ nm$ range. We determined the evolution of the instability time during thermal drawing of a Pt-MG rod with an initial diameter of $900\ nm$ into a $30\ nm$ diameter MG rod. In order to get the viscosity of the core and the cladding during the draw, we measured the temperature distribution in the oven with a thermocouple. We fitted the measurements with a quadratic temperature profile $T(z) = \frac{(T_g - T_{max})}{L^2} z^2 + T_{max}$ with $T_{max} = 258\ ^\circ C, T_g = 228\ ^\circ C$ and $L = 3\ cm$. Furthermore, we estimated the velocity profile $v(z)$ based on the conservation of mass as developed in section 1.1.3. We used our usual feeding speed $v_{feed} = 1\ mm\ min^{-1}$ and a drawing speed $v_{draw} = 900\ mm\ min^{-1}$. Knowing the temperature dependent viscosity of both materials, the instability time in the neck down region could be estimated and is shown in Figure 4-12.
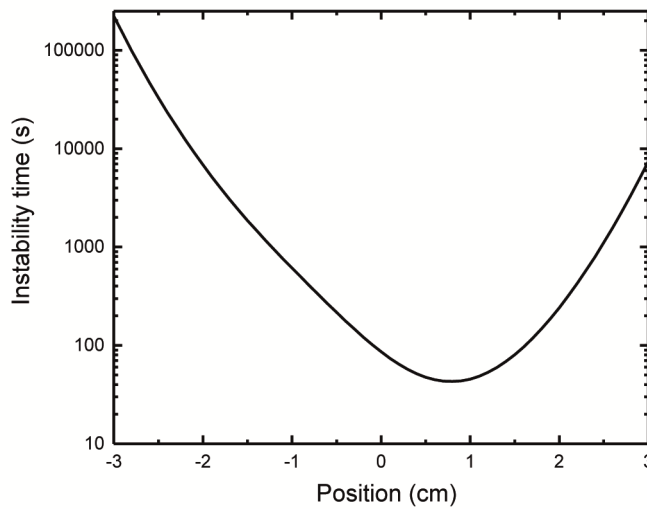
Figure 4-12 Instability time in the neck-down region of the Pt-MG/PEI system.

In order to determine the stability of the MG rod, it is required to compare the processing time (the time when the material dwells in the neck-down region before it exits the furnace) with the capillary instability time. To do so, we use the growth factor Γ defined as [22]:

$$\Gamma = \int_{-L}^{L} \frac{dz}{v(z)\tau(z)}$$

Where $\tau(z)$ is the instability time and $\frac{dz}{v(z)}$ is the dwelling time at each position in the neck-down region. $\Gamma \gg 1$ corresponds to breakup while $\Gamma \ll 1$ indicates a stable draw. With our parameters we obtain:

$$\Gamma = 0.79$$

This value does not completely fulfill the criteria of $\Gamma \ll 1$, but we made many conservative assumptions. Therefore, we can expect a stable draw under these conditions. Experimental observations confirm this result since no large fluctuation in diameter is present even close to the break-up thickness. The break-up seems therefore not to be caused by fluid instabilities.

Optical microscopy (OM) analysis suggests that the break-up may be caused by cracks growing transversely when the ribbons reach a critical thickness. Figure 4-13 exposes three OM micrographs taken at different positions along a fiber containing a thin Pt-MG ribbon. The drawing speed was varied during the draw, and therefore, the MG thickness changed, while other parameters were kept constant. An estimation of the ribbon thickness was calculated for each fiber depending on the draw down ratio. It is apparent that below a critical thickness, the ribbon seems to break into small pieces (Figure 4-13 middle). At slightly larger thicknesses, the presence of small cracks initiating from the edge of the ribbon can be observed. We therefore hypothesized that the thickness limitation could be due to the onset of crystallization during the drawing process. The presence of nanocrystals could induce a resistance to flow that eventually leads to mechanical break-up.
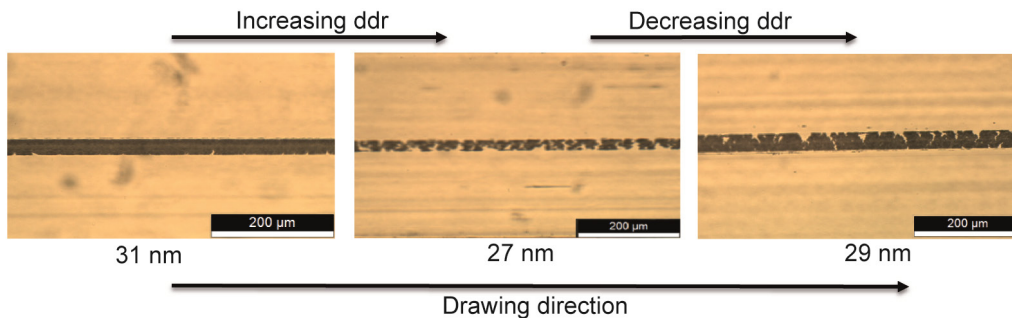
Figure 4-13 OM images of a third drawn Pt-MG/PEI fiber along the drawing direction.

To confirm this hypothesis, we analyzed these broken ribbons by TEM. Thanks to the sub 100 nm thickness, only an etching step in NMP to remove the PEI cladding was required before depositing the ribbons on a TEM grid. In addition to the characteristic diffuse rings from the amorphous matrix, a thin arc can be detected close to the first and second ring of the SAED pattern as shown in Figure 4-14(a). Dark field TEM images formed by carefully selecting the arc alone reveal the presence of an array of elongated nanocrystals distributed both inside the ribbons (Figure 4-14(b)) and at the

crack surface (Figure 4-14(c)). Needle-like crystals have been reported for the Pt-MG after isothermal holding at 292 $°C$ and assumed to be an indication of a interfacial controlled growth with high anisotropy [138]. The variation of intensity along the diffraction ring indicates that the nanocrystals have a preferential orientation. We believe that the flow of the amorphous matrix induces the orientation in the drawing direction. Finally, the nanocrystals can be observed on HRTEM images and have a sub-10 nm diameter (Figure 4-14(d)). The presence of nanocrystals in thicker samples could not be demonstrated by TEM analyses since their signal might be conceal by the diffuse amorphous halo. Nevertheless, we assume that they are generally present in the third drawn ribbon and that when the volume fraction of these nanocrystals relative to the amorphous matric is locally large enough, they can induce a resistance to flow that eventually leads to the mechanical breakup. The presence of nanocrystals along the crack path confirms this scenario.
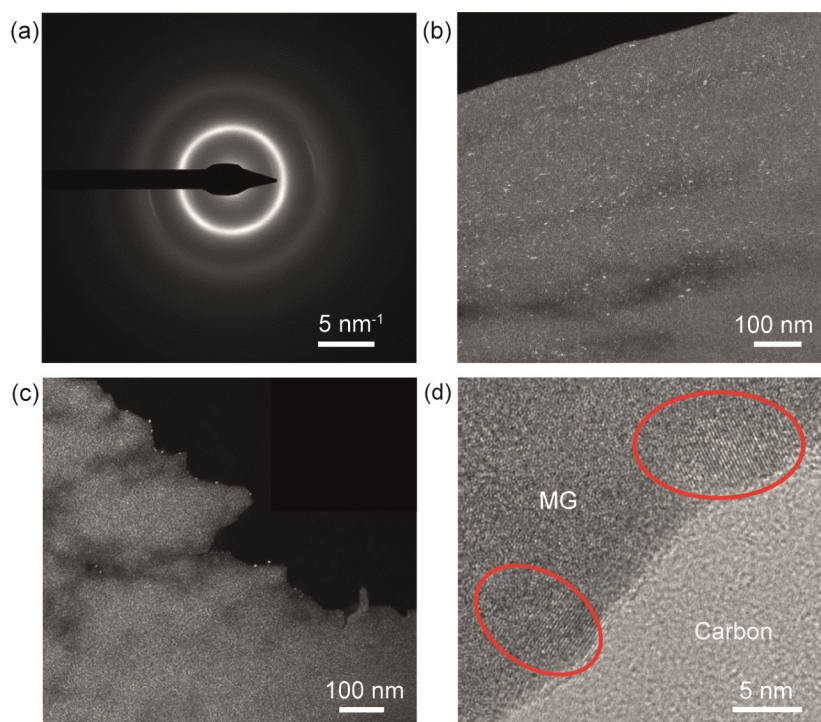
Figure 4-14 TEM characterization of a Pt-MG broken ribbon: (a) SAED. (b) DF image in an intact part. (c) DF image at the fracture surface. (d) HRTEM image at the fracture surface.

4.2.4 Influence of thermal drawing on the crystallization kinetics – nanometer range

We performed in situ heating TEM experiments to study the crystallization kinetics of Pt-MG ribbons with thicknesses of 45, 95 and 105 nm that were obtained in the third-drawn step. We first investigated the crystallization temperature (T$_x$) variation via heating the samples from room temperature to 400 or 500 $°C$, with a 0.5 s heating to 170 $°C$ followed by a heating ramp of 40 $°C\ min^{-1}$. SAED patterns were recorded each second during the experiment and synchronized with the temperature ramp profile. Figure 4-15(a) shows some example of SAED patterns for each ribbon thickness. At room temperature, only the diffuse rings are present which confirms that the ribbons are still mostly in their amorphous state. Upon heating, some sharper arcs appear indicating the nucleation start and at the end of the test all the samples have been fully crystallized. The T$_x$ can be estimated by analyzing the contrast change in the SAED patterns in the highlighted area compared to the background (see experimental methods). The abrupt increase of the relative intensity,

denoted by the red arrows in Figure 4-15(b), indicates the onset of crystallization, which is defined as T_x. We observe that T_x decreases with decreasing ribbon thickness from 292 °C for the 105 nm thick ribbon down to 268 °C for the 45 nm thick ribbon. First, it is interesting to note that the thicker ribbons should be the one with the longest holding at high temperature during thermal drawing since a higher thickness means a slower drawing speed. Nevertheless, the opposite trend is observed which suggests that other parameters influence the crystallization kinetics. Secondly, 268 °C is very close to the maximum temperature we measured during thermal drawing (255-260 °C) which supports the theory of an increase in crystal fraction density in this thickness range inducing the break-up.

Figure 4-15 In situ heating TEM analysis of Pt-MG ribbons with thicknesses of 45, 90 and 105 nm: (a) Snapshot SAED patterns of nanoribbons when heated at a rate of 40 °C min^{-1}. The red rectangles indicate the onset of crystallization. (b) Quantification of T_x based on the intensity change of diffraction pattern contrasts.

In order to further study the crystallization kinetics of these samples, we then investigated the crystallization starting time (t_c) during an isothermal annealing at 260 °C. Some snapshot SAED patterns are shown in Figure 4-16(a) and the quantitative measurements of the t_c of the ribbons are presented in Figure 4-16(b). The onset of crystallization is determined by the abrupt change in intensity, denoted by the red arrows. t_c decreases rapidly with decreasing ribbon thickness which further demonstrates that the crystallization kinetics increase when reducing the ribbon thickness. In particular, the t_c of a 45 nm ribbon is as low as ~32 s. Crystal nucleation is obviously increased at such thickness and it confirms our theory that a higher density of nanocrystals could be the reason for the break-up observed. The SAED patterns also reveal the slow crystal growth rate at this temperature since even after one hour for the thicker sample, the ribbons remain dominantly amorphous. Therefore, the thicker MG ribbons still retain their integrity during drawing.
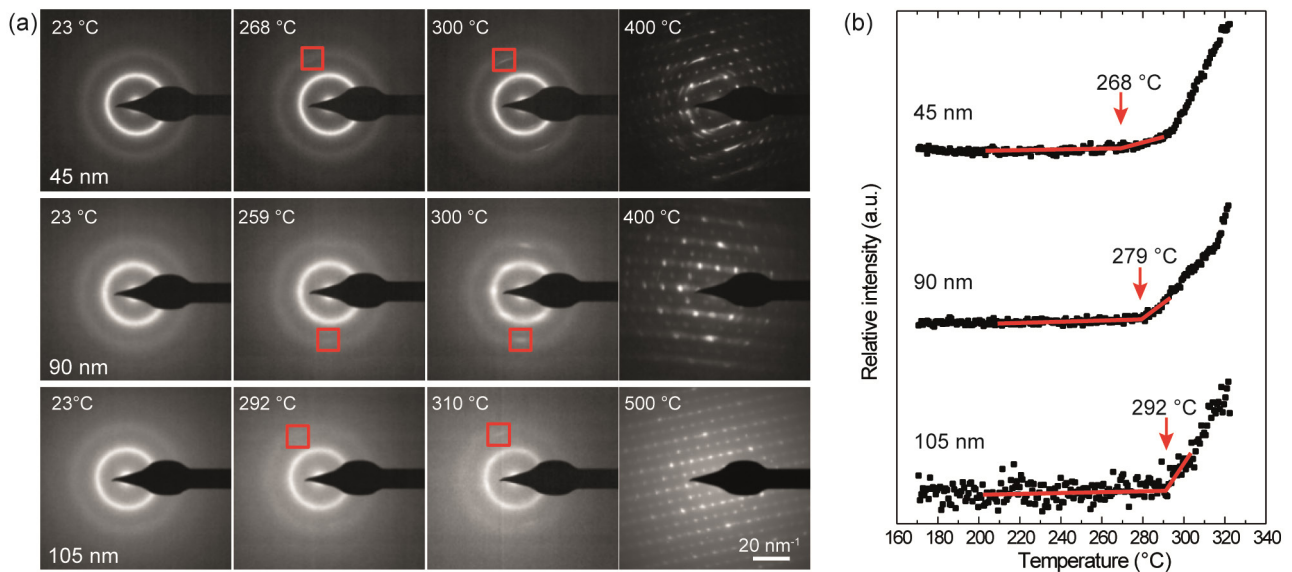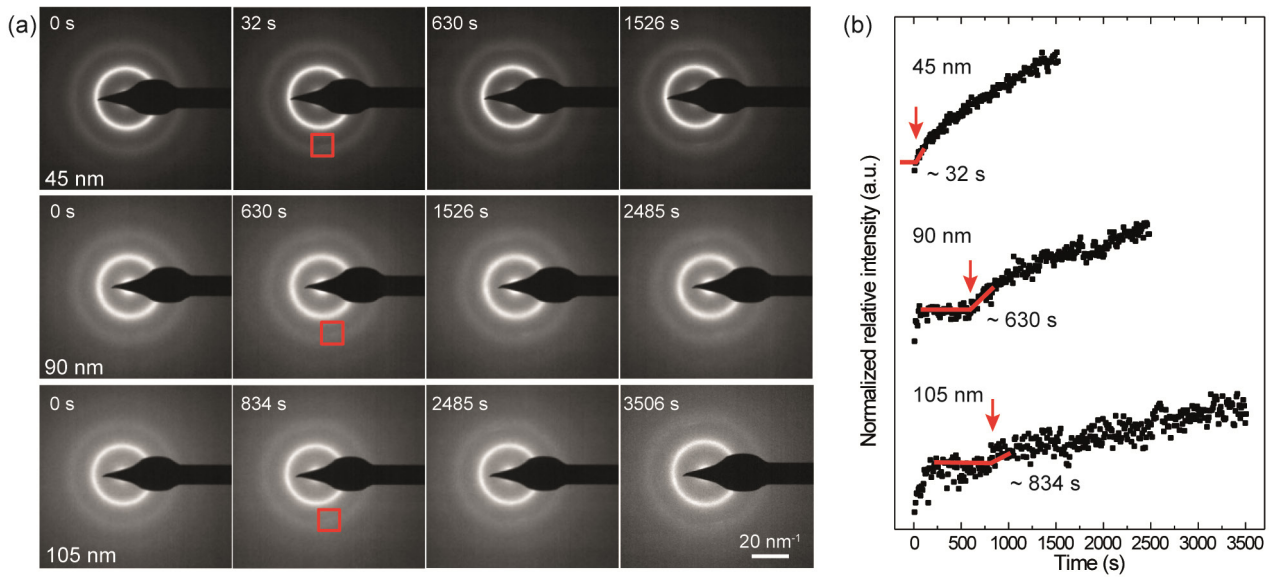
Figure 4-16 in situ TEM heating TEM analysis of Pt-MG ribbons with thicknesses of 45, 90 and 105 nm: (a) Snapshot SAED patterns of nanoribbons when isothermally heated at 260 °C. The red rectangles indicate the onset of crystallization. (b) Quantification of the crystallization time based on the intensity change of diffraction pattern contrasts.

The size-dependent crystallization kinetics of MG nanoribbons observed here may be explained by the increase in surface-to-volume ratio as well as the larger amount of deformation of thinner samples. Previous published studies reported a similar size effect in nanorods and attributed it to faster heterogeneous surface nucleation [96], [97]. The latter has been observed in other metallic glasses but its origin remains unclear [99], [100]. Furthermore, deformation-enhanced crystallization has been reported in the supercooled liquid region of bulk BMGs [83]–[86].

4.2.5 Influence of thermal drawing on the crystallization kinetics – micrometer range

In order to study the influence of the thermal drawing process with no or only small influence of a size effect, we studied the crystallization kinetics of once drawn Pt-MG ribbons with thicknesses ranging from ~27 to ~1.75 μm. As cast Pt-MG ribbons of a thickness of ~70 μm were consolidated between two PEI plates and drawn under draw down ratios (ddr) between 2.6 and 40 as illustrated in Figure 4-17(a). After thermal drawing, the polymer cladding was either mechanically removed or chemically etched in order to retrieve the MG ribbons. We first confirmed that the drawn ribbons retained a fully amorphous state with XRD analyses. The XRD patterns of the as cast and three drawn ribbons (ddr 6.4, 10 and 20) are shown in Figure 4-17(b). They exhibit only a broad diffraction peak at $2\theta = 40°$ and a smaller one at $2\theta = 75°$ which indicates their amorphous state after drawing.
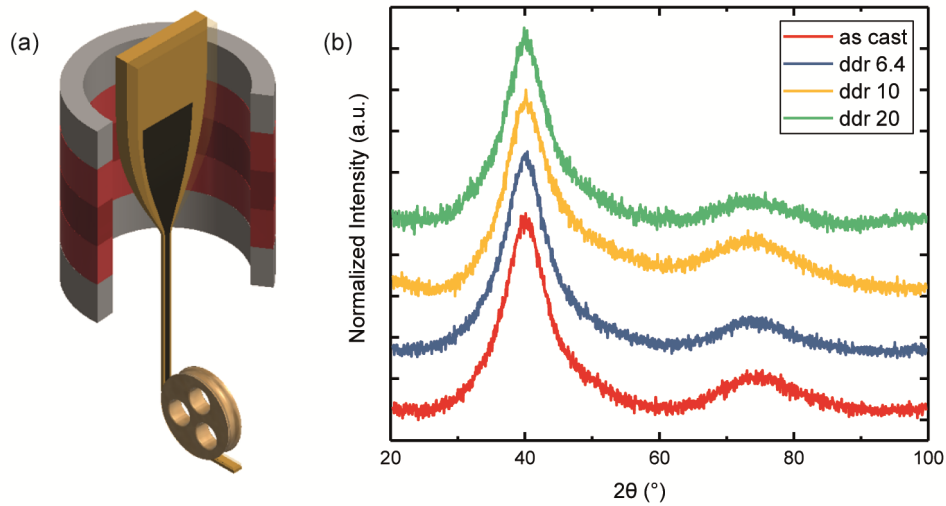
Figure 4-17 (a) Schematic of the thermally drawn fibers. (b) XRD patterns of the as cast and three drawn Pt-MG ribbons (ddr 6.4, 10 and 20).

Then, we investigated the isothermal crystallization kinetics at 255 $°C$ with differential scanning calorimetry (Figure 4-18). The micrometer thickness of the ribbons allowed us to collect enough material at each ddr to obtain samples of 3.5-6 mg which is above the detection limit of the DSC. A significant shift of the crystallization peak is observed between the as-cast sample and the drawn samples. A decrease in the crystallization onset time t_c for the drawn samples was expected due to the annealing occurring during the drawing process. However, t_c should increase with the ddr since drawing at a higher speed means spending less time at high temperature. An opposite trend is observed here with a strong decrease of t_c at low ddr followed by a plateau with constant t_c values. Furthermore, the exothermic crystallization peak splits into two separated peaks above a ddr of 2.6. Therefore, while the crystallization of the as cast and ddr 2.6 samples occurs via a single exothermic process, a two-step crystallization process is observed for the other samples. It reveals that thermal drawing has an impact on the microstructure of the BMGs either modifying its structural ordering or inducing fluctuations in composition. It is interesting to note that above a critical ddr all the DSC curves overlap within experimental uncertainties, even though the ribbons experience different amount of deformation and temperature history.
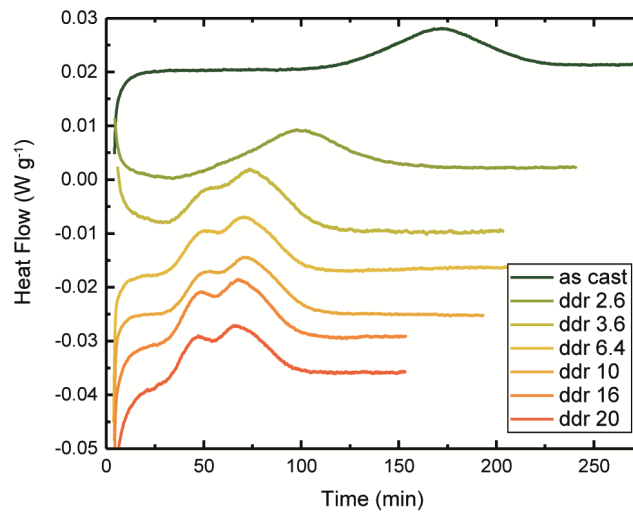
Figure 4-18 255 °C isothermal DSC curves for the as cast and drawn ribbons (ddr 2.6 to 20)

In order to explain these different crystallization mechanisms, we then focused on the analysis of the microstructure of the crystallized samples. XRD patterns of the as cast and ddr 10 samples after crystallization at 260 °C are shown in Figure 4-19(a). Notable differences can be observed between both samples, in particular at low angles. The relative intensity of each peak varies significantly and some peak shifts are also observed. Due to the complexity and the finesse of the microstructure, it is difficult to identify the phases and thus determine if some new phases have appeared. The variance in peak intensity could be caused by the texturing of some phases, which would modify the relative intensity of the same crystalline phases.
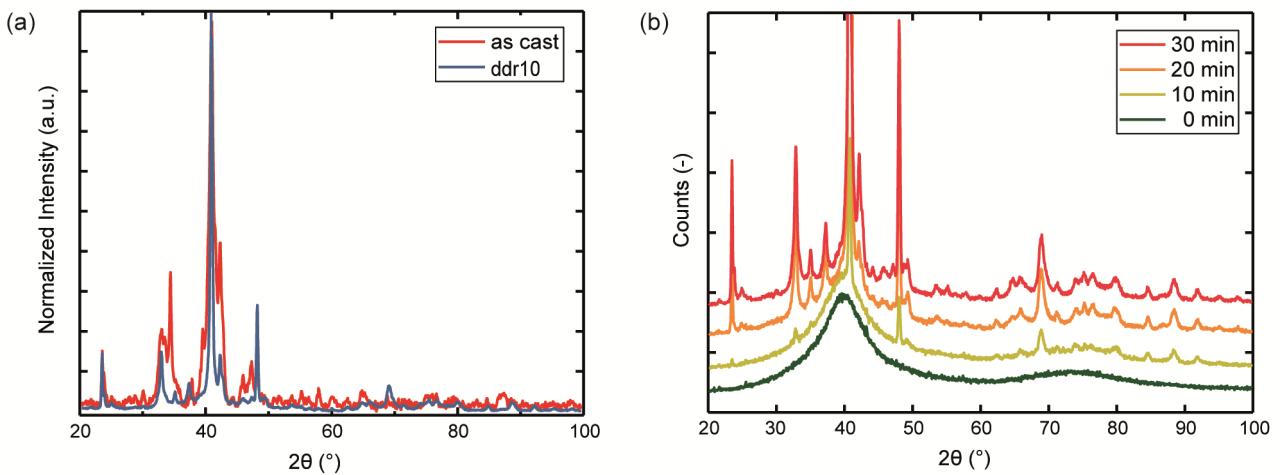
Figure 4-19 (a) XRD patterns of an as cast and ddr 10 ribbons fully crystallized at 260 °C. (b) In-situ XRD patterns of the ddr 10 MG-ribbon at different times during an annealing at 260 °C.

In order to study the crystallization process, continuous in-situ XRD annealing experiments at 260 °C were performed on a ddr 10 ribbon. The patterns recorded every 10 minutes are presented in Figure 4-19(b) and show that few peaks are already appearing after 10 minutes. The latter continue to grow during the annealing while peaks corresponding to other phases appear after 20 minutes. These results reveal that the first peak observed in the DSC is caused by the crystallization of a stable phase and not by some metastable phase acting as precursors for further crystallization. The

crystallization of the first phase can modify the composition of the surrounding amorphous matrix and therefore enhance the crystallization of the rest of the sample.

In order to confirm the XRD analysis, Backscattered-electron (BSE) SEM micrographs of as cast, ddr 2.6 and ddr 3.6 samples were acquired after being fully crystallized in the DSC at 260 °C (Figure 4-20(a)). The images reveal the presence of several phases, homogeneously distributed in the samples. Moreover, a clear microstructural difference can be observed between the undeformed, or slightly deformed, and the deformed samples. The first ones show a lamellar structure with no preferential orientation. On the other hand, smaller ellipsoidal grains are visible in the deformed samples aligned in the drawing direction. This apparent texture could induce the differences observed in the peak intensity in the XRD patterns.
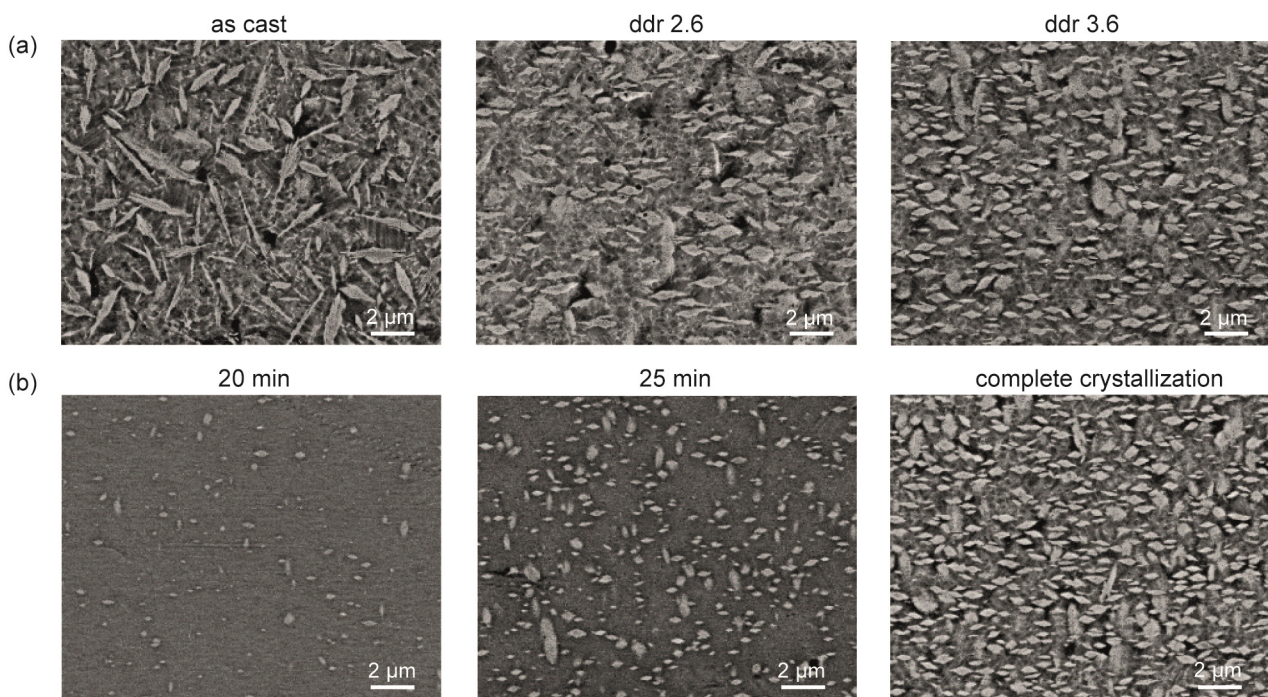
Figure 4-20 BSE SEM micrographs of (a) crystallized as cast, ddr 2.6 and ddr 3.6 Pt-MG ribbons, (b) ddr 10 Pt-MG ribbons after isothermal annealing at 260 °C for 20, 25 and 140 min.

BSE SEM micrographs of the ddr 10 samples were also recorded after partial crystallization at 260 °C to study the solidification sequence and are shown in Figure 4-20(b). The annealing times were selected to compare the microstructures at the start of the first exothermal peak (20 min), at the maximum of the first peak (25 min) and after complete crystallization. The images show that the first phase crystallizing corresponds to small grains aligned in the drawing direction. During further annealing, these grains continue to nucleate and several other grains nucleate simultaneously corresponding to the second exothermic peak.

The analysis of the microstructure reveals different crystallization processes depending on the thermal drawing parameters. However, the mechanism responsible for this transition is still unclear and is discussed hereafter. First, thermal annealing during the draw cannot explain the observed crystallization kinetics. Indeed, a higher ddr means a faster drawing speed and a shorter time at high temperature, and therefore a longer time before crystallization would

be expected which is the contrary to the experimental results. Secondly, the deformation has an impact but, interestingly, the crystallization kinetics do not seem to depend on the total strain or maximum strain rate. A critical amount of deformation is nevertheless required for the appearance of the two crystallization peaks. Since, some studies revealed the crystallization dependence on the shear rate in the SCLR, we also compared the crystallization kinetics of some ribbons drawn at the center (i.e. small shear rate) and on the side of the preform (i.e. larger shear rate) as shown in Figure 4-21(a). The DSC results reveal that both ribbons follow the same crystallization kinetics within experimental errors and therefore we ruled out the effect of the shear rate (Figure 4-21(b)).
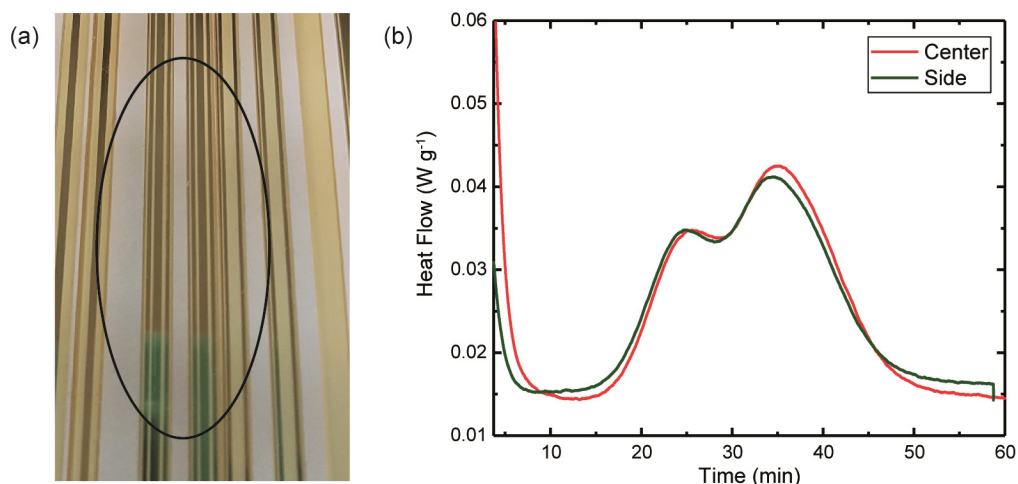
Figure 4-21 (a) Photograph of the drawn fibers. (b) 260 °C isothermal DSC curves of Pt-MG ribbons positioned at the center and on the sides of the preform

Previous studies revealed that the deformation had the largest impact when occurring below or close to the T_g. At room temperature, it has been demonstrated that deformation and especially the formation of shear band modifies the atomic configuration [82] and/or the short [81] and medium-range order [70]. Above T_g the deformation dependent crystallization is assumed to be caused by an interplay between generation of free volume (deformation) and annihilation of free volume (thermal annealing), and at high temperature the deformation dependence is strongly reduced [88]. These studies might help us understand our experimental results. Indeed, a specificity of thermal drawing is that the deformation does not take place at a constant temperature. For all the samples, deformation starts at temperature around T_g. Then, the largest amount of deformation and highest strain rate, which are determined by the ddr, occur at higher temperatures, around T_g + 30 $°C$. Since above a critical ddr similar crystallization kinetics are observed, one can assume that the part controlling crystallization is the beginning of the deformation which is similar for all the samples. This low temperature deformation can modify the atomic structure and promote crystallization. Further experiments would be required to support this hypothesis.

4.3 Thermal drawing of Au-BMG and PMMA

We turn to the investigation of the thermal drawing of a new BMG composition, in an effort to extend the library of glassy materials compatible with the thermal drawing process.

4.3.1 Preliminary tests

Since the oven of the drawing tower is opaque and due to the difficulty to accurately determine the temperature profile inside the drawing tower, it can be complicated to find the optimal parameters when drawing a new material system and understand the factors preventing a successful draw such as temperature, drawing speed or too long time at high temperature. Therefore, some preliminary tests were performed in a dynamic mechanical analyzer (DMA). This instrument allows us to perform tensile deformation experiments of miniaturized preforms at precise temperatures or during temperature ramps. The samples were processed by stacking several films of PMMA, with or without an Au-MG ribbon in the middle, and consolidating them in a hot press to obtain small plates of $\sim$0.8 mm thickness. Small rectangles were then simply cut from this plate to imitate small preforms, as shown in Figure 4-22(b) (left sample).

The deformation of the sample was measured during a heating ramp of 3 $°C \, min^{-1}$ under a constant stress of 0.15 MPa (Figure 4-22(a)). The PMMA sample starts deforming slowly at a temperature of $\sim$110 $°C$ and more sharply at around 150 $°C$. The first increase in deformation is caused by mostly elastic deformation due to the decrease in Young's modulus above the T_g, while above 145 $°C$ the deformation is caused by polymer flow, enabled by the low viscosity. The latter is the important range for thermal drawing. The temperature at which this transition occurs depends on the stress applied but it gives a good estimation of the temperature required for thermal drawing. The sample containing the Au-MG ribbon started deforming at higher temperature, which indicates that the Au-MG limits the deformation, certainly due to its higher viscosity. Nevertheless, a significant deformation could take place while keeping the sample integrity as shown by the photos of the deformed sample in Figure 4-22(b).
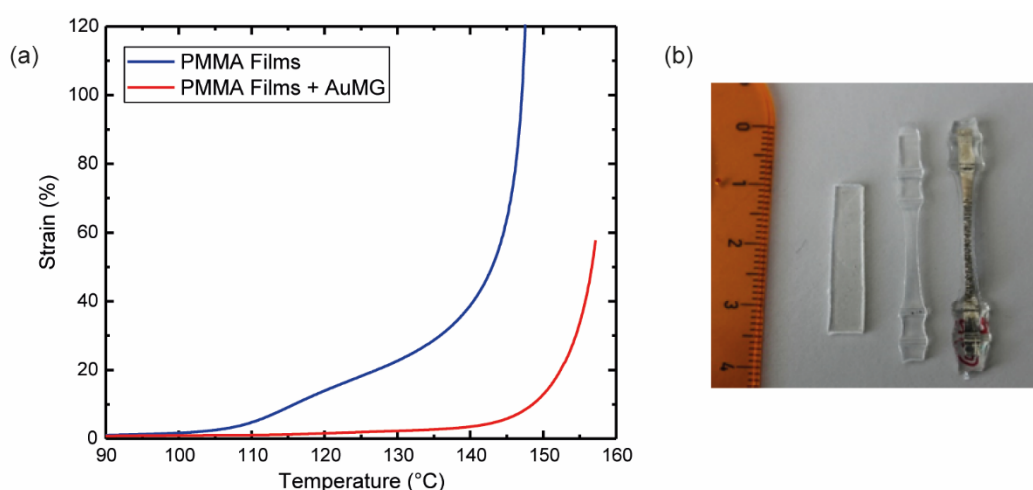
Figure 4-22 DMA characterization (a) Temperature dependent strain of the PMMA and PMMA/Au-MG samples. (b) Photograph of the samples before and after testing.

The next step consisted in deforming larger preforms on a hot plate. The preforms were fabricated following the same procedure than above with larger PMMA films. The temperature of the hot plate was increased while slightly pulling on

each side of the preform until softening occurred. A stronger pulling was then applied to try to deform the preform in a controlled way. A large deformation could be obtained in several preforms as shown in Figure 4-23(a). Furthermore, the deformation and integrity of the Au-MG was confirmed by SEM cross-sectional micrographs (Figure 4-23(b)). Starting with an Au-MG ribbon with a thickness of $\sim 30\ \mu m$, thicknesses down to 7 μm were obtained.
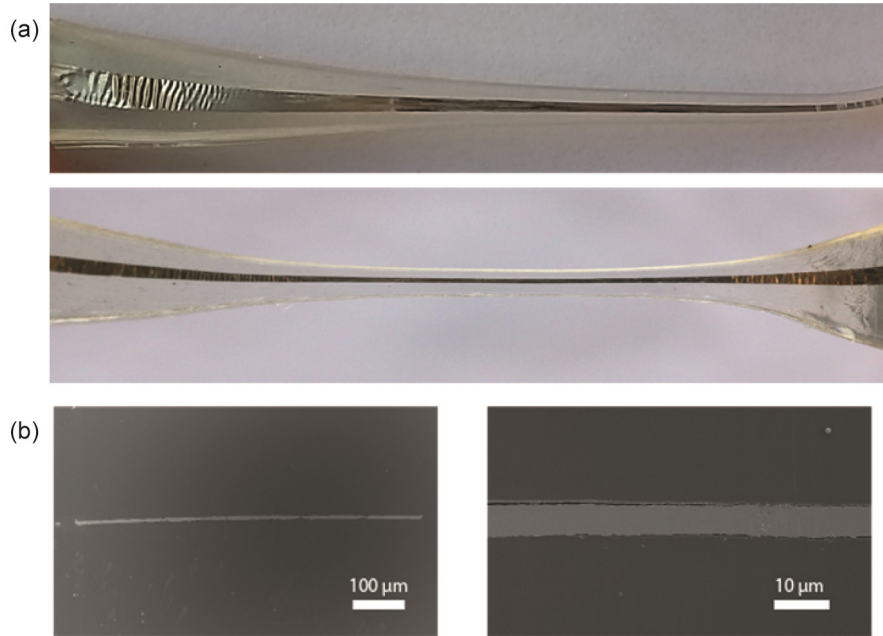
Figure 4-23 (a) Photographs of deformed preforms. (b) Cross-sectional SEM micrographs of the deformed Au-MG ribbon.

The occurrence of crystallization during stretching was investigated via XRD. A small sample was cut in the center of the deformed area and the PMMA cladding was dissolved in acetone. A XRD spectra was also recovered for the as-received sample to enable easier comparison and is shown in Figure 4-24(a). The spectrum of the melt-spun Au-MG ribbon confirms the amorphous structure characterized by only a broad bump around 40°. On the other hand, the spectrum of the stretched preform displays several sharper peaks in the same range (Figure 4-24(b)) induced by some long-range ordering. This demonstrates that a significant fraction of the metallic glass has started to crystallize and attests of the small processing windows available for the thermal drawing of this metallic glass.
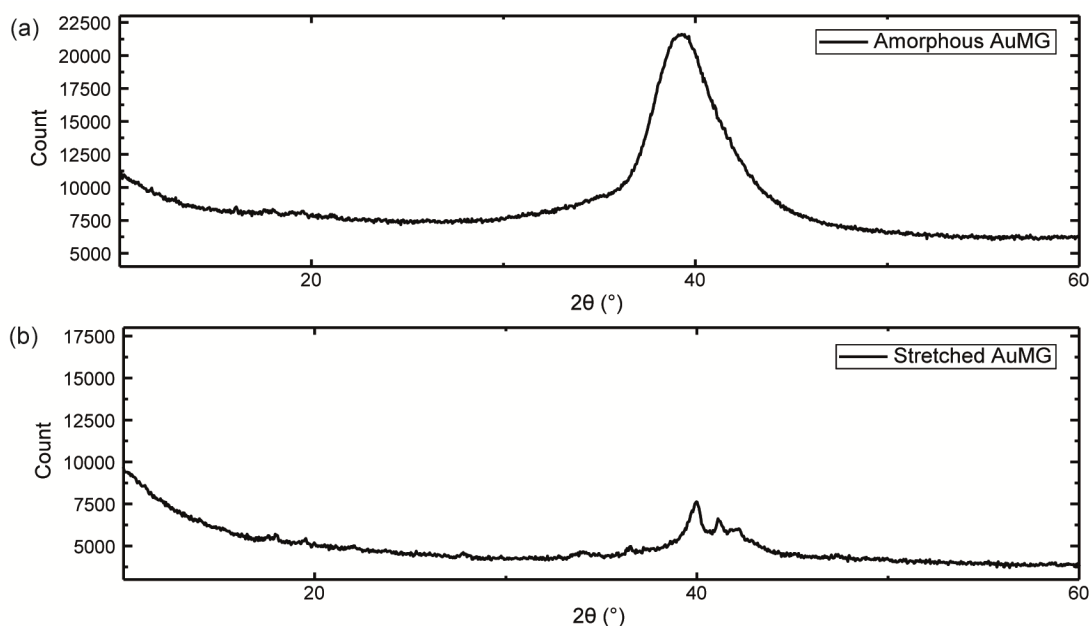
Figure 4-24 XRD pattern of an (a) amorphous Au-MG ribbon and a (b) stretched Au-MG ribbon.

Nevertheless, we attempted to thermally draw the Au-MG ribbon inside a PMMA film cladding. At first, a preform not containing the Au-MG was drawn in order to define the lowest drawing temperatures. The same parameters were then set for the first Au-MG preform. The PMMA cladding deformed relatively quickly but the fiber broke directly after the bait-off, before any Au-MG could be drawn. The break-up was assumed to be due to the too large difference in viscosity between the Au-MG and the polymer cladding. The cladding could easily deformed while the MG was still at too high viscosity to flow easily. In the next preform, the Au-MG ribbon was positioned close to the bottom of the preform so that it could be directly pulled during the bait-off. Lowering the oven temperature and hanging a heavier weight in order to enhance the deformation at higher viscosity enabled us to deform the preform as shown in Figure 4-25(a). However, the drawing could not reached a steady state and the fiber broke quickly due to the too high viscosity which limited the flow. A second PMMA cladding material, referred as "PMMA plate" later in this work, was also tested since it seemed to be drawable under higher stress. Nevertheless, despite decreasing as much as possible the drawing temperature, the Au-MG ribbons were observed to crystallize in the furnace and could not be drawn (Figure 4-25(b)).
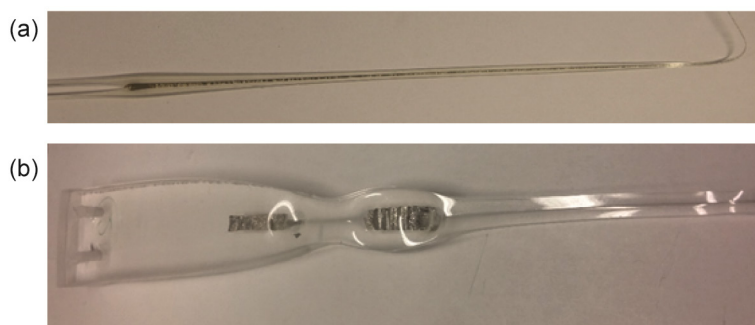
Figure 4-25 Photographs of drawn preforms (a) PMMA films cladding with a heavy weight (b) PMMA plate cladding.

4.3.2 PMMA cladding characterization

These preliminary results highlighted the fast crystallization kinetics at the drawing condition and the influence of the PMMA type on the deformability of the fibers. Next, the thermo-mechanical properties of different types of PMMA were analyzed in order to find an appropriate cladding, i.e. having a lower T_g and a drawing viscosity reached at lower temperature. These properties depend on the polymer molecular weight, thus a third PMMA (Aldrich) with a lower MW was added to the study and is referred as "PMMA powder" in the following part.

Gel permeation chromatography (GPC) was carried out to determine the molecular weight of the PMMAs. The obtained chromatograms are shown in Figure 4-26 and the deduced molecular weights, number averaged (Mn) and weight averaged (Mw), and the polydispersity indexes (PD) are given in Table 4.1. First, we can see that the PMMA plate has the highest MW, while the PMMA film has the lowest. Secondly, it is interesting to note that two peaks appear in the chromatogram of the PMMA film. This indicates that this PMMA is not completely pure and contains a second type of molecule in a relatively high quantity. According to the manufacturer material data sheet, this impact-modified grade of PMMA contained indeed a few percent of elastomer.
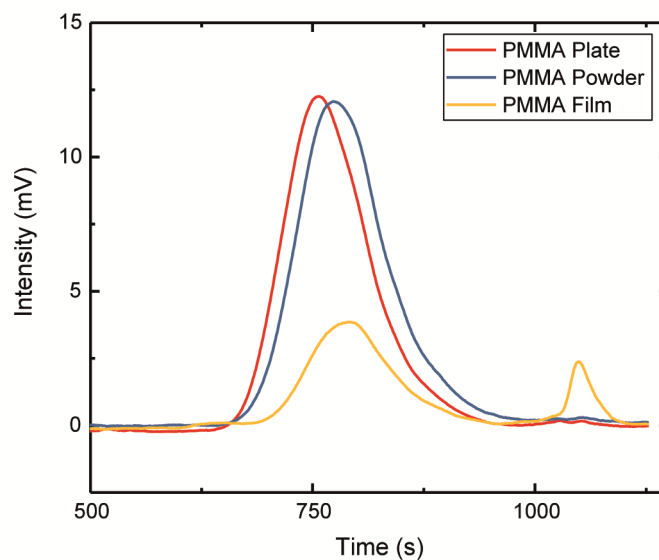
Figure 4-26 GPC chromatographs of the three types of PMMA.

Table 4.1 Molecular weight and polydispersity index calculated for the three PMMAs

Polymer	Mn	Mw	PD
High MW PMMA	68'594	111'419	1.62
Low MW PMMA	50'418	85'143	1.69
PMMA Films	39'470	67'920	1.72

To investigate the influence of the elastomer content on the viscoelastic properties, the two low MW PMMAs were characterized in the DMA in tension mode with an oscillatory strain of 0.02 % at 1 Hz. As can be seen in Figure 4-27, the PMMA film has a storage modulus three times smaller than the PMMA powder and the crossover point

between the storage and loss modulus is 10 °C lower. The latter corresponds to the transition from elastic dominated to viscous dominated deformation, where the material can flow. A lower crossover temperature correlates with a lower drawing temperature which could prevent crystallization. At the same time, the preliminary tests also revealed the requirement to have a strong cladding to be able to pull the Au-MG ribbon at the start of the draw. Therefore, the PMMA powder having higher moduli fulfills better this second requirement.
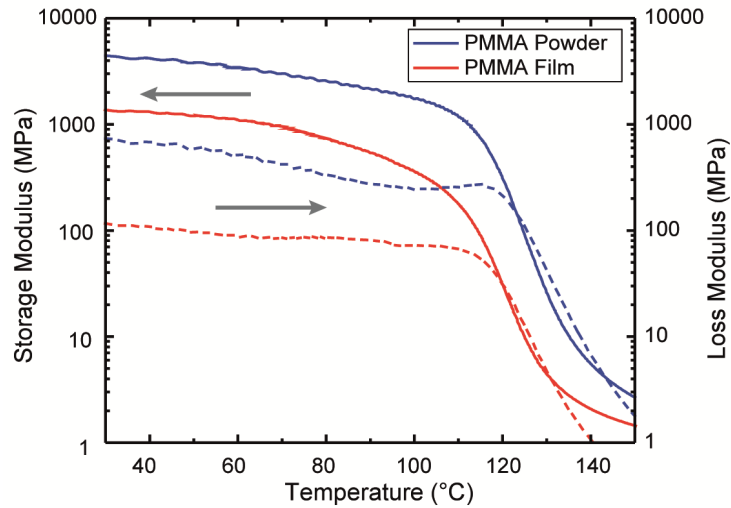
Figure 4-27 Rheological properties of the PMMA powder and PMMA film.

Further calorimetric and rheological tests on the PMMA powder and plates were performed. The results of the DSC experiments are shown in Figure 4-28(a). The measured T$_g$ equal 104 °C for the PMMA powder and 110 °C for the PMMA plate, confirming the influence of the molecular weight. Furthermore, the viscosity was measured in a rheometer operating in oscillatory shear mode using hot-pressed samples, and the temperature dependent viscosity is presented in Figure 4-28(b). As expected, at the same temperature, the PMMA powder viscosity is lower. Especially, it reaches the value of 10^6 $Pa\ s$ at around 150 °C instead of around 175 °C for the PMMA plate. Since the crystallization time of the Au-MG at 150 °C has been reported to be about 1000 s, this PMMA seems to fulfill the requirements for a successful stable fiber drawing.
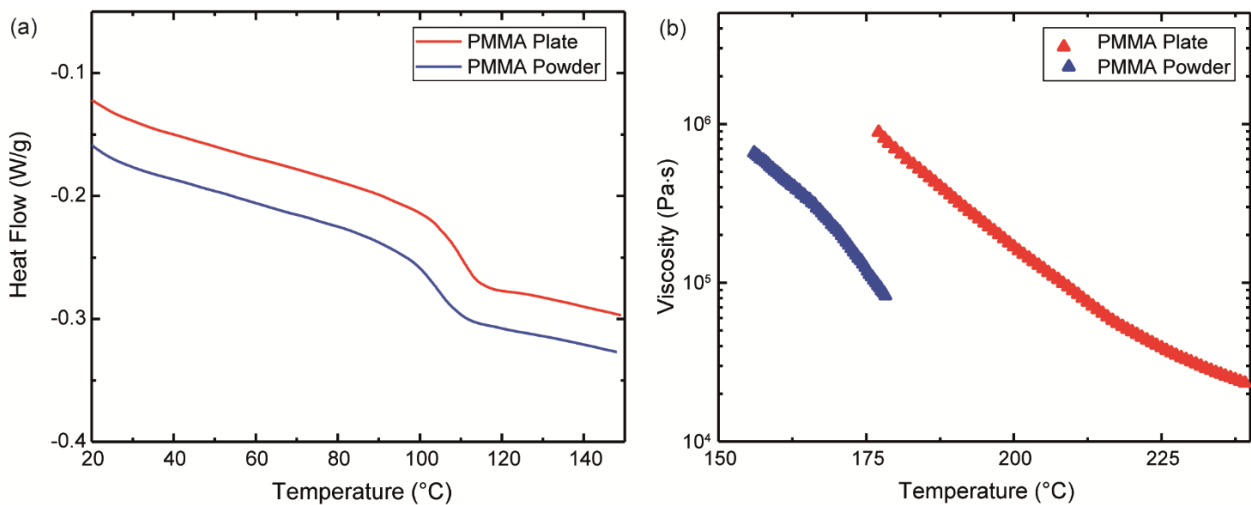
Figure 4-28 (a) DSC curves and (b) viscosity curves for the PMMA plate and PMMA powder.

4.3.3 Thermal drawing and ultimate feature size

The new preforms were produced by first hot pressing the PMMA powder in metallic molds in order to form plates. Then, Au-MG ribbons were inserted between two plates and the structure was consolidated again in a hot press. Furthermore, a lower drawing temperature could be set in comparison to the PMMA plates. It enabled us to successfully bypass crystallization and draw fibers containing continuous ribbons (see Figure 4-29(a)). The Au-MG still turned out to be more prone to break-up inside the fibers. It occurs when the temperature is too high and when the draw down ratio reaches around 18 ($v_{feed} = 1\ mm\ min^{-1}$ and $v_{draw} = 330\ mm\ min^{-1}$). We assume that the break up occurs either at the onset of crystallization, or when the drawing stress becomes too high due to the high viscosity of the Au-MG during the draw. Furthermore its lower resistance to crystallization makes Au-MG unsuitable for the iterative drawing procedure. Hence, the ultimate thickness obtained in this thesis was $\sim 750\ nm$ as shown in Figure 4-29(b).
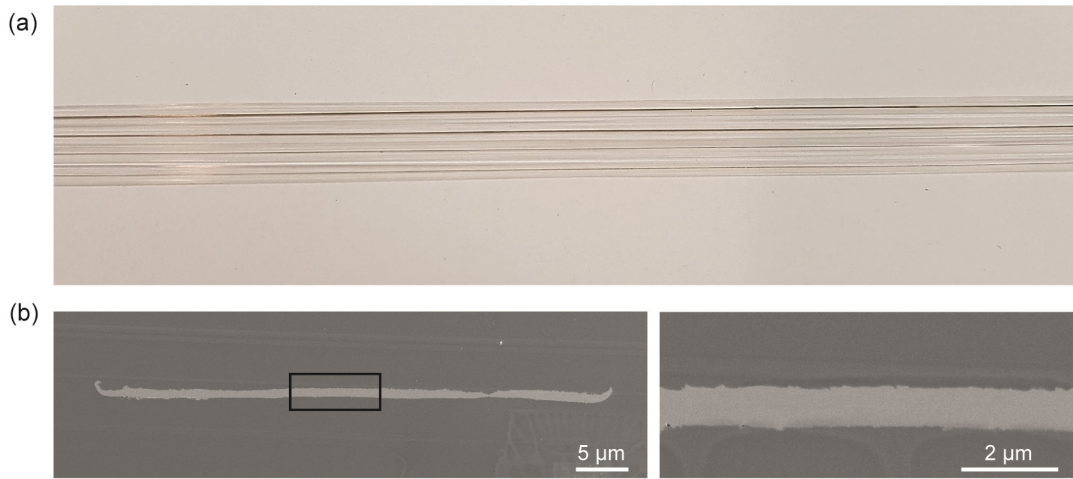
Figure 4-29 Thermal drawing of Au-MG ribbons: (a) Photographs of continuous fibers (b) SEM cross-sectional micrographs of the thinnest Au-MG ribbon. Right: zoom-in micrograph

In order to study the influence of thermal drawing on the crystallization of the Au-MG ribbon, further characterizations were performed. First, Figure 4-30 shows the XRD pattern recorded on the once drawn Au-MG ribbon. We can see that after one draw, the pattern consists of a broad bump with no obvious sharp peak, which is characteristic for amorphous materials. Nevertheless, the sensitivity in XRD is limited and we cannot exclude the presence of few crystals dispersed in the amorphous matrix.
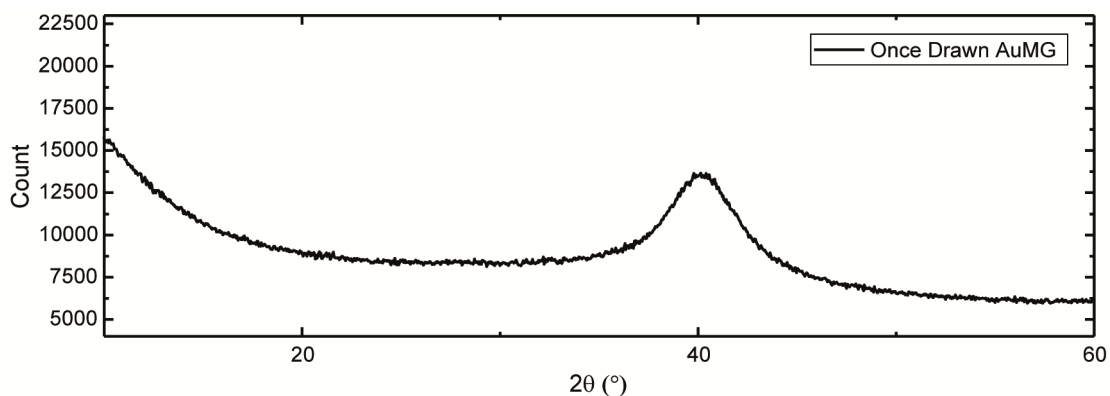
Figure 4-30 XRD pattern of a once drawn Au-MG ribbon.

Secondly, TEM analyses were performed on the Au-MG ribbon. Thin slices of Au-MG were cut from the fiber cross-section with an ultramicrotome and deposited on a TEM grid. The difference in mechanical properties and lack of adhesion between both materials, made the cutting of sub-80 nm slices hard and variable. The SAED shows a halo ring pattern characteristic of amorphous materials, as well as some bright spots arising from reflection from small nanocrystals as shown in Figure 4-31(a). The presence of nanocrystals is confirmed by HRTEM images close to the edge of the ribbons (Figure 4-31(b)). In the central part of the ribbon, no nanocrystal can be observed probably due to the too large thickness of the MG ribbon which prevents us to detect such small signal. This result confirms again the importance of finding the appropriate cladding material to be able to draw the fiber in the small temperature-time windows where the viscosity is low enough to deform the ribbon while still preventing fast crystal nucleation.
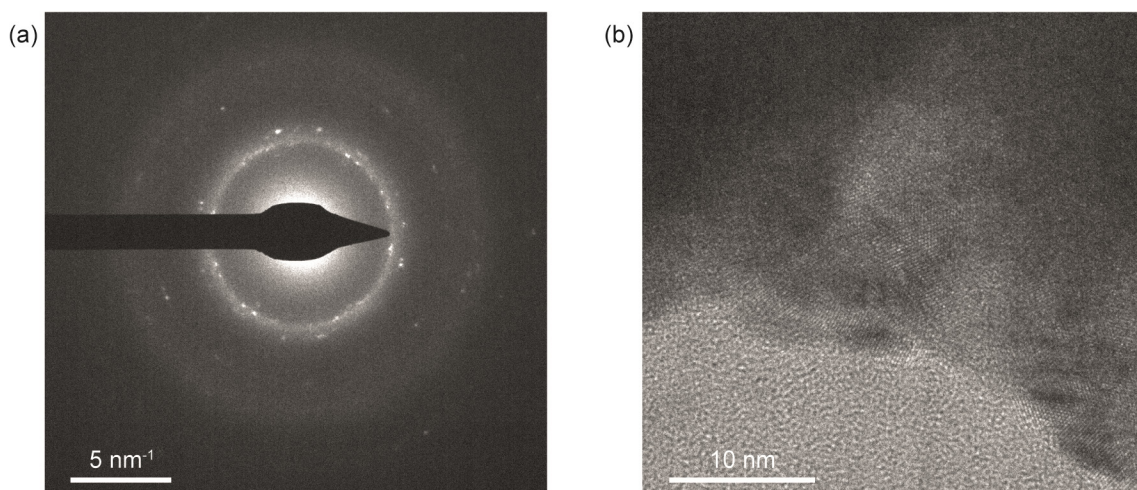
Figure 4-31 TEM characterization of the drawn Au-MG ribbon: (a) SAED pattern. (b) High-Resolution TEM image close to the edge.

4.4 Summary and conclusion

In summary, we demonstrated the compatibility of the thermal drawing technique with bulk metallic glasses with appropriate thermo-mechanical properties and crystallization kinetics. We first investigated the thermal drawing capability of $Pt_{57.5}Cu_{14.7}Ni_{5.3}P_{22.5}$ BMG and showed fibers with a wide variety of architectures. We demonstrated that overcoming crystallization-induced and capillary-induced break-up enabled the mass production of continuous MG fibers with arbitrary cross-sections. A fundamental study of the crystallization kinetics of nanoscale Pt-MG ribbons via

in situ heating TEM revealed a size and/or deformation-dependent break-up of the ribbons. At the microscale, DSC analyses further demonstrated deformation-dependent crystallization kinetics of Pt-MG ribbons. The thermal drawing of Au-MG which has a lower GFA revealed the importance of identifying a cladding polymer with appropriate thermo-mechanical properties in order to prevent crystallization of the MG or mechanical break-up of the fiber. Rheological and thermoanalytical analyses were used to find a compatible cladding, and a sub-micrometer feature size, limited by the onset of crystallization of the MG, was demonstrated.

To conclude, thermal drawing is a simple and scalable method for producing very long, highly uniform and well-ordered micro- and nanoscale MGs. The resulting MGs can be embedded in a flexible polymer fiber matrix, which facilitates their handling and enables direct integration with other functional materials, to interface with external macro-systems or bio-tissues. It opens the way to advanced functional devices requiring highly conductive, small and well-defined electrodes. Some functional fibers integrating Pt-MG electrodes are presented in chapter 5.

4.5 Materials and experimental methods

Materials: The $Pt_{57.5}Cu_{14.7}Ni_{5.3}P_{22.5}$ and $Au_{49}Ag_{5.5}Pd_{2.3}Cu_{26.9}Si_{16.3}$ master alloys were purchased from PXGroup (Switzerland) and processed by Dr. Cao and Dr. Kurtuldu at the Laboratory of Metal Physics and Technology at ETH Zürich. Ribbons were prepared by melt spinning on a Cu wheel with a rim speed of 20 ms^{-1}. The alloy was melted in a quartz tube and then ejected onto the wheel by high-pressure argon. The thickness and width of the ribbons scaled from 60 to 30 μm and 2- to 7 mm respectively. In addition, Pt-MG glassy rods with diameters between 1 and 3 mm were prepared by suction casting in an arc melter.

0.25'' thick PEI plates and rods of diameters between 0.375'' and 1'' were purchased from Boedeker (ULTEM 1000). The plates were cut into rectangular preforms of 24 x 15 mm. The PEI films of thicknesses 25, 50 and 250 μm were bought from Goodfellow (ULTEM). Poly(methyl methacrylate) (PMMA) plates were purchased from Evonik Röhm GmbH, the 50 μm thick films from Goodfellow (Impact modified) and the powder from Sigma Aldrich (average MW~120,000 by GPC, 182230).

Preform making: The preform making procedures are described in section 4.2.2. The rectangular PEI/Pt-MG preforms were consolidated in a hot press (Maschinenfabrik Herbert Meyer GmbH) for 30 min at 240 °C and the cylindrical ones in a consolidation oven (France Etuves) also at ~240 °C. PMMA plates were made by hot pressing the PMMA powder in metallic molds at 205 °C for 30 min under vacuum (Lauffer Pressen UVL 5.0). The PMMA/Au-MG preforms were consolidated at ~130 °C during 20 min.

Thermal drawing: The fibers were drawn in a custom-made drawing tower with three heating zones. For the PEI/Pt-MG fibers, the set temperatures were around 85 °C, 210 °C and 130 °C, the feeding speed was usually 1 $mm\ min^{-1}$ and the drawing speed was varied between 30 and 900 $mm\ min^{-1}$. The PMMA/Au-MG fibers were drawn at set temperatures of around 150 °C, 230-240 °C and 70 °C with a feeding speed of 1 $mm\ min^{-1}$ and drawing speed between 50 and 330 $mm\ min^{-1}$. Note that the real temperatures inside the tower are significantly lower and that the temperature was adjusted depending on the tension measured during the draw.

Differential Scanning Calorimetry: DSC measurements of PEI and $Pt_{57.5}Cu_{14.7}Ni_{5.3}P_{22.5}$ were performed using a Mettler-Toledo DSC 1/700 (ETHZ) under 30 $mL\ min^{-1}$ Ar flow at a rate of 10 $°C\ min^{-1}$. The specimens with a mass between 5 and 50 mg were cut from a glassy rod. DSC measurements of the PMMAs were performed with a DSC Q100 TA under at a rate of 10 $°C\ min^{-1}$. The measurements of the Pt-MG ribbons for the crystallization kinetics study were performed on a DSC Q100 TA at a constant temperature of 255 or 260 $°C$. Samples were prepared by extracting the ribbons from the fibers either mechanically or by etching with acetone and cutting the ribbons in small pieces to obtain 3-5 mg.

Optical Microscopy: Images were taken using a Leica DM 2700M optical microscope.

SEM: The SEM samples for cross-section imaging were prepared by mechanical cutting using ultramicrotomy (diamond blade). Hollow core fibers were filled with epoxy to facilitate the cutting. The SEM samples were then coated with a 10 nm carbon film. All the other samples were prepared by dissolving the cladding with NMP or acetone for PEI and PMMA respectively. The SEM images were taken with a Zeiss Merlin field emission SEM (Zeiss, Göttingen, Germany) equipped with a GEMINI II column operating at 1 or 3 kV with a probe current of 100 or 150 pA. EBSD images were taken under a 15 kV voltage and probe current of 3 nA with a 4 quadrant backscattered electron (BSE) detector.

TEM: Depending on the thickness of the drawn MG ribbon, two methods were used to prepare the TEM samples. Cross-sectional cuts of thick ribbons were prepared using ultramicrotomy and transferred on a carbon/Cu grid support (300 mesh). Thinner ribbons were prepared by dissolving the PEI cladding using NMP. The free-standing MG ribbons were then cleaned with ethanol before being transferred on the carbon/Cu grid. The TEM images and SAED patterns were taken using a Talos F200X operating at 200 kV.

In situ TEM: All the TEM specimens were prepared by dissolving the PEI cladding using NMP followed by ethanol cleaning before being transferred on MEMS chips (DENSsolutions, through hole). After monitoring their resistance, the chips were inserted in the TEM. All data were acquired in a ThermoScientific Titan Themis operated at 300 kV. The samples were first monitored in high-angle annular dark field (HAADF) STEM/EELS mode for t/λ (thickness divided by the mean free path) mapping of the area of interest. The absolute thicknesses were calculated after relating the mean free path with a thickness measured from a 120 nm MG ribbon measured by SEM. Bright-field diffraction imaging was then optimized for all samples at a dose of 2 nA and the selected area probed in each case was 500 nm in diameter. Diffraction patterns were acquired in series with a frame size of 1kx1k for 0.98 s dwell time each. The imaging was synchronized with a chosen temperature ramp profile (heated to 170 $°C$ within 0.5 s from room temperature followed by a 40 $°C\ min^{-1}$ ramp from 170 to 500 $°C$) for the crystallization temperature measurements and a constant temperature hold at 260 $°C$ for the crystallization time measurements.

Quantification of T_x and t_c of nanoscale MG ribbons: The quantification of T_x and t_c of the MG ribbons with diameters of 45, 95 and 105 nm was carried out based on the contrast change in the SAED patterns. In order to better measure the contrast change of the diffuse rings in the SAED patterns, polar transformation was applied to the patterns. Thus, the curved, broad sports in the diffusive rings indicating crystallization appeared as straight, broad lines after transformation. In the polar transformed patterns, two rectangular regions were selected to quantify the T_x: one on the straight, broad line and the other one on the region just below the broad line at the background (the size of both regions

was the same). The sum of the intensity of each pixel from the two regions were performed for all the SAED patterns as a function of imaging time. The relative intensity for each pattern was calculated based on the equation:

$$I_r = \frac{I_{spot} - I_{background}}{I_{background}}$$

Where I_{spot} and $I_{background}$ are the total intensity of the spot and background, respectively. At the onset of crystallization, the relative intensity increases abruptly form a constant background. The T_x was defined at the intercept of the constant background with the linear fit to the increasing relative intensity. To quantify the t_c, every ten SAED frames was treated as one frame by averaging the contrast in order to reduce the noise of each frame. The same polar transformation and relative intensity calculation was applied to each frame. The t_c was defined at the intercept of the constant background and the linear fit to the increasing relative intensity.

Thermo-mechanical characterization: DMA experiments were performed on a Q800 DMA (TA Instruments) with the film tension mode. The deformation tests were performed with a heating ramp of $3\,°C\ min^{-1}$ from 80 to 160 $°C$ and applying a constant stress of 0.15 MPa. The viscoelastic behavior was characterized at a frequency of 1 Hz and strain of 0.02 % with a $3\,°C\ min^{-1}$ heating ramp.

GPC: 3 mg of powder-like samples were prepared from the three types of PMMA by cutting or mechanical grinding. The samples were then dissolved in Tetrahydrofuran (THF). The measurements were performed with an Agilent 1260 Infinity chromatographer.

Rheometer: The rheological measurements were performed on a TA Instrument AR 2000ex (USA) rheometer. The tests were performed with a shear rate of 2.5 s^{-1}. Parallel aluminum plates of 25 mm diameter with a Peltier Plate heating system were employed.

XRD: The Pt-MG samples were obtained by mechanically extracting the ribbons of the fiber or by selectively dissolving the PEI with dichloromethane. Acetone was used to dissolve the PMMA cladding to collect the Au-MG ribbons. The room temperature X-ray diffraction measurements were performed on an Empyrean (Theta-Theta, 240 mm) diffractometer (Panalytical) using Cu Kα radiation. It is equipped with a PIXcel-1D detector, Bragg-Brentano beam optics and parallel beam optics, and a spinning stage. The BMG ribbons were deposited on zero background sample holders. The in-situ heating XRD measurements were performed on an X'Pert diffractometer (Panalytical) using Cu Kα radiation and equipped with a 1S X'Celerator detector and a heating chamber HTK1200 (Anton Parr).

5 Functional fibers integrating Pt-MG electrodes

We conclude this thesis by presenting novel fiber devices that result from our finding of new materials and understanding of the thermal drawing process. The capacity to co-draw materials with different functional properties and to reach micrometer or sub-micrometer feature sizes is known to significantly extend the range of applications of fiber devices [5], [6]. In particular, in the context of implants such as neural probes, the possibility to reach extremely small electrode dimensions and precise arrangement in a fiber geometry, allowed by the drawn BMGs, is a compelling answer to the current need for probes with minimal footprints, flexibility and robustness. The multimodal ability allows minimally invasive surgeries and therefore can be used for long-term *in vivo* applications. Because of the polymer cladding, the probes are flexible and maintain their functionality upon bending. Furthermore, reduced tissue responses compared to insulated steel microwires have been reported [9], [150].

In addition to their unique processing capabilities, another remarkable property of some BMGs is their excellent stability. BMGs retain a completely amorphous structure upon cooling, free of grain boundaries and crystalline defects, which enhance their corrosion resistance [151]–[153]. Furthermore, $Pt_{57.5}Cu_{14.7}Ni_{5.3}P_{22.5}$ has shown high durability and electrocatalytic activity in fuel cells [154]–[156] as well as good biocompatibility [157]. By combining the versatility of the thermal drawing technique and the high stability of the Pt-MG, novel electronic devices can be developed. In the next part, we present two types of functional fibers acting respectively as neural probes and electrochemical sensors.

5.1 Stimulation and recording electrodes in neural probes

Multifunctional fiber probes integrating functions such as optical stimulation, electrical neural recording and controlled chemical delivery have been processed with thermal drawing. Canales et al. demonstrated optogenetic stimulation and neural recording in freely moving mice with all-polymer fibers and reported that the fibers remained functional for up to two months after implantation [9]. Nevertheless, due to the limited conductivity of the conductive composite, the fibers had a diameter superior to $400\ \mu m$ which may induce large tissue damages. The integration of tin electrodes allowed the reduction of the fiber diameter while keeping good recording capability. On the other hand, Park et al. and Guo et al. developed conductive composites with higher electrical conductivity by integrating graphite and carbon nanofibers, respectively [150], [158]. The latter enables the reduction of the electrode dimensions while maintaining the quality of the recording and therefore minimize the tissue response. Despite these advances, a fiber capable of electrical stimulation has not been reported yet. Indeed, the high resistance of the composite electrodes and the limited stability of tin electrodes when subjected to electrical pulses restrict the use of these electrodes to only recording.

The Pt-MG can resolve this limitation thanks to its high conductivity ($\sim 10^6 \ S \ m^{-1}$) and structural homogeneity, which reduces its susceptibility to chemical attack. In the next part, we demonstrate fiber probes integrating multiple Pt-MG wires for electrical stimulation and recording. First, we characterize the electrical and electrochemical properties of Pt-MG electrodes *in vitro*. Then, we present two different designs of multifunctional fibers which can be used for stimulation and recording, as well as drug delivery for the second fiber. The results from *in vivo* tests performed in rats are shown and analyzed in the last part.

The design and processing of these fibers were done in collaboration with Dr. Wei Yan, the electrical characterization with Dr. G. Schiavone at the Laboratory for Soft Bioelectronic Interfaces and the *in vivo* experiments were performed by Dr. N. D. James at the Center for Neuroprosthetics and Brain Mind Institute. The main results have been published in:

W. Yan, I. Richard, G. Kurtuldu, N.D. James, G. Schiavone, J.W. Squair, T. Nguyen-Dang, T. Das Gupta, Y. Qu, J.D. Cao, R. Ignatans, S.P. Lacour, V. Tileli, G. Courtine, J.F. Löffler, and F. Sorin "Structured nanoscale metallic glass fibres with extreme aspect ratios", *Nat. Nanotechnol*. 15, p. 875-882, August 2020, doi : 10.1038/s41565-020-0747-9

5.1.1   *In vitro* characterization of the electrodes

In terms of electrical properties, the electrodes should have a low impedance and a safe reversible charge injection to enable a low signal-to-noise ratio for recording and limit the electrode degradation during stimulation [159]. These properties are usually characterized using a 3 electrode systems in a buffer solution. We performed impedance spectroscopy, cyclic voltammetry (CV) and voltage transient (VT) measurements.

The impedance measurements of two $30 \ \mu m$ diameter MG electrodes are shown in Figure 5-1(a) with frequencies spanning from $1 \ Hz$ to $1 \ MHz$. The Bode plot of impedance versus frequency is similar to the one reported for platinum electrodes [160]. At high frequency the response depends mainly on the electrolyte resistance, and possibly contact resistance, as suggested by the phase shift approaching zero (Figure 5-1(b)). When decreasing the frequency, a higher impedance is measured due to the presence of an electrochemical double layer at the interface between the electrode and the electrolyte which acts as a capacitor. Despite the small variability between the two measurements, which must come from differences in electrode dimension or roughness at the fiber tip, we can see that at $1 \ kHz$, the impedance is lower than $50 \ k\Omega$. The latter is one order of magnitude smaller than the impedance reported for cPE and in the same range than Sn electrodes [9], [150], [161]. It confirms that such electrodes should be suitable for neuron activity recording and that the electrode diameter could be even slightly decreased in order to make a denser array of electrodes or a thinner overall fiber.
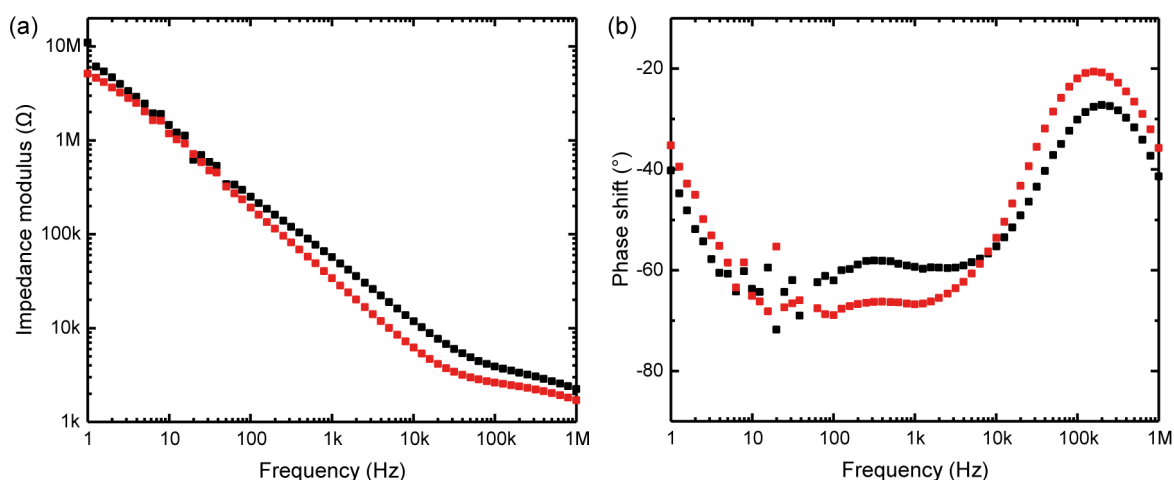
Figure 5-1 Frequency dependent impedance (a) and phase angle (b) of two 30 μm Pt-MG electrodes (black and red) measured *in vitro*.

Cyclic voltammetry gives an insight on the electrochemical reaction occurring in the targeted potential windows, the reversibility of these reactions and the stability of the electrodes. In order to be able to compare the stability of the Pt-MG with conventional electrode materials in the thermal drawing technique, we performed CV tests in phosphate-buffered saline solution (PBS) on crystalline metal (BiSn, Sn), composite (conductive polycarbonate (cPC) and polyethylene (cPE)) and Pt-MG electrodes as shown in Figure 5-2.

For the Pt-MG electrode, the potential was swept between -0.6 V and 0.8 V versus Ag/AgCl, which corresponds to the water windows of this material, to prevent water electrolysis. During the first cycle, a rectangular shape is observed due to the capacitive behavior of the electrochemical double layer (Figure 5-2(a)). After few hundred cycles, a small oxidation peak (around 0.3 V) and deeper reduction peak (around -0.1 V) appear. Carmo et al. analyzed the surface of Pt-BMG nanowires after CV cycling and reported a decrease in Cu content during the first hundreds of cycles [154]. The latter increases the Pt surface area and can enhance the electrochemical activity. The peaks can therefore be attributed to the oxidation and reduction of Pt as observed in pure Pt electrodes [159], [160]. After a few hundreds of cycles the CV response stabilizes and remains constant for up to 12'000 cycles which reveals the long-term stability of the electrode.
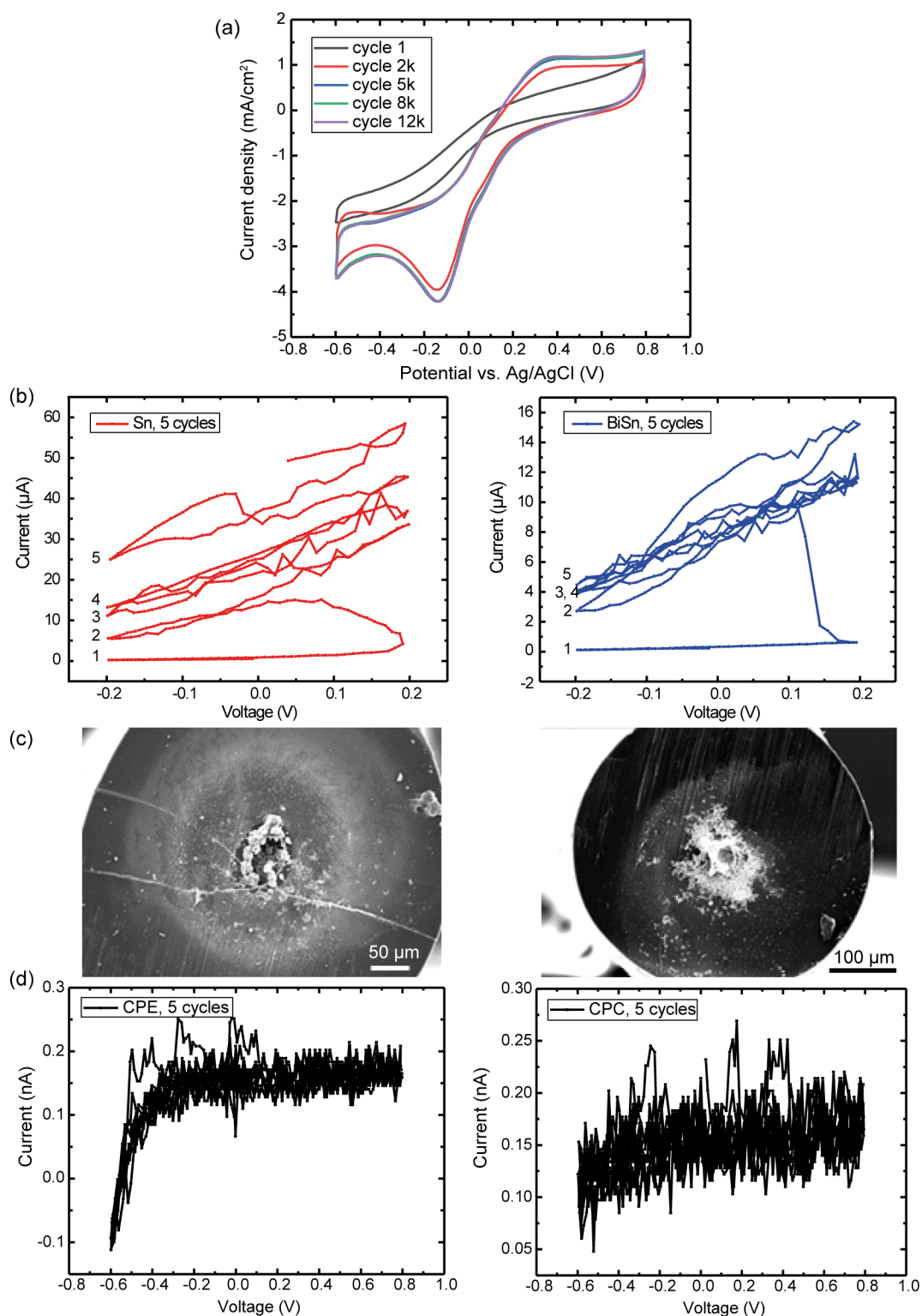
Figure 5-2 CV characterization of thermally drawable electrodes: (a) CV of $30\ \mu m$ Pt-MG electrode between -0.6 to 0.8. (b) CV of Sn and BiSn electrodes, respectively, between -0.2 and 0.2 V. (c) SEM micrographs of the Sn and BiSn electrodes, respectively, after 5 CV cycles. (d) CV of cPE and cPC electrodes between -0.6 to 0.8 V. The scan rate was 100 $mV s^{-1}$ for all the measurements.

The crystalline electrodes do not reach a stable state even when scanning a smaller potential window (-0.2 to 0.2 V versus Ag/AgCl) as shown in Figure 5-2(b). SEM analyses reveals that the electrode surface is considerably damaged after 5 cycles which explains the unstable measurements (Figure 5-2(c)). On the other hand, no measurable current is

obtained for the polymer composite electrodes probably due to the large impedance of the $30\ \mu m$ diameter electrodes as reported by Park et al. [150] (Figure 5-2(d)).

Finally, we carried out voltage transient experiments to compare the stability of crystalline metal and Pt-MG electrodes subjected to electrical pulses. We used similar parameter than for the final *in vivo* experiments: biphasic square pulses with $I_{max} = 50\ \mu A$, pulse width = 300 μs and a frequency of 40 Hz, as schematized in Figure 5-3(a). We observed that the response was frequency dependent and that the signal stabilized only after a certain amount of pulses. Furthermore, the oscilloscope did not have the ability to save all the curves. Therefore we manually saved the first cycle of each set of pulses, each set having a fixed number of pulses in order to record the 1st, 100th, 1000th cycles for example. The pulses we present in Figure 5-3 are therefore not representative of the stable state, but can be used to determine if degradation of the electrode occurred. We can see that the VT curves of Sn and BiSn electrodes rapidly lose stability which suggests that some degradation of the electrode occurs (Figure 5-3(b) and (c)). In contrast, the Pt-MG electrode exhibits a stable response even after 100k pulses (Figure 5-3(d)). Even though *in vitro* conditions are different from *in vivo*, we can conclude that the Pt-MG have a better stability than the crystalline metals and could potentially be used for *in vivo* stimulation.
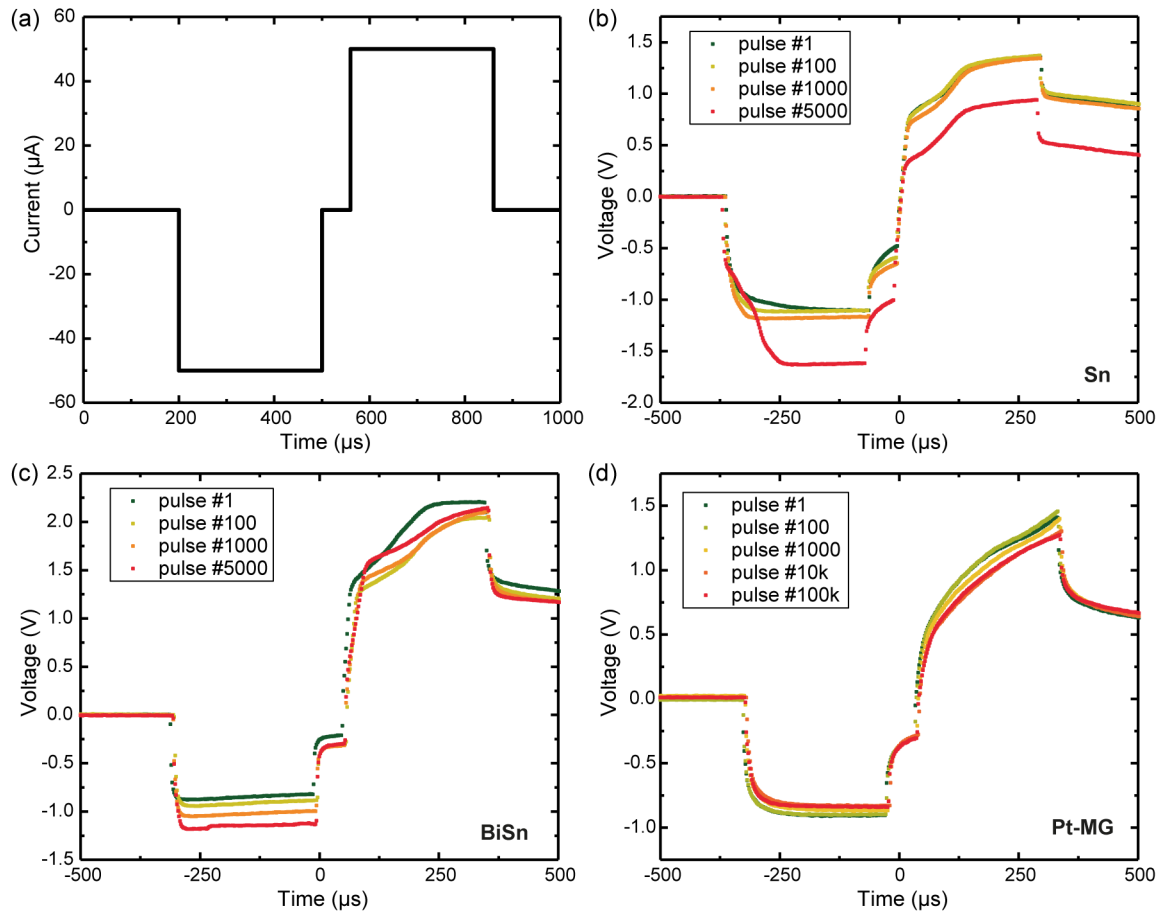
Figure 5-3 Voltage transient experiments: (a) Schematic of the biphasic pulses. (b) VT curves of an in-fiber Sn electrode for 5000 pulses. (c) VT curves of an in-fiber BiSn electrode for 5000 pulses. (d) VT curves of a Pt-MG electrode for 100k pulses.

5.1.2 Probe design and thermal drawing

We designed two types of fibers to analyze their *in vivo* performance. First, we thermally drew a fiber containing an array of Pt-MG electrodes to stimulate and record neural activities in the deep brain of rats and in particular assess the long-term stability of the electrodes. Secondly, in order to demonstrate the adaptability and multi-functional potential of the fiber probes, we designed a shorter probe containing two MG electrodes and a microfluidic channel to allow localized pharmacological manipulation (chemotrode). We targeted electrode diameters of $\sim30~\mu m$, corresponding to a surface area of $\sim700~\mu m^2$. They fulfill therefore both the requirements for single-unit recording and ease of processing since only two iterative drawings are required to reach these dimensions starting from a $1~mm$ diameter Pt-MG rod. Moreover, a large surface area is preferred for stimulation since it increases the amount of charges that can be injected in a pulse while maintaining the potential within the range where no degradation occur.

An optical micrograph of the cross-section of the fiber designed for stimulation and recording is shown in Figure 5-4(a). The four Pt-MG electrodes had a diameter between 20 and 45 μm. The connections were made by mechanically exposing the electrodes, and contacting them with electrical wires and silver paint. An epoxy coating was added on top in order to strengthen and protect the connections. Furthermore, we manually grinded the cladding of the fiber end to be implanted ($\sim8~mm$ in length) in order to reduce the external diameter to $\sim300~\mu m$ (Figure 5-4(b)). A slanted cut of the fiber tip was made in order to have a small variation in recording and stimulation region, and increase the likelihood to have some electrodes perfectly positioned after the surgery. The cross-section of the chemotrode is shown in Figure 5-4 (c) and contained two Pt-MG electrodes with a diameter of $\sim30~\mu m$ and an empty channel with a diameter of $\sim110~\mu m$. Thanks to the high viscosity of the polymer cladding during thermal drawing, the empty channel can be easily maintained from the preform to the fiber level. A similar procedure than for the first fiber was followed to process the probes.
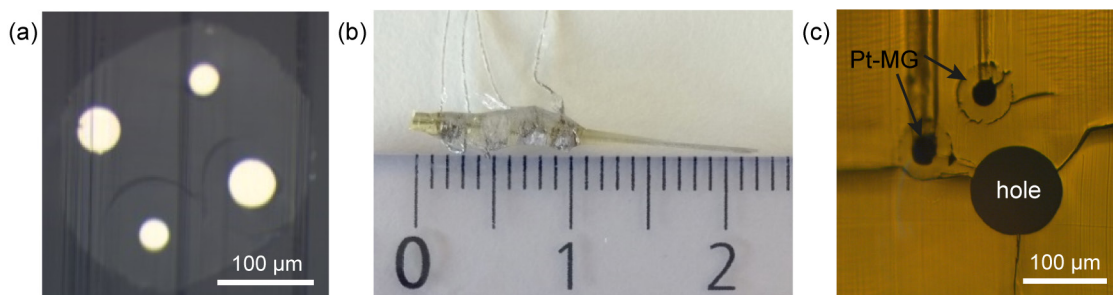
Figure 5-4 Probes. (a) OM micrograph of the stimulating fiber cross-section. (b) Photograph of a fiber probe before implantation with the 4 contacts on one end. (c) OM micrograph of the chemotrode cross-section.

5.1.3 *In vivo* electrochemical characterization of the Pt-MG electrode

Due to the differences of environment in vitro and in vivo such as the temperature, the presence of organic species or of physiological response, electrochemical characterization tests were also performed *in vivo* after fiber implantation. The impedance and cyclic voltammograms of the electrode were recorded following a similar methodology than *in vitro*. However, this time a two-electrode configuration was used where one multi-stranded stainless steel wire (Cooner wire) attached to a skull-fixed screw acted as both counter and reference electrode.

Figure 5-5(a) shows the *in vivo* impedance spectra of two $30\ \mu m$ diameter Pt-MG electrodes. The recorded impedance at $1\ kHz$ are in the range of $92 - 185\ k\Omega$, significantly lower than that of previously reported devices [9], [150]. Furthermore, it is in the same range as during *in vitro* measurements. At high frequency, the impedance modulus is larger *in vivo* due to the increased contribution of the tissue resistance. Figure 5-5(b) shows the CV response *in vivo* which is also comparable to the one recorded *in vitro*. The cathodal charge storage capacity (CSC) can be determined from the time-integral of the negative-current part of the CV curves (grey area in Figure 5-5(b)) and represents the total amount of charge available for a stimulation pulse [159]. We calculated a CSC of about $6\ mC\,cm^{-2}$ for a $30\ \mu m$ diameter MG electrode which is on par with metallic electrodes in other platforms and commercially available probes [159], [162]–[165]. This value could be improved by structuring or roughening the exposed surface of the fiber.
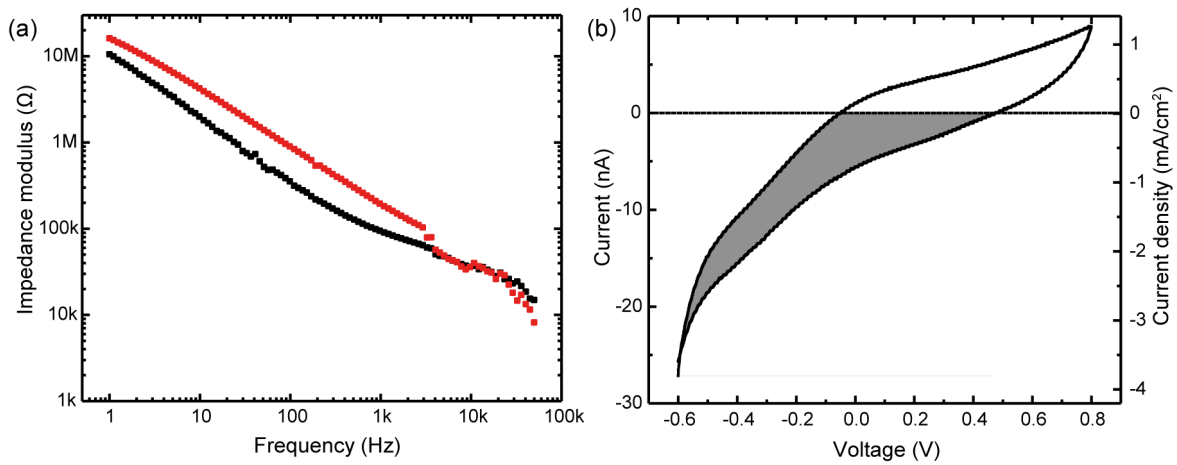
Figure 5-5 *In vivo* characterization of the Pt-MG electrodes: (a) Frequency dependent impedance of two $30\ \mu m$ diameter electrodes. (b) CV curve of a $30\ \mu m$ diameter electrode, with the area in grey used for the calculation of the cathodal CSC.

5.1.4   In vivo fiber probe characterization

In order to assess the functionality and longevity of the fibers, chronic implantation was performed into the pedunculopontine nucleus (PPn) of the mesencephalic locomotor region (MLF) in rats (Figure 5-6(a)). This deeply located structure is involved in the production of locomotion, which allows us to link changes in neuronal activity to clear behavior. Furthermore, the electrical stimulation of the neuronal cell bodies located in this region triggers a forced initiation of locomotion that continues as long as the electrical stimulation is turned on. Therefore, it provides a univocal demonstration of the functionality of the electrodes.

The fibers were implanted in the brain of six rats and stimulation using the implanted fibers was tested weekly for up to 12 weeks post-implantation. In all tested rats, continuous electrical stimulation at $40\ Hz$ in the PPn triggered a stereotypical forced locomotive response (Figure 5-6(b) and (c)). After a reproducible short latency once stimulation was turned on, the left and right hindlimb muscles exhibited alternating bursts of electromyographic (EMG) activity that are typical of walking. Augmenting the intensity of the stimulation resulted in a graded increase in the speed of locomotion (Figure 5-6(d)). These responses were observed consistently in all the rats up to 12 weeks post-implantation. This demonstrates the capability of neural stimulation using metallic glass electrodes.
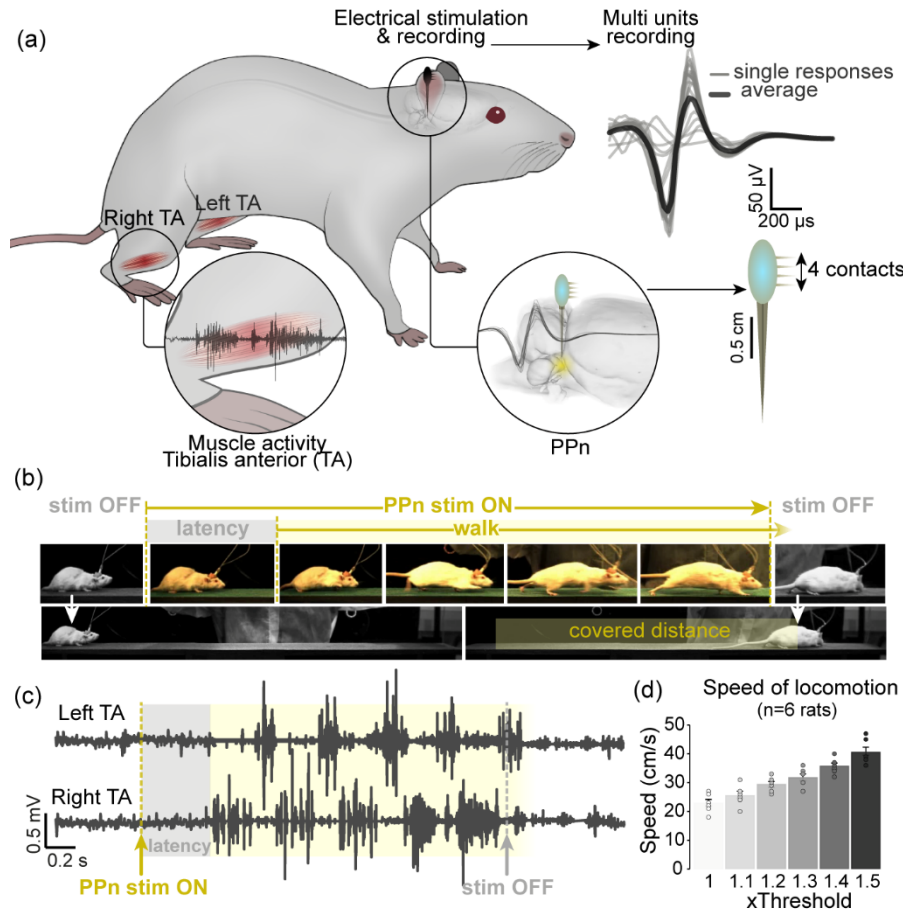
Figure 5-6 Neural stimulation and recording using MG-based fiber probes: (a) Schematic representation of the experimental set-up showing examples of neuronal spiking activity recorded from the PPn at one week post-implantation. (b,c) Stimulation of the PPn using the implanted fiber (b) resulted in a forced locomotion response, (c) associated with alternating electromyographic activity in the left and right hind limbs typical of walking. These findings were repeated in all implanted rats (n=6). (d) Locomotion continued to be evoked in all animals during stimulation at 12 weeks post-implantation, with increasing stimulation intensity generating high speeds of locomotion (n=6, mean ±s.e.m.).

Furthermore, in order to demonstrate the recording potential of these MG electrodes, we performed a detailed quantification of multi-unit spiking activity at one and four weeks post-implantation in two representative animals (Figure 5-7(a)). We found that the neural recordings from the PPn were able to reliably detect a significant increase in neural firing rate between the resting and walking states in awake, freely moving animals. Generally, the ability to record neural activity declined gradually during the weeks that followed, such that between six and eight weeks post-implantation the deterioration in signal-to-noise ratio meant that we could no longer reliably quantify the spiking activity. This degradation is in part due to immune responses of the host brain tissue, including the formation of a reactive gliosis that isolates the electrodes from the neural bodies and the micromotions of the brainstem that can exacerbate these responses. Indeed, post-mortem visualization of the glial fibrillary acidic protein (GFAP), microglia/macrophages (Iba1) and neurons (NeuN) using immunohistochemistry revealed the formation of a reactive gliosis depleted of neurons around the implanted fibers (Figure 5-7(b-d)). The intensity of such tissue response is comparable to previously reported work [9], [150].
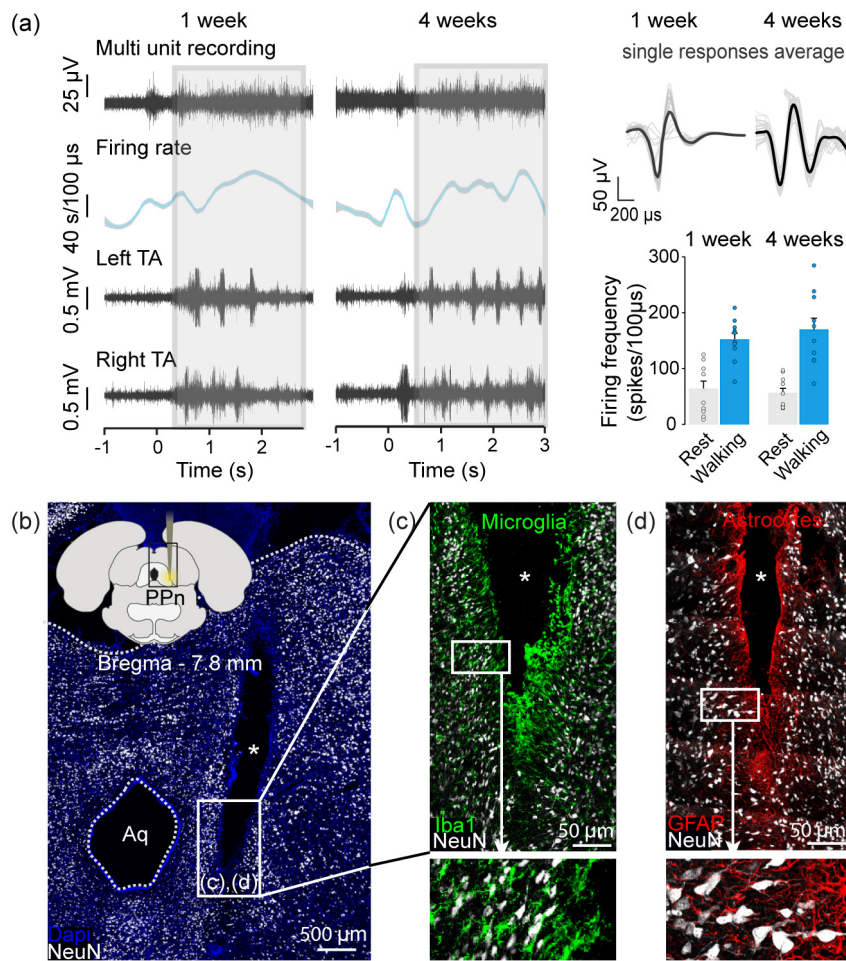
Figure 5-7 Neural stimulation and recording using MG-based fiber probes: (a) Representative traces of multi-unit activity recorded at one and four weeks post-implantation illustrating the increase in firing rate when rats are walking compared to when at rest. A period of walking is highlighted by the grey box overlaying the raw traces. Quantification of firing rates reveals that this increase is statistically significant at both one and four weeks post-implantation (P < 0.001 using a linear mixed model with timepoint and condition as fixed effects and the animal as random effect). For each animal (n = 2) and at each timepoint (one week and four weeks post-injury), the mean spike rate was calculated for a total of n = 5 trials for both rest and walking (40 trials total). Error bars represent standard error of the mean. (b)-(d), Representative immunohistochemistry images taken from 12-weeks post-implantation tissue highlighting the inflammatory processes occurring at the electrode implantation site (b), with microglia/macrophages (Iba1, red; (c)) and astrocytes (GFAP, green; (d)) being recruited to the site and potentially preventing the recording of activity from nearby neurons. (NeuN, white; Dapi (a counterstain for all nuclei), blue). Aq, cerebral aqueduct. A similar inflammatory profile was observed in all animals (n = 6).

For the second test, two chemotrode fibers were implanted into the hindlimb and forelimb regions of the motor cortex of the same rat (Figure 5-8(a)). Stimulation in these two regions can evoke responses in the tibialis anterior and the biceps, respectively, after a short latent period. The delivery of a train of electrical stimulation in the forelimb motor cortex evoked a large EMG response in the forelimb muscles but not in the hindlimb muscles. Inversely, stimulation of the hindlimb motor cortex only evoked responses in hindlimb muscles (Figure 5-8(b), left). We then injected 10 μL of gamma-aminobutyric acid (GABA) agonist muscimol through the chemotrode located in the hindlimb motor cortex. The resulting inhibition of local neural circuits entirely abolished the responses to hindlimb motor cortex stimulation, while responses evoked by the forelimb motor cortex remained unaffected (Figure 5-8(b), middle). After washout of the muscimol, the responses of the hindlimb muscles is recovered (Figure 5-8(b), right). The quantification of the mean

peak-to-peak amplitudes evoked during each condition shown in Figure 5-8(c), clearly indicates the ability to achieve precise local drug delivery with the chemotrode and confirms the stimulating and recording capability of the MG electrodes.
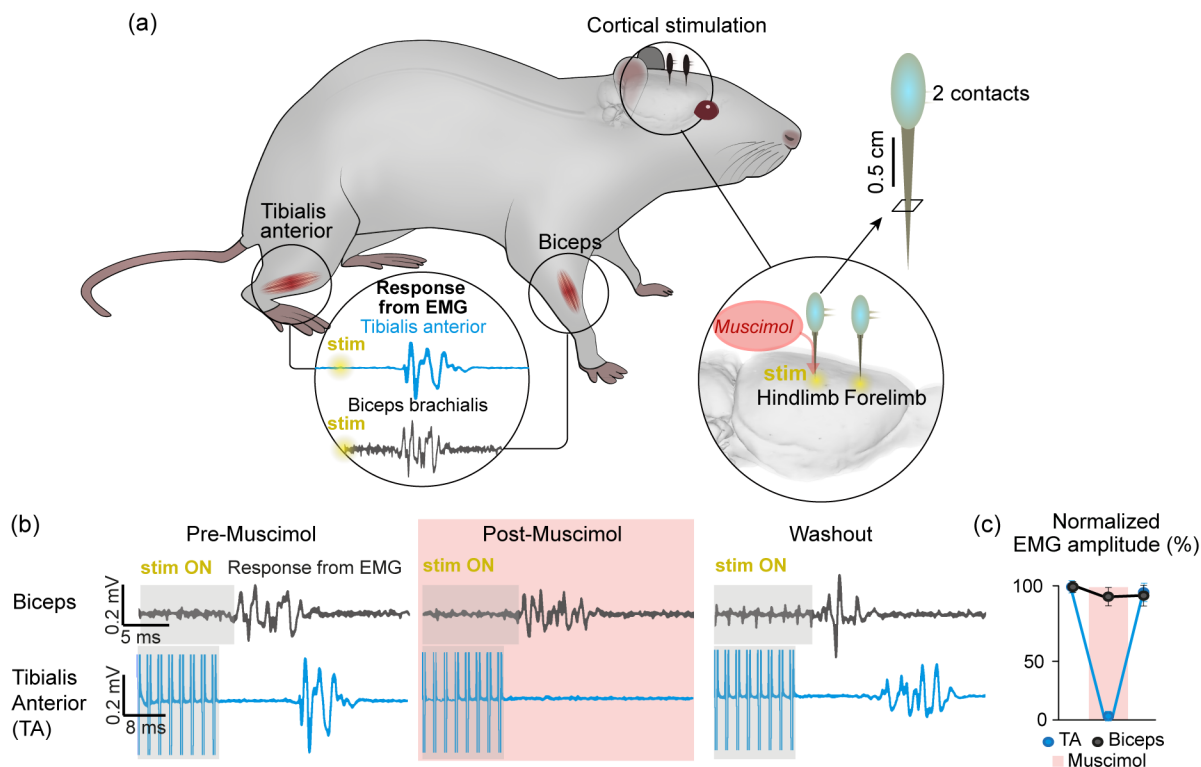
Figure 5-8 Localized neural inactivation using MG based fiber probes incorporating a chemotrode: (a) Schematic representation of the experimental set-up showing the fiber implantation regions. (b) Representative traces of evoked EMG responses recorded from the biceps brachii (forelimb motor cortex stimulation) and tibialis anterior (hindlimb motor cortex stimulation) before, during and after injection of muscimol in the hindlimb motor cortex. (c) Quantification of mean peak to peak amplitudes of 20 EMG responses evoked during each condition.

5.1.5   Materials and experimental methods

Materials: PEI rods were purchased from Boedeker, conductive polycarbonate (cPC) and polyethylene (cPE) from Goodfellow and $Bi_{58}Sn_{42}$ and Sn ribbons from Indium Corporation of America. The $Pt_{57.5}Cu_{14.7}Ni_{5.3}P_{22.5}$ master alloys were purchased from PXGroup (Switzerland) and suction casted into 1 mm rods in an arc melter by Dr. Kurtuldu at the Laboratory of Metal Physics and Technology at ETH Zürich.

Probe making: The preforms used for the CV characterization were prepared by drilling a hole in PEI rods of the same dimensions than the cPC, cPE, BiSn or Sn elements. The preforms were then thermally drawn with ddr enabling to reach similar electrode surface area with the Pt-MG ones. The precursor fiber for the neural probes was obtained by thermally drawing a 1 mm Pt-rod. The probe preforms were fabricated by drilling, in a PEI rod, holes of 1 mm diameter to insert the precursor fibers and 1.5 mm diameter for the hollow channel. The fibers were drawn at set temperatures of 210-335-140 $°C$ with ddr of around 15. The diameter of the implanted part of the probe was reduce to 300 μm by polishing with sandpapers. The electrical connections were made by removing the cladding with a razor blade to expose the

electrodes and contacting them with conductive wires with some silver paint. Epoxy is then applied on the contact to protect them.

Electrochemical impedance spectroscopy measurements: The *in vitro* measurements were performed in phosphate-buffered saline solution (Gibco PBS, pH 7.4, 1X). The fiber was immersed in the solution together with a counter (platinum rod) and reference (Metrohm, El. Ag/AgCl DJ RN SC: KCl) electrode. The measurements were taken in this three-electrode configuration using a Gamry 600 potentiostat at room temperature. The EIS spectra were acquired by injecting sinewave signals of 0.1 V amplitude at the 1 $Hz - 1\ MHz$ frequency range, with 10 data points per decade. A similar methodology was followed for the *in vivo* measurements but using a two-electrode configuration, where one multi-stranded stainless steel wire (Connere Wire) attached to a skull-fixed screw acts as both counter and reference electrode. The spectra were acquired by injecting sinewave signals of 0.1 V amplitude at the 1 $Hz - 50\ kHz$ frequency range, with 21 data points per decade.

Cyclic voltammetry measurements: *In vitro* CV measurements were performed in PBS at room temperature in a three-electrode configuration as for the EIS measurements. The spectra were recorded with a scan rate of 100 mVs^{-1} between voltages of -0.6 and 0.8 V for the Pt-MG and composite electrodes, and -0.2 and 0.2 V for the other metallic electrodes. *In vivo* measurements were performed using a two-electrode configuration, as described for the EIS measurements. The spectra were recorded with a scan rate of 100 mVs^{-1} between -0.6 and 0.8 V after several initial unstable cycles.

Voltage transient measurements: VT measurements were performed in the same three-electrode setup injecting constant current pulsing. Constant current, symmetric, biphasic, charge-balanced, cathodic-first pulses were applied between the electrode under test and the counter with an A-M Systems 2100 Isolated Pulse Stimulator (300 μs per phase-pulse width, 1 s inter-pulse period, 50 μA amplitude), while measuring the voltage across the working and reference electrodes with an oscilloscope. The VT cycles for all electrodes were performed using the abovementioned pulses at 40 Hz, which is the same frequency used for in vivo stimulation.

Fiber implantation: Adult female Lewis rats (Janvier, France) were group-housed, maintained on a 12 h light/drawk cycle and given access to food and water *ad libitum*. For fiber implantation, rats were surgically anaesthetized using 1.5-2.5% gaseous isofluorane in medical oxygen. The skull was exposed and a small hole was drilled over the appropriate area of the brain. The fiber was then implanted into the forelimb motor cortex, hindlimb motor cortex or the PPn of the mesencephalic locomotor region (MLR) using coordinates taken from Paxinos and Watson (2004): +2 mm from Bregma, anterior-posterior (AP); +2.5 mm from the midline, medio-lateral (ML); and a depth of -1.8 mm dorso-ventral (DV) for the forelimb motor cortex; -1.75 mm AP, + 2.25 mm ML, -1.8 mm DV for the hindlimb motor cortex; -8 mm AP, +2 mm ML and -6.5 mm DV for the PPn. Ground and reference wires were attached to skull-fixed screws and the implants was then permanently stabilized using dental cement. The animals were provided with suitable analgesia post-surgery (buprenorphine, 0.01 $mg\ kg^{-1}$ s.c.) and antibiotics (amoxicillin) were provided in drinking water for one week to prevent infection due to implantation.

Stimulation and PPn recordings using the implanted fibers: Stimulation and recording sessions were performed on a weekly basis for up to 12 weeks post-implantation. During stimulation sessions, the behavioral response to PPn stimulation was tested (40 Hz train of 200 μs duration biphasic pulses, with an amplitude of 50-250 μA; A-M Systems isolated pulse stimulator). The animals were placed on a one-meter long runway and stimulation was initiated, resulting in forced locomotor activity (typically after 1-2 seconds of stimulation), which was halted as soon as stimulation was turned off. Recording sessions during spontaneous locomotor behavior involved the recording of extracellular voltage signals, which were pre-amplified, digitalized, filtered (high pass 0.3 kHz, low pass 5 kHz), sampled at 24 kHz, and stored using a BioAmp processor (Tucker-Davis Technologies, USA). The channels average was subtracted offline from each trace to reject common mode noise. Recordings in which the signal exceeded two standard deviations of background noise were deemed to be of acceptable quality for further analysis. The PPn multi-unit activity consisted of all field-potential stochastic events that crossed a manually set threshold value for each channel. The sum spike count was then derived across channels and binned every 100 μs. To compare spike rates during rest and during waling, we manually annotated 2 s bins as either 'rest' or 'walking' based on alternating EMG activity. For each animal (n=2) and at each time-point (one week and four weeks post-surgery) we calculated the mean spike rate for a total of n = 5 trials for both rest and walking (40 trials total). To statistically compare the spike rates we used a linear mixed model with time point and condition as fixed effects and animal as a random effect.

Motor cortex inactivation with muscimol: Rats (n=2) were lightly anaesthetized using a ketamine (30 $mg\ kg^{-1}$) and medetomidine (0.15 $mg\ kg^{-1}$) mixture (administered i.p.). Needle recording electrodes were then inserted into the *biceps brachii* and the *tibialis anterior* directly through the skin. Using the implanted fiber probes, 16 ms trains of 500 Hz, 200 μs square wave pulses (A-M Systems isolated pulse stimulator) were used to stimulate the forelimb and hindlimb motor cortices in alternation once every 2 seconds (0.25 Hz for each separate cortical region). 50 evoked EMG responses were recorded during each condition (A-M Systems amplifier, PowerLab acquisition system). Following a series of baseline recordings, 10 μL of muscimol was slowly injected through the hollow channel of the fiber implanted in the hindlimb motor cortex. A further series of recordings were taken 5 minutes post-muscimol injection. The rat was then allowed to recover from anesthesia for 24 hours, at which point anesthesia was then administered in the same manner and evoked EMGs were again recorded to ensure normal functionality had been restored.

Histological processing: At the study end-point, the animals were terminally anaesthetized with sodium pentobarbital (80 $mg\ kg^{-1}$ i.p.) and transcardially perfused with PBS, followed by 4% paraformaldehyde in PBS. Immediately after perfusion the brain was dissected free and post-fixed overnight at 4 $°C$, cryoprotected in 30% sucrose in PBS for 72 hours, and then embedded and frozen in optimum cutting temperature compound. The relevant region of the brain was then cut in 40 μm serial sections using a cryostat. The sections were then immunostained using the following primary antibodies: rabbit anti-GFAP (1:1500; Dako) to label astrocytes, rabbit anti-Iba1 (1:1500; Wako) to label microglia and macrophages, and guinea pig anti-NeuN (1:3000; Millipore) to label neuronal cell bodies. Complementary secondary antibodies were then used. The images were acquired using an Olympus VS120 and a Leica LSM-880 microscope.

5.2 Electrochemical fiber sensors

Electrochemical sensors have been widely adopted in analytical chemistry thanks to their sensitivity, experimental simplicity and low cost. Screen printing technology in particular has provided a cheap and reproducible method for the mass production of disposable electrochemical devices which are now marketed for industrial, pharmaceutical or environmental analyses. Surface modification of the carbon paste screen printed electrode (SPE) or glassy electrode with nanomaterials such as gold nanoparticles, carbon nanotubes and carbon black have further extended the performances of these devices [166]–[171]. Adopting new electrode configurations may further improve the versatility and sensitivity of electrochemical sensor devices. Examples include band ultramicroelectrodes obtained via slicing along the edge of screen-printed electrodes [172], ring-disc electrodes for hydrodynamic voltammetry [173], [174] and hole based micro tube electrodes for nanoliter samples. However, these approaches often rely on more complex post-processing of SPE and do not overcome their planar limitations. The possibility to produce fibers containing small electrodes in a precise arrangement makes the thermal drawing process a compelling method to produce electrochemical probes for point-of-care or in-situ monitoring with minimum footprints.

Electrochemical sensors rely on redox reactions and measure the flow of electrons through the system. They are generally composed of three electrodes: a working electrode (WE) where the oxidation or reduction of the analyte takes place, a counter electrode (CE) to complete the electrical circuit and a reference electrode (RE) used to define a reference potential. Each electrode has specific conditions to respect in terms of materials properties or dimensions. The material of the WE need to permit fast electron transfer and be electrochemically stable in the potential range of interest. Furthermore, the surface of the WE should have an electroactive area as large as possible to enhance the current amplitude. The CE needs to have a surface area larger than the WE in order not to be the limiting factor for the reaction kinetics and should be ideally inert as well. Previous studies revealed the compatibility of carbon-filled composites as working and counter electrode [175]–[177]. Finally, the pseudo RE needs to have a stable potential in the testing solution. The good electrochemical stability of the Pt-MG makes it a good candidate to serve as the RE.

In the next part we start by characterizing the stability of a Pt-MG electrode and then present two different designs of electrochemical fiber sensors containing Pt-MG and conductive polycarbonate (cPC) electrodes. We investigate their performance for paracetamol (APAP) detection in cyclic voltammetry and chrono amperometry. APAP is an electroactive substance which can be directly oxidized. Furthermore, it is one of the most commonly used analgesic drug to relieve headache and fever beside others. Even though its usage is safe at therapeutic doses, over-dosing can induce harmful side effects [178], [179].

5.2.1 Stability of the Pt-MG

Since the essential role of the pseudo-reference electrode is to control the potential at the working electrode, it is required that it has a constant potential over time. Therefore, the open circuit potential of the Pt-MG against a commercial Ag/AgCl reference electrode was measured in PBS. Figure 5-9 shows a photograph of the experimental set-up. As shown in Figure 5-9(b) the potential is stable for at least one hour with an average value of $269 \pm 3 \; mV$.
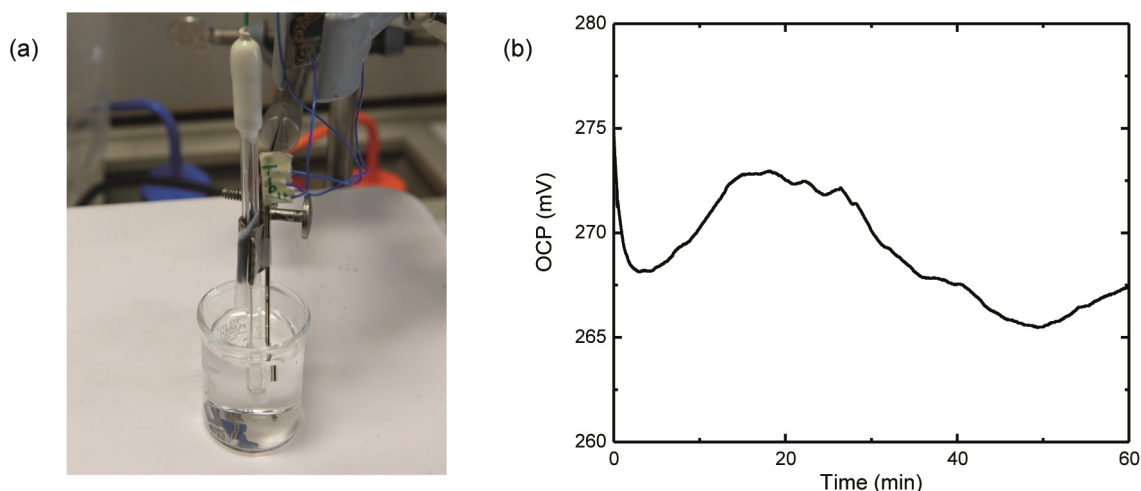
Figure 5-9 (a) Photograph of the experimental set-up. (b) OCP of Pt-MG versus Ag/AgCl

5.2.2 Fiber design

Two fiber designs were developed both composed of two cPC electrodes, acting as the WE and CE, and one Pt-MG electrode as the RE. The preforms were fabricated by drilling channels in polyetherimide (PEI) plates, hot pressing cPC parts with the appropriate dimensions, and hot pressing the full assembly as schematized in Figure 5-10(a) and (b).The first fiber, hereafter referred as fiber tip, displays the three electrodes at its tip. The electrode dimensions and position were selected to respect the requirements of having a CE surface larger than the WE one, and to facilitate the electrical connections. For the second fiber we exploited the fact that the Pt-MG is drawn in a highly viscous state to design a fiber having the three electrodes exposed inside a hollow channel continuously along the whole fiber length. This design enables us to significantly increase the electrode surface area since the latter is proportional to the length of the fiber filled with the solution to analyze. Cross-sectional images of the two fibers after thermal drawing are shown in Figure 5-10(c) and (d), respectively. By varying the drawing speed, fibers of different dimensions were processed.
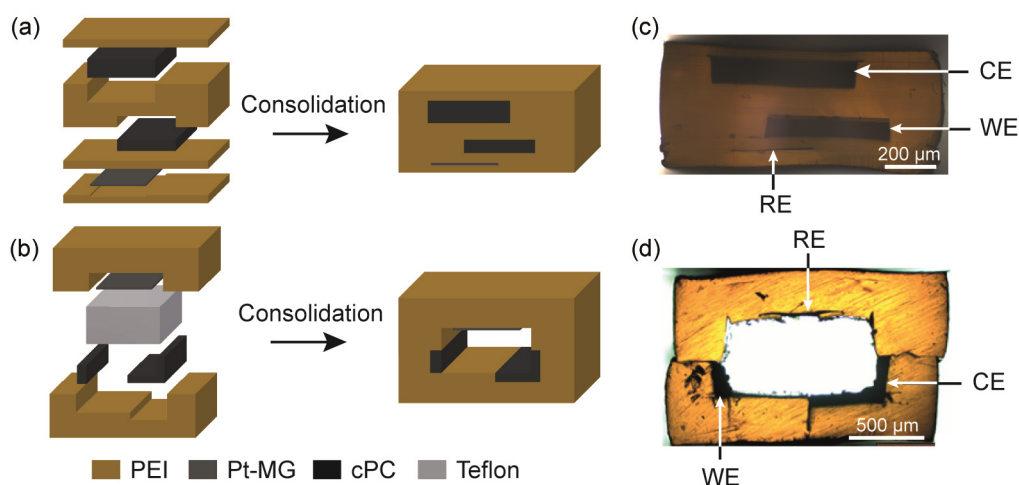
Figure 5-10 Electrochemical sensing fibers. (a) and (b) Schematic illustrations of the preform fabrication process of the fiber tip and hollow fiber. (c) and (d) OM micrographs of the fiber tip and hollow fiber cross-sections.

5.2.3   Fiber tip characterization

The sensing fibers were obtained by cutting 5 cm long probes from the drawn fibers with a razor blade, connecting on one side the electrodes to conductive wires and polishing with sandpapers the sensing surface on the other side. In Figure 5-11(a), the CV responses to pure PBS and 150 μM APAP are reported in blue. An increase in current is observed in presence of APAP due to the electrochemical reaction but the peak remains shallow. We assumed that the low sensitivity was caused by the low amount of carbon black particles exposed at the surface of the WE and therefore small electroactive surface area (EASA). Furthermore, the cut performed with a razor blade seemed to leave some cladding polymer residues on the electrode surface.

In order to enhance the response, we investigated different solvent treatments to increase the EASA of the WE. The optimum activation method consists in soaking the tip of the fiber 10 s in acetone, followed by drying in a vacuum oven at 80 °C for 5 min to remove any trace of acetone. This first step helps to remove any residual cladding polymer from the surface and induces some swelling of the PC matrix. Then, the fiber tip is soaked for around 10 s in dimethylformamide (DMF) which is a good solvent for PC but not for the PEI cladding and therefore allows us to dissolve selectively some PC at the surface of the electrodes, exposing a larger fraction of carbon particles. The CV response after the activation in PBS and in 150 μM APAP are shown in red in Figure 5-11(a). We can see that the treatment induces a well-defined peak with a higher peak current due the larger amount of exposed carbon black. Furthermore, a smaller separation between the oxidation and reduction peaks is observed which reveals faster electron transfer kinetics. SEM micrographs of the WE before and after the treatment shown in Figure 5-11(b) and (c) confirm the significant increase of conductive particles exposed at the surface.
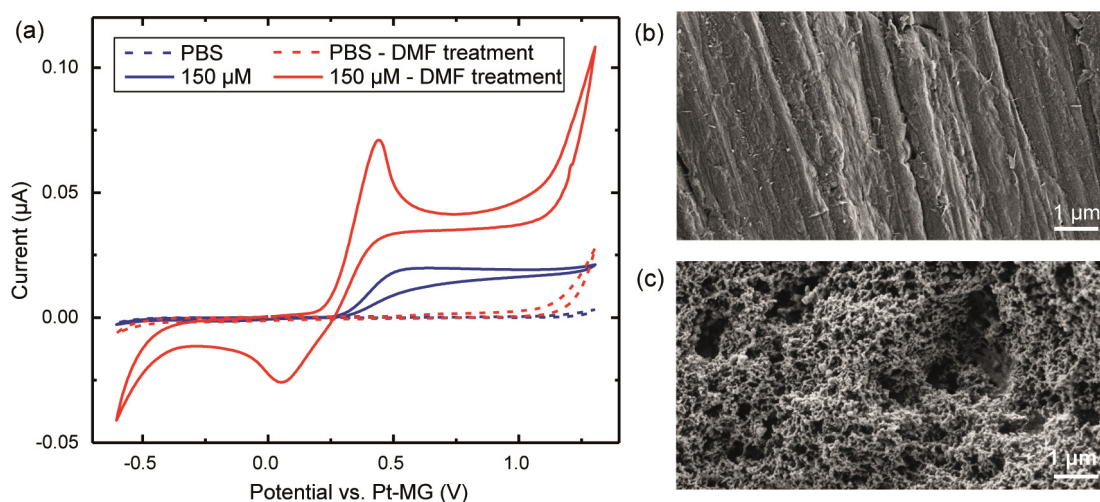
Figure 5-11 Fiber tip characterization: (a) Cyclic voltammograms of the fiber tip before (blue) and after (red) the solvent treatment recorded in PBS (dashed line) and in pure PBS + APAP 150 μM (continuous line). All voltammograms are recorded at a scan rate of 50 mVs^{-1}. SEM micrographs of the WE surface (b) after polishing and (c) after DMF treatment.

The CV measurements of the fiber tip after solvent treatment at APAP concentrations between 50 μM and 300 μM are shown in Figure 5-12(a). A regular increase in current is observed with increasing APAP content. Figure 5-12(b) shows a plot of the peak current, after subtraction of the PBS background, in function of the APAP concentration. A good linear relationship is observed in the tested range demonstrating the analytical ability for APAP detection of our fiber. The

sensitivity s of the sensor is defined as the slope of the fitting curve, and the limit of detection (LOD) can be estimated by $3\sigma_{PBS}/s$, where σ_{PBS} is the standard deviation of PBS scans (n=3) at the lowest peak potential. The former is 0.37 $nA\,\mu M^{-1}$ which is lower than SPE in absolute value but compares favorably with the commercial SPE if taking into account the different WE surface area ($8 \times 10^{-6}\,nA\,\mu M^{-1}\mu m^{-2}$ for the fiber tip, $4 \times 10^{-6}\,nA\,\mu M^{-1}\mu m^{-2}$ for the SPE) [166]. The latter is 1.7 μM and is also comparable to SPE [180]. Finally, the repeatability of the fiber tip is excellent as shown by the very small standard deviation calculated after five sequences of measurements with the same fiber. A low inter-fiber reproducibility was observed and may be caused by variance in the WE active area due to the manual cutting procedure or to heterogeneities in the carbon black composites.
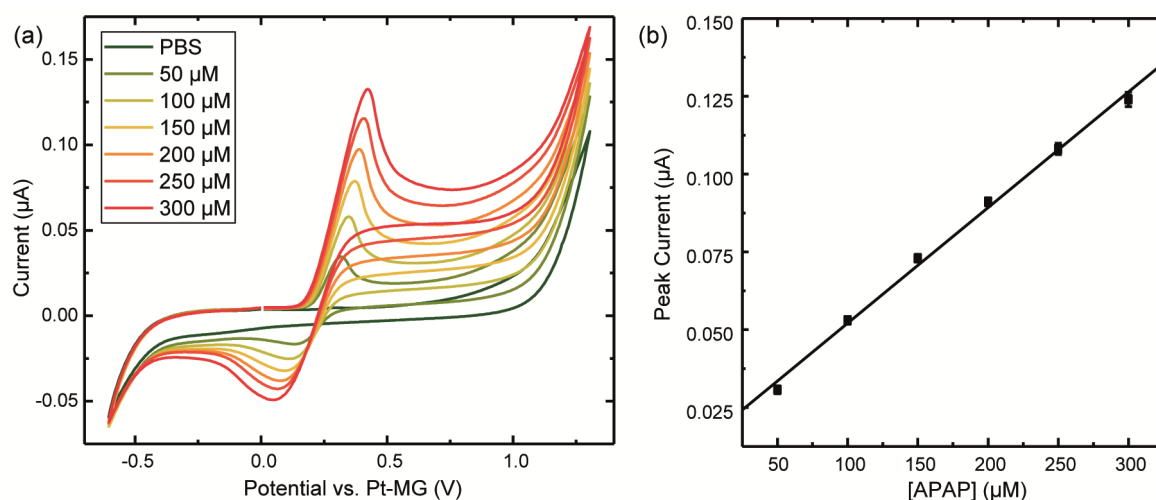
Figure 5-12 Fiber tip characterization: (a) Cyclic voltammograms for APAP detection in a PBS electrolyte. All voltammograms were measured at a scan rate of 50 mVs^{-1}. (b) Calibration plot for APAP detection with the vertical error bar representing the standard deviation between 5 measurements.

The performance of the fiber tip was then characterized in chrono amperometry (CA) by applying a constant voltage of 700 mV and measuring the current over time while injecting APAP. Figure 5-13(a) shows a chronoamperogram with successive injection of 0.5, 1, 2, 10 and 50 μM APAP, under constant stirring of 100 rpm. The calibration plot shown in Figure 5-13(b) is calculated by averaging the current over 30 s after each APAP injection as shown by the red and blue dots in Figure 5-13(a). An excellent linear relationship is observed in the tested range with a sensitivity of 0.46 $nA\,\mu M^{-1}$ and an estimated LOD of 0.22 μM ($3\sigma_{PBS}/s$). The latter reveal the very good sensing performance of our fiber but need to be considered with caution since the values depend strongly on the experimental conditions such as the stirring rate, which influences the analyte diffusion at the sensor surface.
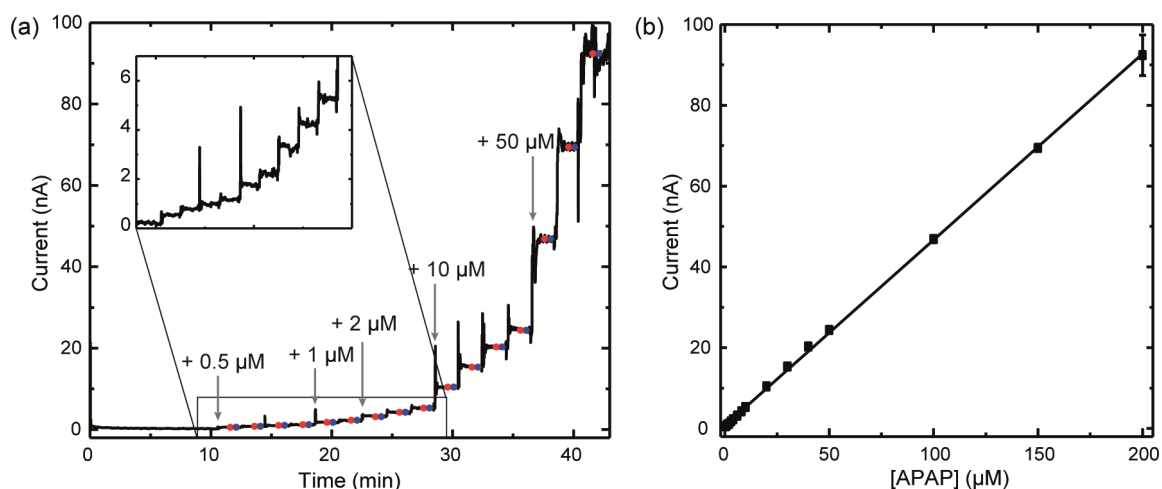
Figure 5-13 Fiber tip characterization: (a) Chronoamperogram with successive addition of APAP at 700 mV. Inset: zoom-in at low APAP concentration. (b) Calibration curve of the current versus APAP concentration.

5.2.4 Hollow fiber characterization

The second type of probe was prepared by again contacting the electrodes and connecting the fiber end to a pipette tip with a heat shrink tube. A precise volume of solution can then be drawn into the fiber using a micropipette as shown in Figure 5-14(a), which determines the surface area of the WE. We followed a similar CV procedure as for the fiber tip to assess the performance of this fiber for APAP detection, using a probe volume of 10 µL and a slower scan rate of 20 mVs^{-1}. The latter was necessary due to the slower electron transfer rate. The CV response to APAP concentrations ranging from 10 to 300 μM is presented in Figure 5-14(b). No surface activation was performed before the test which results in lower electron transfer rate and therefore smaller and broader peaks. Furthermore, a large shift in voltage with increasing concentration is also observed during the test. The latter suggests a limited mass transport from the bulk solution to the electrode surface. The concentration dependence might be caused by a concentration dependent diffusion coefficient.

From Figure 5-14(c) we can see a small deviation from the linear behavior at higher APAP concentration. The decrease in sensitivity at high concentration has been attributed to a decrease in EASA due to the accumulation of excess analyte at the surface of the electrode [181]. A sensitivity of 2.77 $nA\ \mu M^{-1}$ and LOD of 6.67 μM can be deduced from the calibration curve (Figure 5-14(c)). A higher sensitivity is observed compared to the fiber tip due to the larger WE surface area. However, the sensitivity per surface area is only 0.69 $\times\ 10^{-6}\ nA\ \mu M^{-1}\mu m^{-2}$ due to the lower amount of exposed carbon black.
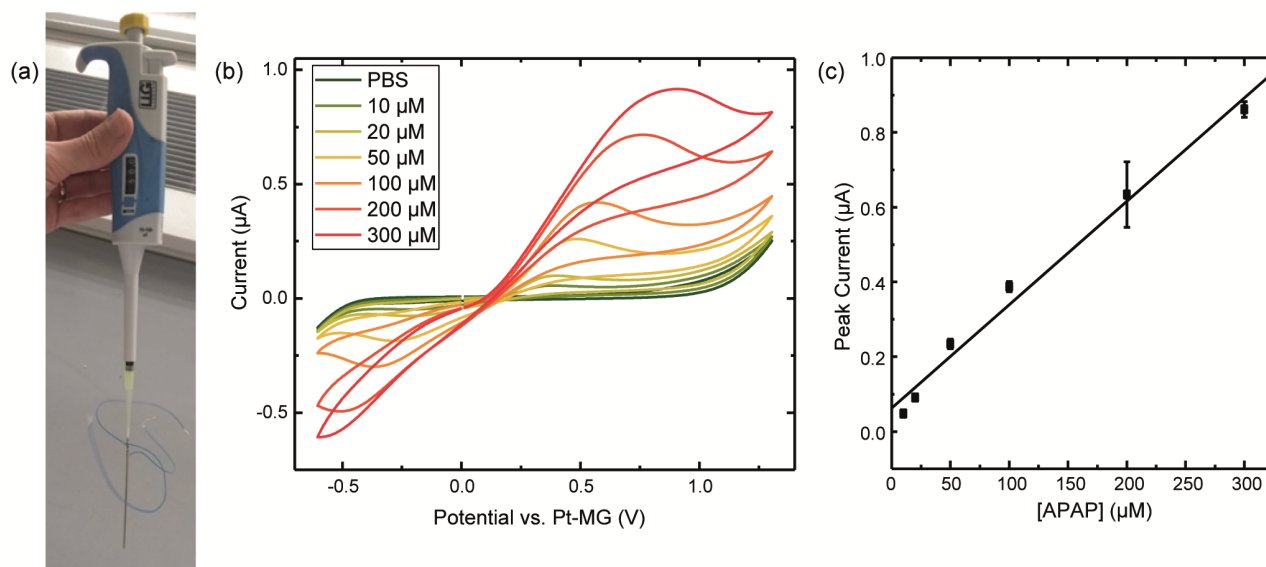
Figure 5-14 Hollow fiber characterization: (a) Picture of the experimental set-up. (b) CVs response to APAP concentrations between 10 and 300 μM, (c) Calibration curve. The vertical error bars represent the standard deviation between 3 measurements.

5.2.5   Materials and experimental methods

Materials: Polyetherimide plates and conductive polycarbonate (cPC) films were purchased from Boedeker and Goodfellow, respectively. The $Pt_{57.5}Cu_{14.7}Ni_{5.3}P_{22.5}$ master alloys were purchased from PXGroup (Switzerland) and processed by Dr. Kurtuldu at the Laboratory of Metal Physics and Technology at ETH Zürich. Ribbons were prepared by melt spinning on a Cu wheel with a rim speed of 20 ms^{-1}. APAP in powder form and PBS tablets (10x, pH: 7.4, 10 mM) were purchased from Sigma-Aldrich (Switzerland). A 30 mM stock solution was prepared by dissolving 5 mg of APAP in 1 mL of PBS.

Preform making: The fabrication of the preform is illustrated in Figure 5-10(a) and (b). The cPC parts were obtained by hot pressing cPC films at 180 $°C$ for 20 min under vacuum (Lauffer Pressen UVL 5.0). The complete preform consolidated at 240 $°C$ for 30 min in a Meyer press (Maschinenfabrik Herbert Meyer GmbH).

Thermal drawing: The two fibers were drawn at set temperatures of top: 210 $°C$, middle: 340 ± 3 $°C$, bottom: 130 $°C$, with a feeding speed of 1 $mm\ min^{-1}$ and drawing speeds between 100 and 500 $mm\ min^{-1}$ for the fiber tip and between 100 and 250 $mm\ min^{-1}$ for the hollow fiber.

Sensor preparation: The preparation of the probes is described in section 5.2.3 and 5.2.4. The cladding material was removed mechanically with a milling machine to expose the electrodes. Silver paint was used to ensure a low resistance between the electrodes and the conductive wires, and the contacts were protected with some super glue to increase their mechanical resistance. Glue was also added around the heat shrink tube to prevent any leakage.

Electrochemical characterization: Electrochemical measurements were performed using an Autoloab potentiostat (PGSTAT128N, Metrohm). The experiments were carried out at room temperature in a PBS electrolyte. For the OCP measurements, the fiber was immersed in the electrolyte with a reference electrode (Ag/AgCl K0265 AMETEK) and the measurement was performed in a two-electrode configuration with Pt-MG as the working electrode. CV responses of

the fiber tips were measured in a three-electrode configuration by connecting the three in-fiber electrodes (Pt-MG as the RE, cPC as the WE and CE) in 10 mL PBS electrolyte. Three spectra were recorded with a scan rate of 50 mVs^{-1} between voltages of -0.6 to 1.3 V. APAP stock solution was added to the electrolyte to reach the desired concentration and mixed for 1.5 minutes at a stirring speed of 250 rpm before recording the spectra. The third spectra of each test was used for the calibration. The chronoamperometric response was measured with the same set-up under a potential of 700 mV with a constant stirring of 100 rpm. 10 µL of solution was drawn in the hollow fiber before each test and the CV measurements were carried out with the same procedure than for the fiber tip but at a scan rate of 20 mVs^{-1}. All the fiber probes were cleaned by dipping them at least three times in distilled water between the different tests.

Scanning electron microscopy: Micrographs of the composite electrodes at the fiber tip were taken using a Zeiss Merlin field emission SEM (Zeiss, Göttingen) equipped with a GEMINI II column.

5.3 Summary and conclusion

In the first section, we demonstrated the excellent electrochemical properties of Pt-MG electrodes *in vitro* and *in vivo*. We then showed the capability of producing neural probes hosting multiple MG electrodes and microfluidic channels in a single step with thermal drawing. These probes are implantable, miniaturized and fully functional to form stable, long-term brain–machine interfaces in freely moving animals. We demonstrated that the probes conserve their recording capability for up to two months, and are capable of *in vivo* stimulation for more than three months, a feature that had not been demonstrated using other conductors in the fiber platform [9], [150], [158]. Furthermore, we showed that the chemotrode enables precise local delivery of drugs, illustrating the multimodal capabilities of the probes. More advanced fibers could be designed in the future such as integrating softer polymers or further miniaturizing the electrodes, in order to improve the long-term stability and functionality.

In the second part, we described the fabrication of novel lab-in-a-fiber electrochemical devices integrating cPC and Pt-MG electrodes. We started by demonstrating the stability of the Pt-MG electrode and then designed two architectures of fibers allowing point-of-care sensing. The activation of the working electrode surface by solvent treatment enabled a significant increase of the performance of the fiber tip sensor. Good linear relationships between the current and the APAP concentration were observed both in CV and CA experiments confirming the fiber ability for the electrochemical detection of paracetamol. Furthermore, promising sensing performances were demonstrated for a hollow fiber enabling detection using small volumes of solution. The dependence of the fiber sensor on the fiber geometry is nevertheless still unclear and should be the subject of future investigations. Optimization in terms of architecture and materials could further enhance the performance and several research directions are proposed in Chapter 6.

6 Conclusion

6.1 Achieved results

The aim of this thesis was to develop strategies to maintain the preform cross-section during thermal drawing, based on an in-depth understanding of the various mechanisms limiting it. Indeed, with the continuous increase in the fiber architecture complexity and the interest to reach always smaller dimensions, several phenomena start to play an important role for structure preservation. We focused on three different mechanisms which are: thermal reflow, polymer chain alignments and capillary instabilities. The main results for each parts are presented hereafter.

We started by investigating the reflow of surface textured fibers. We first developed an analytical model describing the reflow of periodic polymer micropatterns in isothermal annealing. We then extended the model to the thermal drawing process by including the scale down effect and the non-isothermal annealing. Experiments on square-grooved PMMA plates subjected to both treatments showed excellent agreement with the calculated theoretical values. Based on this model, we critically discussed the strategies employed to enhance the texture preservation and showed that lowering the reflow driving force holds the key for fiber texturing at feature sizes as low as few tens of nanometers. We demonstrated this finding by thermal drawing sub-100 nm structures in a PMMA-PC fiber, these two materials having a low interfacial tension.

In the second part of this work we investigated the influence of the thermal drawing process on the polymer morphology and final fiber properties. We first characterized the shrinkage behavior during annealing above the T_g. We showed that the drawing stress was proportional to the retractive stress developing inside the fibers, and that it controlled the amount of shrinkage. We then performed morphological characterization via SAXS and WAXS experiments to determine the degree of polymer chain orientation. An excellent correlation was obtained between the later and the total shrinkage. We then showed that our study could be extended to two other types of PMMAs and used our deeper understanding to design a heat-controlled bending fiber. Next, we proposed a thermal annealing strategy to reduce the amount of internal stress and in-fiber anisotropy in order to limit the shrinkage occurring during use or during an iterative drawing procedure. We applied it to a fiber containing a thin metallic glass electrode to enhance the operating range of this temperature detector by 50 %.

In the third part, we presented the thermal drawing of BMGs which enables the processing of very long, highly uniform and well-ordered micro- and nanoscale features. We started by identifying pairs of BMG-polymer with matching flow behavior: $Pt_{57.5}Cu_{14.7}Ni_{5.3}P_{22.5}$/PEI and $Au_{49}Ag_{5.5}Pd_{2.3}Cu_{26.9}Si_{16.3}$/PMMA. By overcoming the capillary-induced breakup, we first presented the ability to draw Pt-MG features down to tens of nanometer in a large variety of architectures. TEM analyses showed that the break-up of the ribbons with thicknesses below 40 nm is caused by the presence of nanocrystals. A fundamental study of the crystallization kinetics of nanoscale MG ribbons via in situ heating TEM

revealed size-dependent and deformation-dependent kinetics. Enhanced kinetics caused by the thermal drawing process was also demonstrated in microscale ribbons via DSC, XRD and SEM analyses. Finally, we presented the methodology we used to find a compatible PMMA cladding. The Au-MG alloy having faster crystallization kinetics, the ultimate thickness of the ribbons was found to be limited to few hundreds of nanometers.

Last, we demonstrated the versatile capability of the in-fiber Pt-MGs by means of two applications in neuroscience and electrochemical sensing, respectively. We started by demonstrating the enhanced electrochemical stability of the Pt-MG in comparison to crystalline metals *in vitro*. The latter enabled us to design neural probes for long-term stimulation and recording. *In vivo* tests revealed that the probes enabled electrical stimulation for more than three months and recording for up to eight weeks. Precise local drug delivery was also demonstrated by integrating a microfluidic channel in the fiber probes. We then presented the first thermally drawn fibers integrating all the necessary electrodes to act as an electrochemical sensor. We designed two types of fibers, one having the electrodes exposed only at the tip and the other one all along an empty channel, taking advantage of the high viscosity of all the components during the draw. We demonstrated their performance for paracetamol detection via cyclic voltammetry and chronoamperometry.

6.2 Future development

First, we achieved a very good agreement between our theoretical model describing the surface reflow and experimental data. Nevertheless, our model still involves some assumptions that could be alleviated in future research. Numerical solutions could be developed in order to take into account the nonlinearity of the Laplace pressure for patterns with a height larger than the periodicity ($h < \lambda$). In addition, our model could be extended to non-Newtonian fluids and the coupling between the thermal reflow and drawing scaling could also be considered to refine the model, particularly for materials with a strong non-Newtonian behavior.

In this thesis, we identified two BMGs to be co-drawn in polymer fibers. Future work would consist in determining if a wider range of BMGs could be co-drawn. The research of new BMGs is still on-going and further compositions could show compatible temperature dependent viscosity and crystallization kinetics. Furthermore, low melting point glass claddings could be used in order to increase the range of glass transition temperatures. Preliminary results on phosphate based glasses revealed promising temperature dependent viscosity for the thermal co-drawing with a Pd-based BMG for example.

The demonstration of the neuroscience application may be extended in several directions, including further miniaturization of the probe, recording along the fiber length via the capability of exposing electrodes on the fiber surface and incorporation of softer, more biocompatible polymers such as those used in tissue-like mesh electronics to further improve long-term stability and functionality [182], [183]. The electrochemical sensing fibers showed promising performance, but a better understanding of the influence of the sensor geometry on the diffusion kinetics and adsorption behavior of the analyte would be valuable. The fiber design could be optimized and new composite materials could be developed in order to increase the sensitivity of the fibers. Other types of fibers could be designed including additional functionalities such as drug delivery channels, or with electrodes exposed at the surface to integrate the

fibers in smart bandages for example [184]. The functionalization of the electrodes after drawing could be an interesting method to expand the range of sensing compounds.

Finally, thermal drawing enables the direct embedding of micro- and nanoscale MGs in a flexible polymer fiber matrix, which facilitates their handling and allows for direct integration with other functional materials. The diversity and good control over the final fiber architecture allow for novel applications in electronics, metamaterial optics or optoelectronics among others [145], [148]. Furthermore, our deeper understanding on the shrinkage behavior of the fibers could help to define strategies to successfully draw high density electrode arrays in fibers, which can enable high-resolution chemical imaging for example [185].

References

[1]   K. C. Kao and G. A. Hockham, "Dielectric-fibre surface waveguides for optical frequencies," *Proceedings of the Institution of Electrical Engineers*, vol. 113, no. 7, pp. 1151–1158, 1966.

[2]   M. Bayindir, F. Sorin, A. F. Abouraddy, J. Viens, S. D. Hart, J. D. Joannopoulos, and Y. Fink, "Metal–insulator–semiconductor optoelectronic fibres," *Nature*, vol. 431, no. 7010, Art. no. 7010, 2004.

[3]   A. F. Abouraddy, M. Bayindir, G. Benoit, S. D. Hart, K. Kuriki, N. Orf, O. Shapira, F. Sorin, B. Temelkuran, and Y. Fink, "Towards multimaterial multifunctional fibres that see, hear, sense and communicate," *Nat. Mater.*, vol. 6, no. 5, pp. 336–347, 2007.

[4]   G. Tao, A. M. Stolyarov, and A. F. Abouraddy, "Multimaterial Fibers," *Int J Appl Glass Sci*, vol. 3, no. 4, pp. 349–368, 2012.

[5]   W. Yan, A. Page, T. Nguyen-Dang, Y. Qu, F. Sordo, L. Wei, and F. Sorin, "Advanced Multimaterial Electronic and Optoelectronic Fibers and Textiles," *Advanced Materials*, vol. 31, no. 1, p. 1802348, 2019.

[6]   W. Yan, C. Dong, Y. Xiang, S. Jiang, A. Leber, G. Loke, W. Xu, C. Hou, S. Zhou, M. Chen, R. Hu, P. P. Shum, L. Wei, X. Jia, F. Sorin, X. Tao, and G. Tao, "Thermally drawn advanced functional fibers: New frontier of flexible electronics," *Materials Today*, 2020.

[7]   G. Loke, W. Yan, T. Khudiyev, G. Noel, and Y. Fink, "Recent Progress and Perspectives of Thermally Drawn Multimaterial Fiber Electronics," *Advanced Materials*, vol. 32, no. 1, p. 1904911, 2020.

[8]   Y. Qu, T. Nguyen-Dang, A. G. Page, W. Yan, T. D. Gupta, G. M. Rotaru, R. M. Rossi, V. D. Favrod, N. Bartolomei, and F. Sorin, "Superelastic Multimaterial Electronic and Photonic Fibers and Devices via Thermal Drawing," *Advanced Materials*, vol. 30, no. 27, p. 1707251, 2018.

[9]   A. Canales, X. Jia, U. P. Froriep, R. A. Koppes, C. M. Tringides, J. Selvidge, C. Lu, C. Hou, L. Wei, Y. Fink, and P. Anikeeva, "Multifunctional fibers for simultaneous optical, electrical and chemical interrogation of neural circuits in vivo," *Nature Biotechnology*, vol. 33, no. 3, Art. no. 3, 2015.

[10]   R. A. Koppes, S. Park, T. Hood, X. Jia, N. Abdolrahim Poorheravi, A. H. Achyuta, Y. Fink, and P. Anikeeva, "Thermally drawn fibers as nerve guidance scaffolds," *Biomaterials*, vol. 81, pp. 27–35, 2016.

[11]   C. Dong, A. Leber, T. Das Gupta, R. Chandran, M. Volpi, Y. Qu, T. Nguyen-Dang, N. Bartolomei, W. Yan, and F. Sorin, "High-efficiency super-elastic liquid metal based triboelectric fibers and textiles," *Nature Communications*, vol. 11, no. 1, Art. no. 1, 2020.

[12]   A. Leber, C. Dong, R. Chandran, T. Das Gupta, N. Bartolomei, and F. Sorin, "Soft and stretchable liquid metal transmission lines as distributed probes of multimodal deformations," *Nature Electronics*, vol. 3, no. 6, Art. no. 6, 2020.

[13]   M. A. Schmidt, A. Argyros, and F. Sorin, "Hybrid Optical Fibers – An Innovative Platform for In-Fiber Photonic Devices," *Advanced Optical Materials*, vol. 4, no. 1, pp. 13–36, 2016.

[14]   E. Pone, C. Dubois, N. Guo, Y. Gao, A. Dupuis, F. Boismenu, S. Lacroix, and M. Skorobogatiy, "Drawing of the hollow all-polymer Bragg fibers," *Opt. Express, OE*, vol. 14, no. 13, pp. 5838–5852, 2006.

[15]   D. T. Nguyen, "Tailoring Surface Properties of Fiber Materials Novel Opportunities in the Fabrication of Multi-scale Fiber-based Architectures," Doctoral thesis, EPFL, Lausanne, 2017.

[16]   T. Nguyen-Dang, A. C. de Luca, W. Yan, Y. Qu, A. G. Page, M. Volpi, T. D. Gupta, S. P. Lacour, and F. Sorin, "Controlled Sub-Micrometer Hierarchical Textures Engineered in Polymeric Fibers and Microchannels via Thermal Drawing," *Advanced Functional Materials*, vol. 27, no. 10, p. 1605935, 2017.

[17]   A. Yildirim, M. Yunusa, F. E. Ozturk, M. Kanik, and M. Bayindir, "Surface Textured Polymer Fibers for Microfluidics," *Advanced Functional Materials*, vol. 24, no. 29, pp. 4569–4576, 2014.

[18]   T. Khudiyev, C. Hou, A. M. Stolyarov, and Y. Fink, "Sub-Micrometer Surface-Patterned Ribbon Fibers and Textiles," *Advanced Materials*, vol. 29, no. 22, p. 1605868, 2017.

[19]   J. A. F. Plateau, *Statique expérimentale et théorique des liquides soumis aux seules forces moléculaires*. Gauthier-Villars, 1873.

[20]   Lord Rayleigh, "On The Instability Of Jets," *Proceedings of the London Mathematical Society*, vol. s1-10, no. 1, pp. 4–13, 1878.

[21]   S. Tomotika, "On the Instability of a Cylindrical Thread of a Viscous Liquid Surrounded by Another Viscous Fluid," *Proceedings of the Royal Society A: Mathematical, Physical and Engineering Sciences*, vol. 150, no. 870, pp. 322–337, 1935.

[22]   D. S. Deng, J. C. Nave, X. Liang, S. G. Johnson, and Y. Fink, "Exploration of in-fiber nanostructures from capillary instability," *Optics Express*, vol. 19, no. 17, pp. 16273–16290, 2011.

[23]   A. Alchalaby, R. Lwin, H. Al-Janabi, P. Trimby, S. Fleming, B. Kuhlmey, and A. Argyros, "Investigation of Plateau-Rayleigh Instability in Drawn Metal-Polymer Composite Fibres for Metamaterials Fabrication," *Journal of Lightwave Technology*, vol. 34, pp. 1–1, 2015.

[24]   S. Xue, G. W. Barton, S. Fleming, and A. Argyros, "Analysis of Capillary Instability in Metamaterials Fabrication Using Fiber Drawing Technology," *Journal of Lightwave Technology*, vol. 35, no. 11, pp. 2167–2174, 2017.

[25]   B. Xu, S. Ma, Y. Xiang, J. Zhang, M. Zhu, L. Wei, G. Tao, and D. Deng, "In-Fiber Structured Particles and Filament Arrays from the Perspective of Fluid Instabilities," *Adv. Fiber Mater.*, vol. 2, no. 1, pp. 1–12, 2020.

[26]   M. Yaman, T. Khudiyev, E. Ozgur, M. Kanik, O. Aktas, E. O. Ozgur, H. Deniz, E. Korkut, and M. Bayindir, "Arrays of indefinitely long uniform nanowires and nanotubes," *Nat Mater*, vol. 10, no. 7, pp. 494–501, 2011.

[27]   J. J. Kaufman, G. Tao, S. Shabahang, D. S. Deng, Y. Fink, and A. F. Abouraddy, "Thermal Drawing of High-Density Macroscopic Arrays of Well-Ordered Sub-5-nm-Diameter Nanowires," *Nano Lett.*, vol. 11, no. 11, pp. 4768–4773, 2011.

[28] O. T. Naman, M. R. New-Tolley, R. Lwin, A. Tuniz, A. H. Al-Janabi, I. Karatchevtseva, S. C. Fleming, B. T. Kuhlmey, and A. Argyros, "Indefinite Media Based on Wire Array Metamaterials for the THz and Mid-IR," *Advanced Optical Materials*, vol. 1, no. 12, pp. 971–977, 2013.

[29] E. Badinter, A. Ioisher, E. Monaico, V. Postolache, and I. M. Tiginyanu, "Exceptional integration of metal or semimetal nanowires in human-hair-like glass fiber," *Materials Letters*, vol. 64, no. 17, pp. 1902–1904, 2010.

[30] M. S. Moslan, M. H. D. Othman, A. Samavati, M. A. M. Salim, M. A. Rahman, A. F. Ismail, and H. Bakhtiar, "Fabrication of polycarbonate polymer optical fibre core via extrusion method: The role of temperature gradient and collector speed on its characteristics," *Optical Fiber Technology*, vol. 55, p. 102162, 2020.

[31] O. Teall, M. Pilegis, J. Sweeney, T. Gough, G. Thompson, A. Jefferson, R. Lark, and D. Gardner, "Development of high shrinkage polyethylene terephthalate (PET) shape memory polymer tendons for concrete crack closure," *Smart Mater. Struct.*, vol. 26, no. 4, p. 045006, 2017.

[32] J. Y. Lim and S. Y. Kim, "Thermal shrinkage stress in high-speed-spun, high molecular weight poly(ethylene terephthalate) filaments," *Journal of Polymer Science Part B: Polymer Physics*, vol. 39, no. 9, pp. 964–972, 2001.

[33] C. Ru, F. Wang, M. Pang, L. Sun, R. Chen, and Y. Sun, "Suspended, Shrinkage-Free, Electrospun PLGA Nanofibrous Scaffold for Skin Tissue Engineering," *ACS Appl. Mater. Interfaces*, vol. 7, no. 20, pp. 10872–10877, 2015.

[34] V. B. Gupta, J. Radhakrishnan, and S. K. Sett, "Effect of processing history on shrinkage stress in axially oriented poly(ethylene terephthalate) fibres and films," *Polymer*, vol. 35, no. 12, pp. 2560–2567, 1994.

[35] C. Jiang, M. G. Kuzyk, J.-L. Ding, W. E. Johns, and D. J. Welker, "Fabrication and mechanical behavior of dye-doped polymer optical fiber," *Journal of Applied Physics*, vol. 92, no. 1, pp. 4–12, 2002.

[36] W. Okumura, Y. Ohkoshi, Y. Gotoh, M. Nagura, H. Urakawa, and K. Kajiwara, "Effects of the drawing form and draw ratio on the fiber structure and mechanical properties of CO2-laser-heated-drawn poly(ethylene terephthalate) fibers," *Journal of Polymer Science Part B: Polymer Physics*, vol. 42, no. 1, pp. 79–90, 2004.

[37] P. Stajanca, O. Cetinkaya, M. Schukar, P. Mergo, D. J. Webb, and K. Krebber, "Molecular alignment relaxation in polymer optical fibers for sensing applications," *Optical Fiber Technology*, vol. 28, pp. 11–17, 2016.

[38] H. C. Kim, D. Kim, J. Y. Lee, L. Zhai, and J. Kim, "Effect of Wet Spinning and Stretching to Enhance Mechanical Properties of Cellulose Nanofiber Filament," *Int. J. of Precis. Eng. and Manuf.-Green Tech.*, vol. 6, no. 3, pp. 567–575, 2019.

[39] D. J. A. Senden, J. A. W. van Dommelen, and L. E. Govaert, "Strain hardening and its relation to Bauschinger effects in oriented polymers," *Journal of Polymer Science Part B: Polymer Physics*, vol. 48, no. 13, pp. 1483–1494, 2010.

[40] S. Shen, A. Henry, J. Tong, R. Zheng, and G. Chen, "Polyethylene nanofibres with very high thermal conductivities," *Nature Nanotechnology*, vol. 5, no. 4, Art. no. 4, 2010.

[41] T. Pakula and M. Trznadel, "Thermally stimulated shrinkage forces in oriented polymers: 1. Temperature dependence," *Polymer*, vol. 26, no. 7, pp. 1011–1018, 1985.

[42] M. Kanik, S. Orguc, G. Varnavides, J. Kim, T. Benavides, D. Gonzalez, T. Akintilo, C. C. Tasan, A. P. Chandrakasan, Y. Fink, and P. Anikeeva, "Strain-programmable fiber-based artificial muscle," *Science*, vol. 365, no. 6449, pp. 145–150, 2019.

[43] S. Shadman, T. Nguyen-Dang, T. D. Gupta, A. G. Page, I. Richard, A. Leber, J. Ruza, G. Krishnamani, and F. Sorin, "Microstructured Biodegradable Fibers for Advanced Control Delivery," *Advanced Functional Materials*, vol. 30, no. 13, p. 1910283, 2020.

[44] E. B. Pitt, G. Kumar, and J. Schroers, "Temperature dependence of the thermoplastic formability in bulk metallic glasses," *Journal of Applied Physics*, vol. 110, no. 4, p. 043518, 2011.

[45] N. Li, W. Chen, and L. Liu, "Thermoplastic Micro-Forming of Bulk Metallic Glasses: A Review," *JOM*, vol. 68, no. 4, pp. 1246–1261, 2016.

[46] G. Duan, A. Wiest, M. L. Lind, J. Li, W.-K. Rhim, and W. L. Johnson, "Bulk Metallic Glass with Benchmark Thermoplastic Processability," *Adv. Mater.*, vol. 19, no. 23, pp. 4272–4275, 2007.

[47] M. M. Khan, A. Nemati, Z. U. Rahman, U. H. Shah, H. Asgar, and W. Haider, "Recent Advancements in Bulk Metallic Glasses and Their Applications: A Review," *Critical Reviews in Solid State and Materials Sciences*, vol. 43, no. 3, pp. 233–268, 2018.

[48] G. Kumar, A. Desai, and J. Schroers, "Bulk Metallic Glass: The Smaller the Better," *Adv. Mater.*, vol. 23, no. 4, pp. 461–476, 2011.

[49] G. Kumar, H. X. Tang, and J. Schroers, "Nanomoulding with amorphous metals," *Nature*, vol. 457, no. 7231, pp. 868–872, 2009.

[50] M. Hasan and G. Kumar, "High-throughput drawing and testing of metallic glass nanostructures," *Nanoscale*, vol. 9, no. 9, pp. 3261–3268, 2017.

[51] J. Yi, X. X. Xia, D. Q. Zhao, M. X. Pan, H. Y. Bai, and W. H. Wang, "Micro-and Nanoscale Metallic Glassy Fibers," *Adv. Eng. Mater.*, vol. 12, no. 11, pp. 1117–1122, 2010.

[52] A. L. Greer, "Confusion by design," *Nature*, vol. 366, no. 6453, Art. no. 6453, 1993.

[53] A. Inoue, "Stabilization of metallic supercooled liquid and bulk amorphous alloys," *Acta Materialia*, vol. 48, no. 1, pp. 279–306, 2000.

[54] T. Wen, W. Yao, and N. Wang, "Correlation between the Arrhenius crossover and the glass forming ability in metallic glasses," *Scientific Reports*, vol. 7, no. 1, Art. no. 1, 2017.

[55] Z. Long, H. Wei, Y. Ding, P. Zhang, G. Xie, and A. Inoue, "A new criterion for predicting the glass-forming ability of bulk metallic glasses," *Journal of Alloys and Compounds*, vol. 475, no. 1, pp. 207–219, 2009.

[56] Z. P. Lu and C. T. Liu, "A new glass-forming ability criterion for bulk metallic glasses," *Acta Materialia*, vol. 50, no. 13, pp. 3501–3512, 2002.

[57] O. Gross, S. S. Riegler, M. Stolpe, B. Bochtler, A. Kuball, S. Hechler, R. Busch, and I. Gallino, "On the high glass-forming ability of Pt-Cu-Ni/Co-P-based liquids," *Acta Materialia*, vol. 141, pp. 109–119, 2017.

[58]   J. Schroers, Y. Wu, R. Busch, and W. L. Johnson, "Transition from nucleation controlled to growth controlled crystallization in Pd43Ni10Cu27P20 melts," *Acta Materialia*, vol. 49, no. 14, pp. 2773–2781, 2001.

[59]   J. F. Löffler, J. Schroers, and W. L. Johnson, "Time–temperature–transformation diagram and microstructures of bulk glass forming Pd40Cu30Ni10P20," *Appl. Phys. Lett.*, vol. 77, no. 5, pp. 681–683, 2000.

[60]   D. Xu and W. L. Johnson, "Crystallization kinetics and glass-forming ability of bulk metallic glasses Pd40Cu30Ni10P20 and Zr41.2Ti13.8Cu12.5Ni10Be22.5 from classical theory," *Phys. Rev. B*, vol. 74, no. 2, p. 024207, 2006.

[61]   C. A. Angell, "Formation of Glasses from Liquids and Biopolymers," *Science*, vol. 267, no. 5206, pp. 1924–1935, 1995.

[62]   R. Busch, J. Schroers, and W. H. Wang, "Thermodynamics and Kinetics of Bulk Metallic Glass," *MRS Bulletin*, vol. 32, no. 8, pp. 620–623, 2007.

[63]   I. Gallino, "On the Fragility of Bulk Metallic Glass Forming Liquids," *Entropy*, vol. 19, p. 483, 2017.

[64]   D. Ma, A. D. Stoica, and X.-L. Wang, "Power-law scaling and fractal nature of medium-range order in metallic glasses," *Nature Materials*, vol. 8, no. 1, Art. no. 1, 2009.

[65]   H. W. Sheng, W. K. Luo, F. M. Alamgir, J. M. Bai, and E. Ma, "Atomic packing and short-to-medium-range order in metallic glasses," *Nature*, vol. 439, no. 7075, Art. no. 7075, 2006.

[66]   D. B. Miracle, "A structural model for metallic glasses," *Nature Materials*, vol. 3, no. 10, Art. no. 10, 2004.

[67]   A. Hirata, P. Guan, T. Fujita, Y. Hirotsu, A. Inoue, A. R. Yavari, T. Sakurai, and M. Chen, "Direct observation of local atomic order in a metallic glass," *Nature Materials*, vol. 10, no. 1, Art. no. 1, 2011.

[68]   F. Spaepen, "A microscopic mechanism for steady state inhomogeneous flow in metallic glasses," *Acta Metallurgica*, vol. 25, no. 4, pp. 407–415, 1977.

[69]   A. S. Argon, "Plastic deformation in metallic glasses," *Acta Metallurgica*, vol. 27, no. 1, pp. 47–58, 1979.

[70]   S. Hilke, H. Rösner, D. Geissler, A. Gebert, M. Peterlechner, and G. Wilde, "The influence of deformation on the medium-range order of a Zr-based bulk metallic glass characterized by variable resolution fluctuation electron microscopy," *Acta Materialia*, vol. 171, pp. 275–281, 2019.

[71]   F. A. Davani, S. Hilke, H. Rösner, D. Geissler, A. Gebert, and G. Wilde, "On the shear-affected zone of shear bands in bulk metallic glasses," *Journal of Alloys and Compounds*, vol. 837, p. 155494, 2020.

[72]   G. Z. Ma, K. K. Song, B. A. Sun, Z. J. Yan, U. Kühn, D. Chen, and J. Eckert, "Effect of cold-rolling on the crystallization behavior of a CuZr-based bulk metallic glass," *J Mater Sci*, vol. 48, no. 19, pp. 6825–6832, 2013.

[73]   S. Scudino, B. Jerliu, K. B. Surreddi, U. Kühn, and J. Eckert, "Effect of cold rolling on compressive and tensile mechanical properties of Zr52.5Ti5Cu18Ni14.5Al10 bulk metallic glass," *Journal of Alloys and Compounds*, vol. 509, pp. S128–S130, 2011.

[74]   D. J. Magagnosc, W. Chen, G. Kumar, J. Schroers, and D. S. Gianola, "Thermomechanical Behavior of Molded Metallic Glass Nanowires," *Sci Rep*, vol. 6, 2016.

[75]   W. L. Johnson, J. Lu, and M. D. Demetriou, "Deformation and flow in bulk metallic glasses and deeply undercooled glass forming liquids—a self consistent dynamic free volume model," *Intermetallics*, vol. 10, no. 11, pp. 1039–1046, 2002.

[76]   J. Lu, G. Ravichandran, and W. L. Johnson, "Deformation behavior of the Zr41.2Ti13.8Cu12.5Ni10Be22.5 bulk metallic glass over a wide range of strain-rates and temperatures," *Acta Materialia*, vol. 51, no. 12, pp. 3429–3443, 2003.

[77]   M. M. Trexler and N. N. Thadhani, "Mechanical properties of bulk metallic glasses," *Progress in Materials Science*, vol. 55, no. 8, pp. 759–839, 2010.

[78]   P. Bordeenithikasem, S. Sohn, Z. Liu, and J. Schroers, "Protocols for multi-step thermoplastic processing of metallic glasses," *Scripta Materialia*, vol. 104, pp. 56–59, 2015.

[79]   S. Pogatscher, P. J. Uggowitzer, and J. F. Löffler, "In-situ probing of metallic glass formation and crystallization upon heating and cooling via fast differential scanning calorimetry," *Appl. Phys. Lett.*, vol. 104, no. 25, p. 251908, 2014.

[80]   Q. P. Cao, J. F. Li, Y. H. Zhou, A. Horsewell, and J. Z. Jiang, "Effect of rolling deformation on the microstructure of bulk Cu60Zr20Ti20 metallic glass and its crystallization," *Acta Materialia*, vol. 54, no. 16, pp. 4373–4383, 2006.

[81]   Yu. P. Mitrofanov, M. Peterlechner, I. Binkowski, M. Yu. Zadorozhnyy, I. S. Golovin, S. V. Divinski, and G. Wilde, "The impact of elastic and plastic strain on relaxation and crystallization of Pd–Ni–P-based bulk metallic glasses," *Acta Materialia*, vol. 90, pp. 318–329, 2015.

[82]   H. Zhou, M. Peterlechner, S. Hilke, D. Shen, and G. Wilde, "Influence of plastic deformation by high-pressure torsion on the crystallization kinetics of a Pd40Ni40P20 bulk metallic glass," *Journal of Alloys and Compounds*, vol. 821, p. 153254, 2020.

[83]   D. H. Bae, H. K. Lim, S. H. Kim, D. H. Kim, and W. T. Kim, "Mechanical behavior of a bulk Cu–Ti–Zr–Ni–Si–Sn metallic glass forming nano-crystal aggregate bands during deformation in the supercooled liquid region," *Acta Materialia*, vol. 50, no. 7, pp. 1749–1759, 2002.

[84]   H.-S. Shin, Y.-J. Jeong, H.-Y. Choi, and A. Inoue, "Influence of crystallization on the deformation behavior of Zr55Al10Ni5Cu30 bulk metallic glass in the supercooled liquid region," *Materials Science and Engineering: A*, vol. 449, pp. 243–247, 2007.

[85]   T. G. Nieh, J. Wadsworth, C. T. Liu, T. Ohkubo, and Y. Hirotsu, "Plasticity and structural instability in a bulk metallic glass deformed in the supercooled liquid region," *Acta Materialia*, vol. 49, no. 15, pp. 2887–2896, 2001.

[86]   W. J. Kim, D. S. Ma, and H. G. Jeong, "Superplastic flow in a Zr65Al10Ni10Cu15 metallic glass crystallized during deformation in a supercooled liquid region," *Scripta Materialia*, vol. 49, no. 11, pp. 1067–1073, 2003.

[87]   G. T. Bae, S. B. Lee, K. S. Lee, Y. W. Chang, and N. J. Kim, "Effect of Strain on the Crystallization Kinetics of Bulk Amorphous Alloys," *Journal of Metastable and Nanocrystalline Materials*, 2005.

[88]   S. Cheng, C. Wang, M. Ma, D. Shan, and B. Guo, "Mechanism for microstructural evolution induced by high temperature deformation in Zr-based bulk metallic glasses," *Journal of Alloys and Compounds*, vol. 676, pp. 299–304, 2016.

[89]   K. J. Laws, B. Gun, and M. Ferry, "Mechanical stability of Ca65Mg15Zn20 bulk metallic glass during deformation in the super-cooled liquid region," *Materials Science and Engineering: A*, vol. 480, no. 1–2, pp. 198–204, 2008.

[90] M. D. Demetriou and W. L. Johnson, "Shear flow characteristics and crystallization kinetics during steady non-isothermal flow of Vitreloy-1," *Acta Materialia*, vol. 52, no. 12, pp. 3403–3412, 2004.

[91] J. H. Luo, F. F. Wu, J. Y. Huang, J. Q. Wang, and S. X. Mao, "Superelongation and Atomic Chain Formation in Nanosized Metallic Glass," *Phys. Rev. Lett.*, vol. 104, no. 21, p. 215503, 2010.

[92] J. Yi, W. H. Wang, and J. J. Lewandowski, "Sample size and preparation effects on the tensile ductility of Pd-based metallic glass nanowires," *Acta Materialia*, vol. 87, pp. 1–7, 2015.

[93] D. J. Magagnosc, R. Ehrbar, G. Kumar, M. R. He, J. Schroers, and D. S. Gianola, "Tunable Tensile Ductility in Metallic Glasses," *Scientific Reports*, vol. 3, no. 1, Art. no. 1, 2013.

[94] Y. Wu, H. H. Wu, X. D. Hui, G. L. Chen, and Z. P. Lu, "Effects of drawing on the tensile fracture strength and its reliability of small-sized metallic glasses," *Acta Materialia*, vol. 58, no. 7, pp. 2564–2576, 2010.

[95] Z. Shao, M. Gopinadhan, G. Kumar, S. Mukherjee, Y. Liu, C. S. O'Hern, J. Schroers, and C. O. Osuji, "Size-dependent viscosity in the super-cooled liquid state of a bulk metallic glass," *Appl. Phys. Lett.*, vol. 102, no. 22, p. 221901, 2013.

[96] M. Gopinadhan, Z. Shao, Y. Liu, S. Mukherjee, R. C. Sekol, G. Kumar, A. D. Taylor, J. Schroers, and C. O. Osuji, "Finite size effects in the crystallization of a bulk metallic glass," *Appl. Phys. Lett.*, vol. 103, no. 11, p. 111912, 2013.

[97] S. Sohn, Y. Jung, Y. Xie, C. Osuji, J. Schroers, and J. J. Cha, "Nanoscale size effects in crystallization of metallic glass nanorods," *Nature Communications*, vol. 6, p. 8157, 2015.

[98] S. Sohn, Y. Xie, Y. Jung, J. Schroers, and J. J. Cha, "Tailoring crystallization phases in metallic glass nanorods via nucleus starvation," *Nature Communications*, vol. 8, no. 1, p. 1980, 2017.

[99] U. Köster, "Surface crystallization of metallic glasses," *Materials Science and Engineering*, vol. 97, pp. 233–239, 1988.

[100] C. R. Cao, Y. M. Lu, H. Y. Bai, and W. H. Wang, "High surface mobility and fast surface enhanced crystallization of metallic glass," *Appl. Phys. Lett.*, vol. 107, no. 14, p. 141606, 2015.

[101] E.-H. Banaei and A. F. Abouraddy, "Design of a polymer optical fiber luminescent solar concentrator," *Progress in Photovoltaics: Research and Applications*, vol. 23, no. 4, pp. 403–416, 2015.

[102] L. G. Leal, *Advanced Transport Phenomena: Fluid Mechanics and Convective Transport Processes*. Cambridge University Press, 2007.

[103] T. Leveder, S. Landis, and L. Davoust, "Reflow dynamics of thin patterned viscous films," *Appl. Phys. Lett.*, vol. 92, no. 1, p. 013107, 2008.

[104] M. Hamdorf and D. Johannsmann, "Surface-rheological measurements on glass forming polymers based on the surface tension driven decay of imprinted corrugation gratings," *J. Chem. Phys.*, vol. 112, no. 9, pp. 4262–4270, 2000.

[105] M. L. Henle and A. J. Levine, "Capillary wave dynamics on supported viscoelastic films: Single and double layers," *Phys. Rev. E*, vol. 75, no. 2, p. 021604, 2007.

[106] J. E. Mark, Ed., *Physical Properties of Polymers Handbook*, 2nd ed. New York: Springer-Verlag, 2007.

[107] S. C. Xue, M. C. J. Large, G. W. Barton, R. I. Tanner, L. Poladian, and R. Lwin, "Role of material properties and drawing conditions in the fabrication of microstructured optical fibers," *Journal of Lightwave Technology*, vol. 24, no. 2, pp. 853–860, 2006.

[108] S. C. Xue, R. I. Tanner, G. W. Barton, R. Lwin, M. C. J. Large, and L. Poladian, "Fabrication of microstructured optical fibers-part I: problem formulation and numerical modeling of transient draw process," *Journal of Lightwave Technology*, vol. 23, no. 7, pp. 2245–2254, 2005.

[109] T. Nguyen-Dang, A. C. de Luca, W. Yan, Y. Qu, A. G. Page, M. Volpi, T. Das Gupta, S. P. S. P. S. P. Lacour, and F. Sorin, "Controlled Sub-Micrometer Hierarchical Textures Engineered in Polymeric Fibers and Microchannels via Thermal Drawing," *Advanced Functional Materials*, vol. 27, no. 10, p. 1605935, 2017.

[110] S. Wu, *Polymer interface and adhesion*. New York; Basel: Marcel Dekker, 1982.

[111] H. T. Pham and C. J. Carriere, "The effect of temperature on the interfacial tension of polycarbonate/polyethylene blends," *Polymer Engineering & Science*, vol. 37, no. 3, pp. 636–639, 1997.

[112] T. Nguyen-Dang, A. G. Page, Y. Qu, M. Volpi, W. Yan, and F. Sorin, "Multi-material micro-electromechanical fibers with bendable functional domains," *J. Phys. D: Appl. Phys.*, vol. 50, no. 14, p. 144001, 2017.

[113] T. Khudiyev, J. Clayton, E. Levy, N. Chocat, A. Gumennik, A. M. Stolyarov, J. Joannopoulos, and Y. Fink, "Electrostrictive microelectromechanical fibres and textiles," *Nature Communications*, vol. 8, no. 1, Art. no. 1, 2017.

[114] H. Schift, C. Spreu, A. Schleunitz, and J. Lee, "Shape control of polymer reflow structures fabricated by nanoimprint lithography," *Microelectronic Engineering*, vol. 88, no. 1, pp. 87–92, 2011.

[115] R. W. Lenz and R. S. Stein, *Structure and Properties of Polymer Films*, vol. 1. Springer US, 1973.

[116] L. C. E. Struik, *Internal Stresses, Dimensional Instabilities and Molecular Orientations in Plastics*. Chichester, United Kingdom: John Wiley and Sons Ltd, 1990.

[117] D. J. A. Senden, "Strain hardening and anisotropy in solid polymers," 2013.

[118] L. E. Nielsen and R. F. Landel, *Mechanical Properties of Polymers and Composites*, 2nd ed. CRC Press, 1993.

[119] M. Trznadel and M. Kryszewski, "Shrinkage and related relaxation of internal stresses in oriented glassy polymers," *Polymer*, vol. 29, no. 3, pp. 418–425, 1988.

[120] Z. Zhao, X. Zhao, J. Liu, W. Wang, J. Mays, and S.-Q. Wang, "Characterizing effects of fast melt deformation on entangled polymers in their glassy state," *J. Chem. Phys.*, vol. 151, no. 12, p. 124906, 2019.

[121] M. M. El-Tonsy, M. S. Meikhail, and R. M. Felfel, "Automatic measurement of the absolute CTE of thin polymer samples. II. Effect of chain orientation on thermal expansion of drawn polymer films," *Journal of Applied Polymer Science*, vol. 100, no. 6, pp. 4452–4460, 2006.

[122] M. Heinle and D. Drummer, "Temperature-dependent coefficient of thermal expansion (CTE) of injection molded, short-glass-fiber-reinforced polymers," *Polymer Engineering & Science*, vol. 55, no. 11, pp. 2661–2668, 2015.

[123] S. Nishitsuji, Y. Watanabe, T. Takebe, N. Fujii, M. Okano, and M. Takenaka, "X-ray scattering study on the changes in the morphology of low-modulus polypropylene under cyclic uniaxial elongation," *Polymer Journal*, vol. 52, no. 3, Art. no. 3, 2020.

[124] F. Auriemma, C. De Rosa, R. Di Girolamo, A. Malafronte, M. Scoti, G. R. Mitchell, and S. Esposito, "Deformation of Stereoirregular Isotactic Polypropylene across Length Scales. Influence of Temperature," *Macromolecules*, vol. 50, no. 7, pp. 2856–2870, 2017.

[125] D. Tahara, T. H. Ninh, H. Yamamoto, and K. Tashiro, "Metropolis Monte Carlo Simulation of Two-Dimensional Small-Angle X-ray Scattering Patterns of Oriented Polymer Materials," *Macromolecules*, vol. 53, no. 1, pp. 276–287, 2020.

[126] B. Crist, "Microfibril dimensions from small-angle X-ray scattering," *J Appl Cryst*, vol. 12, no. 1, Art. no. 1, 1979.

[127] H. Jiang and C. Jiang, "Finite deformation constitutive model for macro-yield behavior of amorphous glassy polymers with a molecular entanglement-based internal-state variable," *International Journal of Mechanical Sciences*, vol. 161–162, p. 105064, 2019.

[128] G. Siqueira, D. Kokkinis, R. Libanori, M. K. Hausmann, A. S. Gladman, A. Neels, P. Tingaut, T. Zimmermann, J. A. Lewis, and A. R. Studart, "Cellulose Nanocrystal Inks for 3D Printing of Textured Cellular Architectures," *Advanced Functional Materials*, vol. 27, no. 12, p. 1604619, 2017.

[129] M. R. Mani, A. Gebrekrstos, G. Madras, P. Pötschke, and S. Bose, "PVDF–MWNT interactions control process induced β-lamellar morphology and orientation in the nanocomposites," *Phys. Chem. Chem. Phys.*, vol. 20, no. 38, pp. 24821–24831, 2018.

[130] T. Matsumoto and D. C. Bogue, "Stress birefringence in amorphous polymers under nonisothermal conditions," *Journal of Polymer Science: Polymer Physics Edition*, vol. 15, no. 9, pp. 1663–1674, 1977.

[131] Y. Wang and S.-Q. Wang, "Salient Features in Uniaxial Extension of Polymer Melts and Solutions: Progressive Loss of Entanglements, Yielding, Non-Gaussian Stretching, and Rupture," *Macromolecules*, vol. 44, no. 13, pp. 5427–5435, 2011.

[132] D. T. Turner, "Glass transition elevation by polymer entanglements," *Polymer*, vol. 19, no. 7, pp. 789–796, 1978.

[133] S. Napolitano, E. Glynos, and N. B. Tito, "Glass transition of polymers in bulk, confined geometries, and near interfaces," *Rep. Prog. Phys.*, vol. 80, no. 3, p. 036602, 2017.

[134] W. Yan, I. Richard, G. Kurtuldu, N. D. James, G. Schiavone, J. W. Squair, T. Nguyen-Dang, T. Das Gupta, Y. Qu, J. D. Cao, R. Ignatans, S. P. Lacour, V. Tileli, G. Courtine, J. F. Löffler, and F. Sorin, "Structured nanoscale metallic glass fibres with extreme aspect ratios," *Nature Nanotechnology*, vol. 15, pp. 875–882, 2020.

[135] J. Kim, J. Kim, Y. Shin, and Y. Yoon, "A study on the fabrication of an RTD (resistance temperature detector) by using Pt thin film," *Korean J. Chem. Eng.*, vol. 18, no. 1, pp. 61–66, 2001.

[136] J. Schroers and W. L. Johnson, "Highly processable bulk metallic glass-forming alloys in the Pt–Co–Ni–Cu–P system," *Applied Physics Letters*, vol. 84, no. 18, pp. 3666–3668, 2004.

[137] J. Schroers, "On the formability of bulk metallic glass in its supercooled liquid state," *Acta Materialia*, vol. 56, no. 3, pp. 471–478, 2008.

[138] B. A. Legg, J. Schroers, and R. Busch, "Thermodynamics, kinetics, and crystallization of Pt57.3Cu14.6Ni5.3P22.8 bulk metallic glass," *Acta Materialia*, vol. 55, no. 3, pp. 1109–1116, 2007.

[139] J. Schroers, B. Lohwongwatana, W. L. Johnson, and A. Peker, "Gold based bulk metallic glass," *Appl. Phys. Lett.*, vol. 87, no. 6, p. 061912, 2005.

[140] T. W. Tang, Y. C. Chang, J. C. Huang, Q. Gao, J. S. C. Jang, and C. Y. A. Tsao, "On thermomechanical properties of Au–Ag–Pd–Cu–Si bulk metallic glass," *Materials Chemistry and Physics*, vol. 116, no. 2, pp. 569–572, 2009.

[141] G. Fiore, P. Rizzi, and L. Battezzati, "Phase constitution and glass formation in an Au-based alloy," *Journal of Alloys and Compounds*, vol. 509, pp. S166–S169, 2011.

[142] J. M. Pelletier, S. Cardinal, J. C. Qiao, M. Eisenbart, and U. E. Klotz, "Main and secondary relaxations in an Au-based bulk metallic glass investigated by mechanical spectroscopy," *Journal of Alloys and Compounds*, vol. 684, pp. 530–536, 2016.

[143] Z. Evenson, "On the thermodynamic and kinetic properties of bulk glass forming metallic systems," 2013.

[144] S. Cardinal, J. M. Pelletier, M. Eisenbart, and U. E. Klotz, "Influence of crystallinity on thermo-process ability and mechanical properties in a Au-based bulk metallic glass," *Materials Science and Engineering: A*, vol. 660, pp. 158–165, 2016.

[145] A. Tuniz, K. J. Kaltenecker, B. M. Fischer, M. Walther, S. C. Fleming, A. Argyros, and B. T. Kuhlmey, "Metamaterial fibres for subdiffraction imaging and focusing at terahertz frequencies over optically long distances," *Nature Communications*, vol. 4, no. 1, Art. no. 1, 2013.

[146] Y. Saotome, S. Okaniwa, H. Kimura, and A. Inoue, "Superplastic Nanoforging of Pt-Based Metallic Glass with Dies of Zr-BMG and Glassy Carbon Fabricated by Focused Ion Beam," *Materials Science Forum*, 2007.

[147] J. P. Chu, H. Wijaya, C. W. Wu, T. R. Tsai, C. S. Wei, T. G. Nieh, and J. Wadsworth, "Nanoimprint of gratings on a bulk metallic glass," *Appl. Phys. Lett.*, vol. 90, no. 3, p. 034101, 2007.

[148] A. Tuniz, R. Lwin, A. Argyros, S. C. Fleming, E. M. Pogson, E. Constable, R. A. Lewis, and B. T. Kuhlmey, "Stacked-and-drawn metamaterials with magnetic resonances in the terahertz range," *Opt. Express, OE*, vol. 19, no. 17, pp. 16480–16490, 2011.

[149] G. Kumar and J. Schroers, "Write and erase mechanisms for bulk metallic glass," *Appl. Phys. Lett.*, vol. 92, no. 3, p. 031901, 2008.

[150] S. Park, Y. Guo, X. Jia, H. K. Choe, B. Grena, J. Kang, J. Park, C. Lu, A. Canales, R. Chen, Y. S. Yim, G. B. Choi, Y. Fink, and P. Anikeeva, "One-step optogenetics with multifunctional flexible polymer fibers," *Nature Neuroscience*, vol. 20, no. 4, Art. no. 4, 2017.

[151] F. Qin, G. T. Bae, Z. Dan, H. Lee, and N. J. Kim, "Corrosion behavior of the Mg65CU25Gd10 bulk amorphous alloys," *Materials Science and Engineering: A*, vol. 449–451, pp. 636–639, 2007.

[152] A. Kawashima, K. Ohmura, Y. Yokoyama, and A. Inoue, "The corrosion behaviour of Zr-based bulk metallic glasses in 0.5M NaCl solution," *Corrosion Science*, vol. 53, no. 9, pp. 2778–2784, 2011.

[153] H. Kou, Y. Li, T. Zhang, J. Li, and J. Li, "Electrochemical corrosion properties of Zr- and Ti-based bulk metallic glasses," *Transactions of Nonferrous Metals Society of China*, vol. 21, no. 3, pp. 552–557, 2011.

[154] M. Carmo, R. C. Sekol, S. Ding, G. Kumar, J. Schroers, and A. D. Taylor, "Bulk Metallic Glass Nanowire Architecture for Electrochemical Applications," *ACS Nano*, vol. 5, no. 4, pp. 2979–2983, 2011.

[155] R. C. Sekol, G. Kumar, M. Carmo, F. Gittleson, N. Hardesty-Dyck, S. Mukherjee, J. Schroers, and A. D. Taylor, "Bulk Metallic Glass Micro Fuel Cell," *Small*, vol. 9, no. 12, pp. 2081–2085, 2013.

[156] G. Doubek, R. C. Sekol, J. Li, W.-H. Ryu, F. S. Gittleson, S. Nejati, E. Moy, C. Reid, M. Carmo, M. Linardi, P. Bordeenithikasem, E. Kinser, Y. Liu, X. Tong, C. O. Osuji, J. Schroers, S. Mukherjee, and A. D. Taylor, "Guided Evolution of Bulk Metallic Glass Nanostructures: A Platform for Designing 3D Electrocatalytic Surfaces," *Advanced Materials*, vol. 28, no. 10, pp. 1940–1949, 2016.

[157] J. Schroers, G. Kumar, T. M. Hodges, S. Chan, and T. R. Kyriakides, "Bulk metallic glasses for biomedical applications," *JOM*, vol. 61, no. 9, pp. 21–29, 2009.

[158] Y. Guo, S. Jiang, B. J. B. Grena, I. F. Kimbrough, E. G. Thompson, Y. Fink, H. Sontheimer, T. Yoshinobu, and X. Jia, "Polymer Composite with Carbon Nanofibers Aligned during Thermal Drawing as a Microelectrode for Chronic Neural Interfaces," *ACS Nano*, vol. 11, no. 7, pp. 6574–6585, 2017.

[159] S. F. Cogan, "Neural Stimulation and Recording Electrodes," *Annual Review of Biomedical Engineering*, vol. 10, no. 1, pp. 275–309, 2008.

[160] R. Green, H. Toor, C. Dodds, and N. Lovell, "Variation in Performance of Platinum Electrodes with Size and Surface Roughness," *Sensors and Materials*, vol. 24, pp. 165–180, 2012.

[161] C. Lu, U. P. Froriep, R. A. Koppes, A. Canales, V. Caggiano, J. Selvidge, E. Bizzi, and P. Anikeeva, "Polymer Fiber Probes Enable Optical Control of Spinal Cord and Muscle Function In Vivo," *Advanced Functional Materials*, vol. 24, no. 42, pp. 6594–6600, 2014.

[162] Y. Lu, T. Li, X. Zhao, M. Li, Y. Cao, H. Yang, and Y. Y. Duan, "Electrodeposited polypyrrole/carbon nanotubes composite films electrodes for neural interfaces," *Biomaterials*, vol. 31, no. 19, pp. 5169–5181, 2010.

[163] F. Vitale, S. R. Summerson, B. Aazhang, C. Kemere, and M. Pasquali, "Neural Stimulation and Recording with Bidirectional, Soft Carbon Nanotube Fiber Microelectrodes," *ACS Nano*, vol. 9, no. 4, pp. 4465–4474, 2015.

[164] M. J. I. A. Leccardi, P. Vagni, and D. Ghezzi, "Multilayer 3D electrodes for neural implants," *J. Neural Eng.*, vol. 16, no. 2, p. 026013, 2019.

[165] X. Beebe and T. L. Rose, "Charge injection limits of activated iridium oxide electrodes with 0.2 ms pulses in bicarbonate buffered saline (neurological stimulation application)," *IEEE Transactions on Biomedical Engineering*, vol. 35, no. 6, pp. 494–495, 1988.

[166] N. Aliakbarinodehi, F. Stradolini, S. A. Nakhjavani, I. Tzouvadaki, I. Taurino, G. De Micheli, and S. Carrara, "Performance of Carbon Nano-Scale Allotropes in Detecting Midazolam and Paracetamol in Undiluted Human Serum," *IEEE Sensors Journal*, vol. 18, no. 12, pp. 5073–5081, 2018.

[167] A. Wong, A. M. Santos, and O. Fatibello-Filho, "Simultaneous determination of paracetamol and levofloxacin using a glassy carbon electrode modified with carbon black, silver nanoparticles and PEDOT:PSS film," *Sensors and Actuators B: Chemical*, vol. 255, pp. 2264–2273, 2018.

[168] J. Smajdor, R. Piech, M. Ławrywianiec, and B. Paczosa-Bator, "Glassy carbon electrode modified with carbon black for sensitive estradiol determination by means of voltammetry and flow injection analysis with amperometric detection," *Analytical Biochemistry*, vol. 544, pp. 7–12, 2018.

[169] F. C. Vicentini, P. A. Raymundo-Pereira, B. C. Janegitz, S. A. S. Machado, and O. Fatibello-Filho, "Nanostructured carbon black for simultaneous sensing in biological fluids," *Sensors and Actuators B: Chemical*, vol. 227, pp. 610–618, 2016.

[170] X. Zhang, Y. Peng, J. Bai, B. Ning, S. Sun, X. Hong, Y. Liu, Y. Liu, and Z. Gao, "A novel electrochemical sensor based on electropolymerized molecularly imprinted polymer and gold nanomaterials amplification for estradiol detection," *Sensors and Actuators B: Chemical*, vol. 200, pp. 69–75, 2014.

[171] S. Cinti, F. Arduini, M. Carbone, L. Sansone, I. Cacciotti, D. Moscone, and G. Palleschi, "Screen-Printed Electrodes Modified with Carbon Nanomaterials: A Comparison among Carbon Black, Carbon Nanotubes and Graphene," *Electroanalysis*, vol. 27, no. 9, pp. 2230–2238, 2015.

[172] J.-L. Chang and J.-M. Zen, "Fabrication of disposable ultramicroelectrodes: Characterization and applications," *Electrochemistry Communications*, vol. 8, no. 4, pp. 571–576, 2006.

[173] T.-H. Yang, C.-Y. Liao, J.-L. Chang, C.-H. Lien, and J.-M. Zen, "A Simple Electrochemical Approach Based on Inexpensive Wall-Jet Screen-Printed Ring Disk Electrode to Evaluate Oxygen Reduction Catalysts," *Electroanalysis*, vol. 21, no. 21, pp. 2390–2394, 2009.

[174] C.-Y. Liao, C.-C. Chang, C. Ay, and J.-M. Zen, "Flow Injection Analysis of Chloramphenicol by Using a Disposable Wall-Jet Ring Disk Carbon Electrode," *Electroanalysis*, vol. 19, no. 1, pp. 65–70, 2007.

[175] V. Katseli, A. Economou, and C. Kokkinos, "A novel all-3D-printed cell-on-a-chip device as a useful electroanalytical tool: Application to the simultaneous voltammetric determination of caffeine and paracetamol," *Talanta*, vol. 208, p. 120388, 2020.

[176] E. M. Richter, D. P. Rocha, R. M. Cardoso, E. M. Keefe, C. W. Foster, R. A. A. Munoz, and C. E. Banks, "Complete Additively Manufactured (3D-Printed) Electrochemical Sensing Platform," *Anal. Chem.*, vol. 91, no. 20, pp. 12844–12851, 2019.

[177]   M. P. Browne, F. Novotný, Z. Sofer, and M. Pumera, "3D Printed Graphene Electrodes' Electrochemical Activation," *ACS Appl. Mater. Interfaces*, vol. 10, no. 46, pp. 40294–40301, 2018.

[178]   M. T. Olaleye and B. T. J. Rocha, "Acetaminophen-induced liver damage in mice: Effects of some medicinal plants on the oxidative defense system," *Experimental and Toxicologic Pathology*, vol. 59, no. 5, pp. 319–327, 2008.

[179]   A. M. Larson, J. Polson, R. J. Fontana, T. J. Davern, E. Lalani, L. S. Hynan, J. S. Reisch, F. V. Schiødt, G. Ostapowicz, A. O. Shakil, and W. M. Lee, "Acetaminophen-induced acute liver failure: Results of a United States multicenter, prospective study," *Hepatology*, vol. 42, no. 6, pp. 1364–1372, 2005.

[180]   S. Aiassa, F. Stradolini, A. Tuoheti, S. Carrara, and D. Demarchi, "Quasi-Digital Biosensor-Interface for a Portable Pen to Monitor Anaesthetics Delivery," *2019 15th Conference on Ph.D Research in Microelectronics and Electronics (PRIME)*, 2019.

[181]   J. Wang, B. Yang, F. Gao, P. Song, L. Li, Y. Zhang, C. Lu, M. C. Goh, and Y. Du, "Ultra-stable Electrochemical Sensor for Detection of Caffeic Acid Based on Platinum and Nickel Jagged-Like Nanowires," *Nanoscale Research Letters*, vol. 14, no. 1, p. 11, 2019.

[182]   C. Xie, J. Liu, T.-M. Fu, X. Dai, W. Zhou, and C. M. Lieber, "Three-dimensional macroporous nanoelectronic networks as minimally invasive brain probes," *Nature Materials*, vol. 14, no. 12, Art. no. 12, 2015.

[183]   G. Hong and C. M. Lieber, "Novel electrode technologies for neural recordings," *Nature Reviews Neuroscience*, vol. 20, no. 6, Art. no. 6, 2019.

[184]   J. Phair, J. Benson, C. McCormac, J. Cundell, S. Gracheva, D. Wilkinson, S. Forsythe, and J. Davis, "Butyl grafted polyethylene films doped with carbon black: A foundation for the development of smart bandages," *Sensors and Actuators B: Chemical*, vol. 193, pp. 764–769, 2014.

[185]   T. Iwama, K. Y. Inoue, H. Abe, and T. Matsue, "Chemical Imaging Using a Closed Bipolar Electrode Array," *Chemistry Letters*, vol. 47, no. 7, pp. 843–845, 2018.

Curriculum Vitae

Rue de la gare 15B
1110 Morges

+41 79 393 47 53
ines.richard26@gmail.com

Swiss
Single, 28 years old

Inès Richard

Engineer in Materials Science EPF

Education

2016-Present   **PhD studies in Materials Science and Engineering**, *Ecole Polytechnique Fédérale de Lausanne (EPFL)*, Laboratory of Photonic Materials and Fibre Devices.
- Thesis title: *Ultimate feature sizes in thermally drawn fibers: from fundamental analysis to novel functional fibers*, Supervision: Prof. F. Sorin

2013-2015   **Master studies in Materials Science and Engineering**, *Ecole Polytechnique Fédérale de Lausanne (EPFL)*, Three-month research at The University of Tokyo, Japan, as part of a collaborative master project.
- Master thesis title: *Tensile cyclic deformation and low cycle fatigue behaviour of laminated steel composites*, Supervision: Prof. A. Mortensen and Prof. S. Nambu
- Semester project 2: *Thermal drawing of electrically conductive polymer composites*, Supervision: Prof. F. Sorin
- Semester project 1: *New mechanical testing for self-healing fibre-reinforced polymer*, Supervision: Prof. V. Michaud

2010-2013   **Bachelor studies in Materials Science and Engineering**, *Ecole Polytechnique Fédérale de Lausanne (EPFL)*, Third year as an exchange student at The University of Manchester, United Kingdom.
- Bachelor thesis: *Overload effects on fatigue crack-tip fields under plane stress & plane strain*, Supervision: Prof. P. Withers

Awards

Excellence fellowship for the master studies obtained from EPFL
Award for the best academic diploma project of the IMX faculty

Experience

2016-Present   **Doctoral assistant**, *Laboratoy of Photonic Materials and Fibre Devices, EPFL*.
- Exercise Assistant in the course "Materials: From chemistry to properties"
- Student supervision during semester projects
- Person in charge of the lab visits

2014 (6 months)	**Internship on electrically nonlinear ceramic resistors**, *ABB Corporate Research Center, BadenDättwil, AG*.

- Manufacturing of ceramic resistors
- Optimization of manufacturing parameters
- Characterization of the electrical properties and microstructure

Skills

Computer knowledge

Programming	Basic skills in C programming, Mathematica, MATLAB, html, python
Data/image processing	Origin, Illustrator, Inventor
Editing	Use of L^AT_EX and Microsoft Office

Technical Competences

Characterization techniques	Optical microscopy, scanning electron microscopy (SEM, EBSD, EDS), transmission electron microscopy (TEM, STEM), X-ray crystallography (XRD), laser topography, electrical conductivity measurements, hardness testing, mechanical testing (traction, compression, toughness, fatigue), Thermo-mechanical testing (DSC, DMA, TMA)
Processing	Resin infusion moulding, fiber drawing, manufacturing of ceramics (spray drying, compaction, sintering)

Languages

French	Mother tongue
English	Fluent
German	Upper intermediate

Publication and conferences

2020 I. Richard, W. Yan and F. Sorin, "Thermal Drawing of Structured Nanoscale Metallic Glass Fibers", MRS Fall meeting

2019 I. Richard, W. Yan, T. Dang Nguyen, T. Das Gupta, Y. Qu and F. Sorin, "Thermal drawing of bulk metallic glasses: fundamentals and applications", 25th International Congress on Glass ICG, Boston, USA

W. Yan, I. Richard, G. Kurtuldu, ... , and F. Sorin, "Structured nanoscale metallic glass fibres with extreme aspect ratios", *Nature Nanotechnology* **15**, 875-882 (2020)

S. Shadman, T. Nguyen-Dang, T. Das Gupta, A. G. Page, I. Richard, A. Leber, J. Ruza, G. Krishnamani, and F. Sorin, "Microstructured Biodegradable Fibers for Advanced Control Delivery", *Advanced Functional Materials* **30**, 1910283 (2020)

I. Richard*, T. Nguyen Dang*, E. Goy, F. Sordo and F. Sorin, "Insights into the fabrication of sub-100 nm textured thermally drawn fibers", *Journal of Applied Physics* **125**, 175301 (2019)

E. Manfredi, A. Cohades, I. Richard and V. Michaud, "Assessment of solvent capsule-based healing for woven E-glass fibre-reinforced polymers", *Smart Materials and Structures* **24**, 015019 (2014)

Patent

"Ultralong, complexly structured micro- and nanoscale metallic glasses and fibers", F. Sorin, I. Richard, W. Yan, J. Loeffler, G. Courtine